TECHNISCHE UNIVERSITÄT MÜNCHEN

Institut für Photogrammetrie und Kartographie

Fachgebiet Photogrammetrie und Fernerkundung

Glacier Monitoring using Spaceborne SAR Intensity Images

Li Fang

Dissertation

2017

TECHNISCHE UNIVERSITÄT MÜNCHEN
Institut für Photogrammetrie und Kartographie
Fachgebiet Photogrammetrie und Fernerkundung

Glacier Monitoring using Spaceborne SAR Intensity Images

Li Fang

Abstract

In last decade, Synthetic Aperture Radar (SAR) is becoming a popular technology for the monitoring of glaciers in polar region and alpine areas, accounting for its specific advantages of being independent from weather and sunlight conditions. In particular, in the field of glaciology, the spaceborne SAR has been widely applied to measure the velocity of glacier surface movement helping the understanding of glacier dynamics, and detect the glacier facies for analysing the mass balance of glacier. However, for the conventional method of glacier surface motion estimation that based on patch-based correlation techniques, there is always a trade-off between the size of matching template and the preservation of local details occurs. Moreover, the traditional methods for glacier facies detection using single polarimetric SAR data are pixel-based ones depending highly on various SAR backscatter coefficients, which are limited by the insufficient information existing in a resolution cell and have the less consideration on spatial distribution of different land covers. Both these factors mentioned have restrained the performance of glacier monitoring.

In this thesis, methods and strategies for the glacier monitoring task, involving the quantitative estimation of glacier surface motion and the multi-objects classification on and around the glacier surface areas, have been developed and evaluated with different research areas and datasets, separately, with spaceborne SAR intensity images used.

The estimation of glacier surface motion is conducted via the extraction of point like features from the intensity image pair and the robust phase correlation algorithm. Additionally, to increase the robustness, an adaptive refined Lee filter is developed for despeckling SAR images, aiming to achieve a trade-off between the suppression of noise and the preservation of local image textures. On the other hand, a supervised classification method of the glacier surface areas is conducted in order to detect the glacier facies. This method takes advantages of the discrimination ability of sparse representations, based on which a feature extraction technique called supervised neighbourhood embedding is constructed. Alternatively, a gradient method is also developed to update the dictionary and the projection matrix.

The test area including six TerraSAR-X images covered two different glaciers, namely the Taku glacier and Baltoro glacier, representing discriminative glacier characteristics in light of dimensions, surface features, topography etc. are used for assessing the performances of methodologies. In addition, simulated SAR dataset are adopted to evaluate the performance of robust phase correlation algorithm and the proposed adaptive refined Lee filter, in the context of SAR intensity images contaminated by noise.

The analysis and discussion about results of glacier movement and classification, under a variety of tests using both the simulated and real SAR datasets, have confirmed the superiority and feasibility of the proposed methods compared to the existing classical methods and algorithms.

Kurzfassung

Zum Zwecke eines besseren Verständnisses der Gletscherdynamik und Massenbilanz wurde Synthetic Aperture Radar (SAR) in großem Umfang angewendet, um die Bewegungsgeschwindigkeit und Flächen von Gletscheroberflächen zu vermessen. Jedoch tritt bei herkömmlichen verwendeten Methoden für die Schätzung von Gletscheroberflächenbewegungen, vor allem auf Basis von Patch-Korrelationstechniken, immer ein Kompromiss zwischen der Größe der passenden Fenster und die Erhaltung der lokalen Details auf. Darüber hinaus sind die traditionellen Methoden zur Gletschererkennung mit einfach-polarimetrischen SAR-Daten pixel-basiert und hängen in hohem Maße von verschiedenen SAR-Rückstreu-Koeffizienten ab, die durch ungenügende Informationen in einer Auflösungszelle begrenzt sind und weniger Rücksicht auf die räumliche Verteilung der verschiedenen Landabdeckungen nehmen.

In dieser Arbeit wird die Bewegungsschätzung der Gletscheroberfläche über die Extraktion von punktförmigen Merkmalen aus einem SAR-Intensitäts Bildpaar und die Verwendung eines robusten Phasenkorrelations-Algorithmus durchgeführt. Darüber hinaus, um die Robustheit zu erhöhen, wird ein neuartiger adaptiver und verfeinerter Lee-Filter für die Entfernung von Fleckenrauschen entwickelt, die nach Erreichung eine gute Balance zwischen der Unterdrückung von Rauschen und die Erhaltung der lokalen Bildtexturen anstrebt. Auf der anderen Seite wird ein überwachtes Klassifikationsverfahren vorgeschlagen um die Detektion von Gletscherregionen abzuschätzen. Das vorgeschlagene Klassifikationsverfahren nutzt die Vorteile der Unterscheidungsfähigkeit von spärlichen Darstellungen aus, und ist auf Grundlage einer Technik zur Merkmalsextraktion mit Einbettung von Nachbarschaften aufgebaut. Außerdem wird ein Gradientenverfahren entwickelt, um das Wörterbuch und die Projektionsmatrix zu aktualisieren.

Die Analyse und Diskussion über die Ergebnisse der Gletscherbewegung und Klassifikation, unter einer Vielzahl von Tests unter Verwendung von sowohl simulierten als auch realen SAR Datensätzen, haben die Überlegenheit und die Durchführbarkeit der vorgeschlagenen Methoden bestätigt, wenn sie mit den bestehenden klassischen Methoden und Algorithmen verglichen werden.

Contents

List of Abbreviations

Abbreviation	Description	Page
ARLee	adaptive refined Lee	31
BC	backscatter coefficients	26
CoV	coefficient of variation	32
DEM	digital elevation model	21
DFT	discrete fourier transform	38
D-InSAR	differential interferometry SAR	21
DPLC	learning dictionary and projection matrix for linear classification	41
EEC	enhanced ellipsoid corrected	49
ENL	equivalent number of looks	32
EPI	edge preservation index	52
FT	Fourier transform	36
GED	generalized eigenvalue decomposition	45
IFT	inverse fourier transform	24
InSAR	interferometric SAR	20
LDA	Linear Discriminant Analysis	72
LMMSE	linear minimum mean square error	33
LOS	line of sight	31
LSM	Least square matching	24
MAI	multi-aperture InSAR	21
ML	maximum likelihood	20
NCC	normalized cross correlation	20
NCR	natural corner reflector	69
NN	Nearest neighbors	43
PC	phase correlation	16
PEF	peak evaluation formula	25
PLF	point like feature	16
RANSAC	random sample consensus	25
RMSE	root mean square error	52
SAR	Synthetic aperture radar	15
SIFT	scale-invariant feature transform	29
SLC	Single- Look Complex	21
SM	stripmap mode	35
SMPI	suppression and mean preservation index	52
SNE	Supervised Neighborhood Embedding	43
SNR	signal to noise ratio	59
SR	sparse representation	16
SSC	single look slant range complex	49
SVD	singular value decomposition	25
SVM	support vector machines	27
SWIR	shortwave infrared	26
TSX	TerraSAR-X	22
VIS	visible spectrum	26
ZNCC	zero mean normalized cross correlation	23

List of Figures

List of Tables

1 Introduction

1.1 Motivation and Objective of the Thesis

Glaciers act as important components in albedo feedback mechanisms of the local and global climate system [Rees, 2006]. Glaciers also play vital roles as crucial reservoirs of global fresh water. For instance, some regions (e.g. Central Asia) characterized by water stress and densely population are reliant at a large extent on the melt water of alpine glaciers [Pellikka & Rees, 2010].

Moreover, in the context of global warming, the melting glaciers are expected to make increasing contributes to global sea level rise [Gardner et al., 2013]. It is estimated that melting glaciers accounts for approximately 29% of the observed sea level rise [Schubert et al., 2013]. Therefore, researches on the behaviors of glacier and the glacier mass balance with geometry changes have drawn growing attentions in the past decades.

The earliest monitoring and studies of glaciers depended mainly upon the repeated field-survey by glaciologists. The researchers had to travel to far-flung glaciers, normally located in high-altitude mountainous areas characterized by hazardous environment, in order to collect field measuring data only in few dozen points accompanying with time-consuming and expensive field surveys. Accordingly, due to the inaccessibility of many glaciers and the environmental hazards, the acquisition of reliable measuring data in large scale was always a challenging task [Schubert et al., 2013]. To that end, remotely sensed data, especially the spaceborne imagery, providing high resolution, trustworthy, large scale, and time-sequential measurements in a cost-effective manner, are expected to be capable for the glacier monitoring task.

With respect to the remote sensing sensors, optical and infrared sensors have been extensively applied on glacier monitoring tasks. However, the frequently happened cloud-coverage in polar and alpine regions inevitably makes the abidingly acquisition of optical data impossible, thus leading to insufficient datasets. Within opposite to that, in the last decade, remote sensed Synthetic aperture radar (SAR) images are more and more popular to be applied on measuring glaciers. This is due to that the SAR sensor emit its special electromagnetic energy, allowing to obtain images with no limitations in terms of weather phenomena and illumination. It can collect data reliably with a pre-defined temporal interval over long periods of time, with a spatial resolution compatible with the task of glacier monitoring.

As for glaciology, the spaceborne SAR has as many applications as other imaging techniques. SAR can be used to measure glacier velocity helping the understanding of glacier dynamics, and detecting glacial facies for the analysis of glacier mass balance, on the basis of its ability to penetrate down below the glacier surface and the SAR backscattering contributions affected by the dielectric and geometric properties (surface roughness, morphology, shape and grain size) of glacier facies. Nevertheless, the applications of SAR images for glacier monitoring still have some critical challenges. On one hand, the spaceborne SAR image is normally hampered by the trade-off between the suppression of noise and the preservation of image details. For example, the

conflict between matching template size and preservation of local details occurs in all normally used 'correlation like' methods, although larger template size normally accepted because of the entity unique but it increases the computation time exponentially, error in displacement estimation due to more geometric distortion and the sparsity of estimation results. On the other hand, the traditional glacier facies detection methods using SAR data are pixel-based ones depending on various SAR backscatter characteristics of resolution cells from different classes which are limited by the information existing in one resolution cell and the less consideration on spatial distribution of different land covers.

Facing these drawbacks in glacier monitoring using spaceborne SAR images, this thesis is trying to provide a processing chain for the glaciers monitoring task involving two aspects, namely the quantitive estimation of glacier surface motion and the multi-classes classification of the glacier.

The estimation of glacier surface motion is conducted via proposed point like feature (PLF) and the robust phase correlation (PC) algorithm, and also an adaptive refined version of Lee filter is developed for the despeckling of SAR images aiming to find a appropriate balance between noise suppression and image details preservation. Whereas, the multi-classes classification on and around the glacier is carried out by taking advantage of the structure in sparse domain. Discriminative features are directly learned on sparse representation (SR). The dictionary and the linear projection for data representation and task of classification are alternatively learned, respectively. This method is proposed on the basis of the relationships between target pixel and its neighboring pixels, which focuses on the local geometry of image patches, but not the purely value of pixels.

1.2   Structure of the Thesis

This thesis is structured in 8 chapters as follows:

The Chapter 2 introduces current works in the field of glacier velocity and glacial facies detection using spaceborne SAR images as well as the state of art of the related topics on despeckling and denoising of SAR image, phase correlation algorithms, and sparse representation. According to the discussion on strength and weakness of the existing approaches, the motivation and objectives of this thesis are raised.

In Chapter 3, the proposed processing chain for the estimation of glacier surface motion via point like feature and the robust phase correlation algorithm is explained in detail. First, an adaptive refined version of Lee filter is developed for the despeckling of SAR images. Then, the methods for elimination of SAR topographic information and co-registration are presented. Afterwards, the selection of point like feature and robust phase correlation algorithm is given.

In Chapter 4, the methodology about multi-classes classification of glacier in terms of discriminative features learned from sparse representation is given. First, the basic principles about the data-driven dictionary learning are illustrated. Afterwards, we learn low-dimensional discriminative features from sparse coefficients and then classify such extracted features using a linear classifier (e.g., SVM). We shortly refer the entire learning framework as jointly learning dictionary and projection matrix for linear classification.

Chapter 5 firstly introduces the data sets used in experiments as well as the study areas. Then, the design of the experiment framework is depicted.

Chapter 6 presents the experimental results for the data sets described in Chapter 5 achieved by applying the methodologies proposed in Chapter 3 (i.e., glacier surface motion estimation) and 4 (i.e., glacier facies detection), separately.

In Chapter 7, critical discussions related to the experimental results displayed in Chapter 6 are presented.

Chapter 8 finally concludes the thesis according to the findings above and gives some perspectives for future research directions.

2 State of the Art in Glacier Monitoring using SAR images

Solutions for the glacier monitoring tasks in this thesis is given via analyzing two important features which are most indeed to be obtained using spaceborne SAR intensity images and outlined in Section 1.1, namely the glacier surface velocity, and the glacier facies. Thus, in the following sections, the state-of-the-art in these areas related to this thesis will be presented. Current researches dealing with glacier surface motion estimation will be overviewed in Section 2.1. Then, the reviews on despeckling and denoising of SAR images, and image matching methods in light of dense matching are illustrated in Section 2.2 and 2.3 served as sub-subjects of glacier motion estimation, separately. Consequently, recent research work and methods applied on glacier areas classification will be presented in Section 2.4. Afterwards, in Section 2.5, the sub-subject of glacier areas classification, namely sparse representation, is described. Finally, the contributions of this thesis based on the literature review and identified gaps in the state-of-the-art are listed in Section 2.6.

2.1 Glacier Surface Motion Monitoring

The behavior of the glacier flow acts always like a river, which has higher velocity rate in the parts closer to the surface and center of riverbed than those in the bottom and sides. The monitoring of glacier surface motion as well as its velocity is an essential method to obtain the quantitative changes of glacier providing numerical clues to deducing past glacier changes and predicting future developments [Schubert et al., 2013].

The traditional optical imagery acquired by earth observation satellites are the most commonly used data for glacier monitoring, featured for its high resolution, wide coverage, lower cost and shorter revisiting period. Many researchers have already used optical imagery for measuring glacier topography [Fallourd et al., 2011], surface displacements [Schubert et al., 2013] and velocity [Berthier et al., 2005]. However, the frequently happened cloud-coverage in polar and alpine regions inevitably makes the abidingly acquisition of optical data impossible, thus leading to insufficient dataset. Moreover, snowfalls in winter time and lack of ground texture in the ice field will largely increase the difficulties of finding corresponding points or features from images.

Opposite to optical observation system, the spaceborne SAR imaging system is a complementary information source which has the advantage of providing images all year round, with no limitations in terms of weather condition and imaging time, as the SAR sensors emit and receive its own electromagnetic radiation. It can reliably collect data with a pre-defined temporal interval over long periods of time with a spatial resolution compatible with the application of glacier monitoring. Additionally, active SAR sensors observe both the amplitude and phase information of the backscattering signal from the ground target [Baghdadi et al., 1997; Fahnestock et al., 1993]. To be specific, the magnitude information of SAR data reports spatial features and textures of the

imaging area and backscattering coefficients of the ground, while the phase information reveals the phase difference of the radar signal. With regard to the ground resolution, spaceborne SAR data (e.g. TSX spotlight mode) can reach as high as 1m resolution, with fully polarimetric data, which will be helpful to extract different features and backscattering characteristics [Goldstein et al., 1993; Fahnestock et al., 1993; Kumara et al., 2011; Vasile et al., 2006] .

Generally speaking, the popular used approaches for glacier dynamics monitoring using SAR images data can be summarized into two main categories. The first category is named as off-set tracking based approaches, while the second category is in relation to interferometric SAR technique which utilizes the phase difference and interferometric principle.

2.1.1   Offset Tracking Method

In the first category, the amplitude information of SAR data, usually in the form of intensity image, is utilized. The offset tracking is mainly conducted through the 'correlation like' methods, so that the offsets of point or feature on glacier surface can be measured. Among all the methods, intensity tracking, feature tracking and speckle tracking are the commonly used approaches.

- **Intensity tracking,** also known as cross-correlation optimization procedure, which is normally based on pixel-to-pixel image correlation algorithm, correlates small image patches so as to derive the relative displacements between image pairs in the range and azimuth directions, respectively. This technique was first introduced in optical data based domain [Scambos et al., 1992], and later applied for SAR images based application extensively [Strozzi et al., 2002]. Among all the correlation algorithms, normalized cross correlation (NCC) [Lewis, 1995], maximum likelihood (ML) [Erten et al., 2009], multi-resolution wavelet decomposition [Schubert et al., 2013] and their variants are most commonly used for finding corresponding parches. However, the successful intensity tracking always relies on the glacier surface texture which facilitates the matching accuracy and robustness. If the glacier surfaces have no distinctive patterns or textures, the matching result will be significantly influenced.

- **Feature tracking** counts on the detection of movement of identifiable objects (e.g. crevasses, moraines) or feature points on the glacier surface in sequential, co-registered image pairs, making it possible to derive a 2-D velocity field. The feature tracking approaches can be divided into two groups: manually selection and automated tracking. In the early ages, feature tracking was mainly conducted in manual ways [Lucchitta & Ferguson, 1986; Lucchitta et al., 1993], whereas currently the features are selected and tracked automatically relying on cross-correlating algorithm (e.g. NCC) [Fallourd et al., 2011; Nagler et al., 2012] or characteristic operator (e.g. SIFT) [Liu & Yamazaki, 2013]. The mandatory for these approaches is that the features remain relatively undisturbed on the glacier over the period of observation. Then, the relative shifts measured between the conjugate features in matching and reference images can provide estimation of motion within the observation time [Schubert et al., 2013].

- Similarly, **speckle tracking** can be regarded as a modification of SAR feature tracking. Different from typical SAR feature tracking, this kind of methods requires no recognizable objects or distinctive feature points on the glacier, using speckle pattern of SAR image instead, which is a high-frequency noise-like phenomenon present in all coherent measurement systems, can be correlated between SAR image pairs under certain conditions. Normally, the tracking of speckle patterns is mainly achieved via correlation based matching algorithm [Gray et al., 2001; Joughin et al., 2010; Michel & Rignot, 1999], but in some cases, speckle

tracking can also utilize both the amplitude and phase information of the SAR data [Schubert et al., 2013], for the sake of robustness. In [Bamler & Eineder, 2005], the pros and cons of using native-complex information of SAR data are discussed as well. In addition, in more common applications, the advantages of tracking both conventional features and speckle patterns are combined into one single method [de Lange et al., 2007; Floricioiu et al., 2008; Luckmann et al., 2004; Pritchard et al., 2005; Strozzi et al., 2002], so as to achieve a best result of monitoring.

2.1.2 InSAR Based Method

Complementary to the offset tracking approach, the InSAR based method can be called as most accurate technique using SAR data for glacier surface monitoring, with the highest known sensitivity and accuracy to surface motion. With the help of following phase changes or the order of the transmitted wavelength, the motion of surface feature patterns can be precisely measured [Rosen et al., 2000; Bamler & Hartl, 1998]. The frequently used approaches include differential interferometry SAR (D-InSAR) , multi-aperture InSAR (MAI) and coherence tracking.

- **D-InSAR** techniques aim to detect ground deformations from the differential results of two or more repeated InSAR image pairs by comparing the InSAR result [Schubert et al., 2013]. D-InSAR techniques has greatly contributed to glaciology by offering the ability of mapping ice flows over almost globally located glaciers and ice sheets with the most accurate precision [Joughin et al., 1998; Luckman et al., 2007; Trouve et al., 2007; Li et al., 2008; Kumara et al., 2011]. For example, the interferometric velocity measurements of the Arctic and Antarctic ice sheets and streams [Kwok & Fahnestock, 1996; Rignot & Jacobs, 2002], alpine glaciers [Mattar et al., 1998; Cumming & Zhang, 1999; Li et al., 2008] and the Aletsch glacier [Prats et al., 2009]. However, it is noteworthy that the topographic information should be removed from the SAR data by external digital elevation model (DEM) or multiple SAR pair [Schubert et al., 2013].

- With regard to **MAI,** it is an alternative approach overcoming the one direction limitation of conventional InSAR technique and inferring azimuth displacement from an interferometric pair [Bechor & Zebker, 2006]. In [Gourmelen et al., 2011; Zhou et al., 2014], comparisons between traditional InSAR and MAI for ice velocity and the glacier thickness are conducted and discussed, respectively. Moreover, the 3D motions of Dongkemadi glacier are estimated in [Hu et al., 2014a].

- **Coherence tracking,** or coherence optimization is a technique related to SAR interferometry. The interferometric coherence represents the degree of phase correlation between a pair of Single- Look Complex (SLC) products. The basic assumption underlying this method is that a loss of coherence for acquisitions over a moving glacier will to a large extent be the result of local co-registration errors. By adjusting the relative offsets of such low-coherence regions until the local coherence is maximized, it is presumed that the relative surface motion will also have been more accurately captured [Derauw, 1999]. To accomplish this, a number of image sub-windows distributed over the SLC scenes are used to create a series of interferograms for which the coherence is estimated. Generally, coherence tracking is utilized in combination with other methods such as D-InSAR and feature tracking [Strozzi et al., 2002; Derauw, 1999].

2.1.3   Conclusion from the Literature Review

However, all the aforementioned two categories (section 2.1.1 and 2.1.2) of approaches still have some disadvantages. For the InSAR based method, although this kind of method can provide the highest accuracy when measuring the glacier, it is often limited by phase noise characterized by the coherence of glacier surface [Strozzi et al., 2002], which is affected by meteorological and flow characteristics (i.e., ice and snow surface melt, snow and rain fall, wind-provoked snow drift, fast flow rate). And also, the D-InSAR based methods can only measure the glacier motions in slant range direction hampering the generation of the full three-component velocity vectors [Trouve et al., 2007]. In addition, if the moving of glacier is too fast or the time interval of reacquisition is too large resulting in a lager deformation of glacier surface, it is also counterproductive to the utility of D-InSAR technique, which is the case for many SAR satellites [Trouve et al., 2007]. Especially, for TerraSAR-X (TSX) data in X-band, it is more sensitive to the ground surface roughness and changes increasing the difficulties of using D-InSAR for glacier motion estimation within 11 days interval [Fallourd et al., 2011].

As for the offset-tracking based approach, its accuracy of pixel-offset measurements depends on the quality of cross-correlation algorithm or feature operator, and is limited by the texture, features as well as the resolution of SAR intensity images [Fallourd et al., 2011; Wang et al., 2014]. For example, the accuracy of NCC algorithm will be significantly affected by the "pixel-locking" effect , the phenomenon of which denotes that the subpixel estimates bias toward intergral pixel positions [Tong et al., 2015]. And also, the square shaped correlation window used during the matching process will result in fattening effect (i.e., the "stair-like" boundaries of object in the disparity map after matching) [Wang et al., 2014], which will reduce the accuracy and resolution of the tracking result. Although the offset measurements are less accurate than the InSAR phase measurements, offsets tracking have been proven to be effective when the ground displacements are large and discontine [Hu et al., 2014b].

Therefore, it can be concluded that different methods complement each other, and the choice of the appropriate method depends on the available data , the degree of expected interferometric coherence, the size, surface conditions and flow velocity of the glacier, and the required accuracy and spatial resolution [Schubert et al., 2013].

2.2   Despeckling and Denoising

Despite that SAR images have become more and more popular in remote sensing fields, the speckle, which is a kind of multiplicative signal that diminishes quality of signal and increases the burden of image interpretation [Ansari & Mohan, 2014; Yommy et al., 2015], is always a significant drawbacks hindering the further application of SAR image, especially for high resolution SAR data [Goodman, 1976; Lee, 1986].

To solve this challenging problem, plentiful operators such as the well-known Lee filter [Lee, 1980], Kuan filter [Kuan et al., 1985], and nonlocal mean based filters [Buades et al., 2005] have been developed as standard filters to despeckle or denoise SAR images and they have already been validated in many cases [Yommy et al., 2015]. Briefly, commonly used despeckling methods can be roughly classified into two categories: local filters and non-local ones.

Local filters utilize pixel information within a vicinity of the center pixel, (e.g., a square window). Boxcar filter, averaging all the pixels in the sliding window, is one of the simplest ones. Besides the way of directly averaging all the pixels in the local window, an adaptive selection of useful pixels is also reasonable. Lee filter [Lee, 1980] is also a well-known and representative local adaptive filter. It considers more about the statistics information than the pixel value

itself. However, for the filters, one of the most difficult challenges is to preserve the edges when despeckling [Lee, 1981]. The essential objective of any despeckling technique is to suppress the speckle signal in the image and keep edges, texture, and other features in the image, simultaneously [Kuan et al., 1985]. To that end, in Lee et al. [1999], the improved Lee filter was developed by introducing edge-aligned masks of various shapes, so that the orientated edges of image patterns can be preserved as much as possible. The exact shape of the mask used is adaptively determined by the gradient information of the pixels inside the window.

In contrast, the non-local filter was firstly introduced in Buades et al. [2005], which complements the local information in local filters. Experiments and research have demonstrated that the non-local means filter is capable to keep a good balance between noise reduction and feature preservation. The non-local means filter [Buades et al., 2005] is one of the most representative ones, taking a mean of all pixels in the image, weighted by how similar these pixels are to the target pixel. The key idea of the non-local based filters lies in the similarity measure of two pixels. However, this similarity measuring process normally requires large computation costs, which may significantly degrade the efficiency of the non-local based methods.

Therefore, an excellent speckle removal filter should make the suppression of noise be balanced with the ability of effectively reserving fine details and features in the image [Xiao et al., 2003], and also have an acceptable efficiency of computation.

2.3 Reviews on Image Matching Techniques for Offset Estimation

2.3.1 Spatial Domain Correlation Method

The area-based matching or correlation techniques are the most commonly used method due to its relative simplicity and reliability [Lewis, 1995; Zitova & Flusser, 2003].

Among all the popular techniques, the cross-correlation based methods are the representatives. For example, normalized cross correlation (NCC) algorithm, which accounts for the normalized form of brightness and contrast in matching patches, is one of the most widely used similarity measure criteria in the field of image processing due to its reliability and simplicity [Lewis, 1995]. However, beside the simplicity and reliability, the NCC still has been reported for numbers of drawbacks [Lewis, 1995; Scambos et al., 1992; Zhang & Gruen, 2006]. For instance, NCC is sensitive to noise and significant scale, rotation or shearing differences between the images to be correlated [Debella-Gilo & Kääb, 2012]. The computation cost of cross correlation based method is also a heavy burden for large scale image processing as well. To overcome these drawbacks, several improved cross-correlation algorithms have been achieved. For example, the zero mean normalized cross correlation (ZNCC) [Stefano et al., 2005] considers the subtraction of the local mean and tolerates uniform brightness variations, which make the ZNCC provides better robustness than the NCC [Faugeras et al., 1993; Tsai et al., 2003] when dealing with noise contaminated image.

Moreover, theoretically, the precision of cross correlation method is limited to integer pixel level, and thus varies with the pixel size of the image patches. The sub-pixel level accuracy can only be achieved via further refinements. To be specific, there are two common approaches can be used for achieving sub-pixel accuracy [Debella-Gilo & Kääb, 2011]. The first one is based the up-sampling idea, which resample the image to a higher spatial resolution through interpolation, so that a small pixel size can be obtained that increasing the accuracy indirectly [Szeliski & Scharstein, 2002]. While the other one is to directly interpolate or fit the 3D surface formed by correlation coefficient value after the cross correlation process, in order to locate the correlation peak with sub-pixel precision [Scambos et al., 1992; Althof et al., 1997].

Least square matching (LSM) is also a renowned area-based spatial domain method, which was firstly used in the field of photogrammetry (Gruen, 2003) for the application of DEM generation. Compared with cross correlation based methods, LSM features its capability to deal with scaling and rotation deformation of images [Debella-Gilo & Kääb, 2011] and can achieve extremely high accuracy in some cases. In essence, the LSM can be categorized as a process of nonlinear regression [Li & Wang, 2014], since it uses the grey values of image patches as the input observation and combines affine transformation model and linear radiometric model. To apply the least square algorithm to this a nonlinear model, the Taylor linearization transfers is introduced to transform the nonlinear model into the linear one [Li & Wang, 2014].

Since the creation, a wide variety of researches and explorations has been made to improve the performance and feasibleness of LSM. For example, new projective transformation models have been introduced in the functional model to improve the adaptability [Bethmann & Luhmann, 2011]. Considering the sensitiveness of least square algorithm, in some work, the robust estimators can also be used in the functional model for eliminating outliers [Li & Wang, 2014]. However, since the LSM requires an iteration process, it always has a larger computation cost compared with cross correlation based ones. Therefore, in practice, LSM generally act as refine step in a matching process, for example, the last step for refinement of matching results in a Pyramid-based matching strategy [Debella-Gilo & Kääb, 2012]. So that the computation cost resulting from iterations can be largely reduced.

2.3.2   Phase Correlation Method

Compared with these area-based correlation methods, phase correlation (PC) is a Fourier-based matching technique, which is considered to be more accurate and effective than some popular correlation based methods such as aforementioned NCC [Heid & Kääb, 2012; Foroosh et al., 2002].

The phase correlation has been successfully adopted in a diverse applications in the fields of image matching, including super-resolution reconstruction [Vandewalle et al., 2006], medical image registration [Hoge, 2003], motion tracking [Ho & Goecke, 2008], digital image stabilization [Kumar et al., 2011], mosaicking [Pan et al., 2009], fingerprint matching [Ito et al., 2004], 3-D construction [Muquit & Shibahara, 2006], and video analysis and processing [Dai et al., 2006; Paul et al., 2011] et al. In addition, phase correlation has also drawn increasing attention in the remote sensing community, in applications such as pixel to pixel coregistration [Liu & Yan, 2008], narrow baseline DEM generation [Morgan et al., 2010], in-flight calibration [Leprince et al., 2008; Jiang et al., 2014], and surface dynamics measurement, such as coseismic deformation measurement [Leprince et al., 2007; Gonzalez et al., 2010] and glacier displacement survey [Heid & Kääb, 2012; Scherler et al., 2008].

Generally, the existing researches on the subpixel phase correlation methods can be classified into two typical categories [Foroosh et al., 2002; Leprince et al., 2007]. The first category estimates the translational parameters by precisely identifying the main peak location of the IFT (inverse fourier transform) of the normalized cross-power spectrum. Whereas, the second category calculates the relative displacement by estimating the linear phase difference directly in the Fourier domain.

- In the former category, interpolation based methods are the most commonly used approaches for subpixel level offsets estimation. Interpolation methods with a 1-D parabolic function, Gaussian function, sinc function, and modified esinc function were employed with the locations of three peaks in the normalized cross-power spectrum, including the main integer

peak and its two neighboring side peaks in Ren et al. [2010]. However, these simple inter-
polation methods are sensitive to noise and other sources of gross errors [Ren et al., 2010].
Meanwhile, their accuracy is highly dependent on the data quality and interpolation algo-
rithms [Foroosh et al., 2002]. In [Foroosh et al., 2002], an assumption was given that images
with subpixel shifts were originally displaced by integer values in a higher resolution image,
and followed by a downsampling process. According to this assumption, in the case of a
subpixel shift, the signal power will not concentrate in a single peak rather be distributed
like several coherent peaks, with the most eminent ones closely neighboring to each other
[Foroosh et al., 2002]. This phenomenon implies that the signal power of phase correlation
results in a downsampled 2-D Dirichlet kernel. Compared with the methods in Abdou [1999]
and Ren et al. [2010], the method of Foroosh deduces a closed-form solution for the subpixel
estimation by utilizing a sinc function to approximately mimic the Dirichlet function, and is
thus more analytically demonstrable. However, it has been claimed that Foroosh's method
insufficiently takes the interference term during the analytical derivation into consideration.
Using only one-sided information will lead to the method being subjected to the negative
effect of noise [Ren et al., 2010; Foroosh & Balci, 2004]. In Nagashima et al. [2006], a
so-called peak evaluation formula (PEF) deduced from the sinc function fitting in one di-
mensions was introduced, through which the subpixel displacement can be obtained from
multiple tri-tuples consisting of the main peak and its corresponding surrounding points,
requiring merely least squares estimation without any iterative process.

- In the latter category, in light of the fact that the phase shift angle is a linear function of
  the shift parameters, and represents a 2-D plane mathematically, Stone et al. [2001] utilized
  least squares adjustment to fit the 2-D plane, with the high-frequency and small-magnitude
  spectral components cut off [Vandewalle et al., 2006]. However, the phase shift angle is 2Π
  wrapped in two dimensions, so as to only shifts of less than half a pixel can be estimated. For
  such reasons, two separate and consecutive 1-D unwrappings in the u-and v-directions were
  performed in Foroosh & Balci [2004]. A robust plane fitting approach, the quick maximum
  density power estimator, was applied in [Morgan et al., 2010] and [Liu & Yan, 2006] to make
  the estimation more reliable. Similarly, Tong et al. [2015] adopted maximum kernel density
  estimator to fit the 2-D phase plane for the improvement of robustness. In [Hoge, 2003],
  Hoge proposed a straightforward approach using singular value decomposition (SVD) to
  find the dominant rank-one approximation of the normalized cross-power spectrum matrix
  before 1-D phase unwrapping and linear fitting. Keller & Averbuch [2007] developed a
  robust extension to [Hoge, 2003] with a so-called 'projection' masking operator, under the
  assumption that the noise is additive white Gaussian noise. However, this method achieves
  a poor improvement in practical applications. To make the SVD based PC [Hoge, 2003]
  more robust, Tong et al. [2015] applied local optimized random sample consensus (RANSAC)
  algorithm to the 1-D linear fitting getting improved result. Nonlinear optimization is another
  commonly used direct approach for solving subpixel displacement. Leprince et al. [2007]
  provided an effective method based on nonlinear optimization, and they minimized the
  Frobenius norm of the difference between the measured cross-spectrum and the theoretical
  one weighted by adaptive frequency masking, using a two-point step size gradient algorithm.

Many researchers have already employed PC based algorithms for the matching between SAR
images in a broad range of applications. In [Michel & Rignot, 1999], a comparison between
phase correlation and interferometry for monitoring the flow of glacier is given, in which the PC
performs better for rapid ice flow and more robust to temporal changes in glacier scattering, and
measures two dimensions velocity using only one image pair. In some cased, the Fourier-Mellin
transform based on PC were applied to the single-frequency, repeat-pass, and dual-frequency SAR

imagery for an accurate registration in [Abdelfattah & Nicolas, 2005]. In [Karvonen et al., 2012; Wohlleben et al., 2013; Komarov & Barber, 2014], the sea ice motion is detected and computed via traditional PC algorithm for a measurement in pixel-level accuracy.

Nevertheless, the PC algorithm used for SAR image still meet several problems. In many researches, for example, the work of Komarov & Barber [2014], the motion of sea ice are obtained with integer pixel accuracy via PC which is lower than conventional NCC algorithm with sub-pixel accuracy [Wang et al., 2014]. Moreover, the SAR intensity imagery is always contaminated by multiplicative noise in high frequency domain [Lee, 1989], which is detrimental to robustness of the result of PC And also, the large and discontinue deformation of the glacier surface will also make a negative impact on the measurement using PC algorithm on account of the errors of unwrapping process required by large deformation measuring via PC principle. Therefore, with respect to the application of glacier monitoring, the PC algorithm for SAR imagery should possess the abilities of being both robust and accurate.

2.4   Glacier Surface Area Classification

Accurate and instant information about changes of snow and ice covered areas, proven to be closely in response to climate changes and sea-level rise, plays also a vital role in hydrological and climatological research and implications. Consequently, considering strong spatial and time dependent dynamics of the snow and ice cover in research areas, regular and frequent observation techniques with large coverages are in urgent need for the monitoring tasks.

To that end, the optical sensors, including multispectral, hyperspetral and infrared sensors, have been extensively used to map snow or ice cover areas in light of their unique reflectance characteristics appearing different spectral bands [Paul et al., 2002, 2004; Kargel et al., 2005; Rastner et al., 2014]. All the related work based on optical images utilizing the distinctive spectral reflectance difference of ice and snow between the shortwave infrared (SWIR) and the high reflectance in the visible spectrum (VIS) to identify glaciers [Dozier, 1989] have shown impressive results. However, there are still several factors that have hampered the application of visible sensors: (i) optical remote sensing requires good illumination conditions, cloud-free viewing, and appropriate gain settings to yield image data of good quality for glacier mapping, which are problematic in some regions especially in rugged mountainous areas; (ii) mapping with glaciers covered by debris using optical images, which confirmed as a major error source, is considered to be a bottleneck in glacier mapping and inventory due to the differentiation of spectral characteristics between glacier and surrounding ground is extremely subtle [Bhambri et al., 2011; Paul & et al., 2013]; and (iii) it is difficult to discriminate snow from ice due to the fact that they have similar spectral properties in glacier areas [Gupta et al., 2005].

In the last decade, remotely sensed SAR images are more and more popular to be applied on measuring the glacier surface facies. Theoretically, the SAR backscattering contributions of glacier ice and snow rely on signal wavelength, polarization and incidence angle. For example, a surface scattering component are affected by the dielectric and geometric properties (surface roughness, morphology, shape and grain size), while that of a volume scattering component will be influenced in the presence of internal reflectors such as ice crystals and crevasses. As for the electromagnetic wave frequency used by spaceborne and airborne SAR, it is not easy to discriminate the dry snow covered area which is transparent at C-band from the bare ground. In contrast, wet snow changes the backscattering behavior significantly, resulting in low backscatter coefficients (BC) which provides capabilities for "snow line" detection between wet snow areas and bare ice covered ground [Baghdadi et al., 1997; Huang et al., 2013].

Researchers have been investigating and studying about potentials and capabilities of SAR for glacier snow and ice applications over last few decades, and consequently methods of two main categories have been proposed on the basis of single or multi polarization property.

- The first one is the methods using single polarization SAR images: Based on the investigation of SAR radiometric signature differences on glacier zonations [Engeset & Weydahl, 1998; Rott & Mätzler, 1987], researchers can map wet snow coverage area and detect snow/firn lines via manualy chosen thresholds of BC according to experimental data or prior knowledge [König et al., 2002, 2004; Brown, 2012; Huang et al., 2013]. Alternatively, this can also be achieved by the use of ratio between BC of melting snow period and another reference snow-free image according to the reduced BC from the snow coverage area when compared to that without snow [Baghdadi et al., 1997; Venkataraman et al., 2008]. However, due to similar backscatter characteristics, glacier ice and its surrounding ground are difficult to be discriminated from each other [König et al., 2001]. For such cases, optical data are used as a complement of SAR images [Jaenicke et al., 2006], and InSAR pair can also be added to derive coherence information which helps the discrimination between glacier and non-glacier [Shi et al., 1997; Atwood et al., 2010]. Nevertheless, optical data have several limitations as we discussed before and temporal coherence loss is also an unavoidable problem in InSAR application especially in glacier area affected by meteorological and flow characteristics (i.e., ice and snow surface melt, snow and rain fall, wind-provoked snow drift, fast flow rate). Furthermore, these procedures require additional data set hampering their application.

- The second one is related to the approaches utilizing multiple polarization SAR images: Compared to single-channel SAR, the inclusion of SAR polarimetry can provide capability for the optimization of the polarimetric contrast and other polarimetric parameters significantly improving the quality of the data analysis [Shimoni et al., 2009]. The accuracy of wet snow mapping is greatly improved in [Singh et al., 2014], as the method of which is proposed based on polarization fraction representing ratio between to the maximum receiving power and the minimum power from radar channels within a resolution cell. However, it is still problematic for discrimination of the snow from bare surfaces or water bodies. Locations of boundaries between glacier facies are monitored by an unsupervised contextual non-Gaussian clustering algorithm using a series of dual-polarization C-band ENVISAT ASAR images achieving an classification accuracy of around 80% with only three glacier facies under the prerequisite of manually masking out mountains and isolating the glacier pixels [Akbari et al., 2014]. In Li et al. [2012], using C-band RADARSAT-2 quad-polarization SAR data and support vector machines (SVM) , the land cover map over glacier area or wet snow line is derived with an overall accuracy of 70.75%. Moreover, it can be increased to 91.1% by applying target decomposition, aiming to extracting physical information from the observed scattering of microwaves by both surface and volume structures [Huang et al., 2011].

All the methods mentioned above based on single polarization SAR data are pixel-based ones depending on various SAR backscatter characteristics of resolution cells from different classes. However, in the frequencies ranging from 1-12 GHz used by spaceborne and airborne SAR systems, it is difficult to distinguished glacier ice from surrounding areas at a single frequency with a fixed polarization as described by other researchers [Shi et al., 1994; König et al., 2001]. At the first glance, polarimetric sensor providing more information per pixel than single-polarization data seems to enable better land cover discrimination ability over glacier areas [Akbari et al., 2014]. However, single-polarization mode has a long history for monitoring purpose such as change detection on earth surface providing a huge amount of data archives. It is worth to study on the

potential of single-polarization SAR data on glacier research, which could also be extended for a long term monitoring purpose.

2.5 Sparse Representation for Object Classification

Sparse representation over a redundant dictionary is becoming a popular way of representing the data and has already attracted attentions in the communities of signal processing and machine learning. It is assumed that a signal of interest can be modeled as a linear combination of a few elements in a given dictionary, and the data can be explicitly mapped into a higher order sparse feature space. Classic applications of sparse representation are often based on a data driven strategy. Namely, the signal of interest is expected to be re-expressed or reconstructed by exploring the sparse assumption, such as denoising, impainting, and superresolution, cf. [Aharon et al., 2006; Hawe et al., 2013; Yang et al., 2012]. Recently, sparse representation has been demonstrated about its promising potentials on different kinds of datasets, with respect to specific tasks, such as learning or constructing dictionaries for face recognition [Wright et al., 2009], handwritten digit classification [Gao et al., 2012], texture categorization [Yang et al., 2014], pets (i.e. dogs and cats) classification [Bufford et al., 2013], digital art authentification [Mairal et al., 2012], and human action recognition [Guha & Ward, 2012], etc.

Thus, considering the aforementioned work related to the sparse representation, we can conclude that the sparse representation is often interpreted as the transformed features to promote the task of learning discrimination, and the structure in sparse domain is believed could make the hidden patterns easy to be captured. On behalf of this benefit of structure in sparse domain, the sparse representation based methods could be efficient tools for glacier classification tasks in SAR images.

Theoretically, the SAR image classification can be regarded as a high-dimensional nonlinear mapping problem [Zhang et al., 2015]. From the point of view in the remote sensing field, which mainly focuses on a large scale investigation on natural scenario, the analysis of physical mechanism about the classification problem seems to be not so significant. Thus, we mainly adopt image processing algorithm and machine learning methods to complete this SAR image classification task, with a natural scenario, e.g., glacier.

As for the classification, the sparse representation-based has been proved to be rather efficacious. In Thiagarajan et al. [2010], a target classification method based on SR is proposed. Its results show that the classification performance slightly outperforms the similar SVM based classification method, with the same training and testing sets adopted. More than that, the complexity has been reduced by decrease the dimensionality of the data sets via the theory of random projections. The experiments also demonstrated that such a significant reduction of complexity is achieved by trading off only a small loss in classification performance. In Feng et al. [2014], the feasibility of classifying PolSAR images with sparse representation-based classification methods is investigated. In their work, the features for classification are generated with various polarimetric parameter extraction methods, and the supervised classification algorithm is adopted. Then, a dictionary for the SR of test samples is constructed, with polarimetric feature samples of labeled pixels trained, which is followed by the classification process. However, the polarimetric feature vectors, which are generated through the projection, are treated as a disarranged list of signals. It means that the contextual information around the target pixels in the PolSAR image contributes nothing to the feature generation process [Feng et al., 2014].

However, in general cases, neighboring pixels in a remote sensing image probably belong to the same class. Therefore, the classification accuracy is likely to be improved when contextual information is taken into account. For example, we can use a patch of pixels around the target pixel

as the smallest element for the classification. In [Ruan et al., 2016], a novel multi-scale sparse representation approach for SAR target classification is proposed. Unlike the aforementioned methods with single-scale methods, it firstly extracts the dense scale-invariant feature transform (SIFT) descriptors on multiple scales, then trains the global multi-scale dictionary by sparse coding algorithm. By using features with multiple scales, the proposed method can reach a better classification performance than that of single-scale ones. However, once the feature of target is high-dimensional, the multiple scale strategy may suffer a challenge of computation cost when solving optimization problem.

Therefore, we hope that we could find a sparse representation based classification method can combine the multi-scale strategy with the dimension reduction approach, so that we can extract effective features from the SAR image and reduce the computation cost simultaneously.

2.6 Contribution of this Thesis

This thesis focuses on glacier monitoring via two important aspects, namely glacier surface velocity, and areas of glacier facies. Comparing with the methods summarized in Section 2.1 and Section 2.4 dealing with glacier motion and glacier zones detection, the contribution of this thesis can be divided into two parts separately as follows.

2.6.1 Glacier Surface Motion Estimation

In this context, the contribution of this part is to provide a processing chain for the estimation of glacier surface motion using repeated spaceborne SAR intensity images. The main contributions which are specific to measuring the glacier surface motion include:

- A dense matching method based on point like feature in SAR intensity images is developed for a robust workflow for estimating the dense glacier motion map.

- An improved robust phase correlation algorithm combing the RANSAC algorithm with singular value decomposition is utilized for matching SAR images, which can cope with strong speckles and increase the matching accuracy between small patches.

- An adaptive refined version of Lee filter is developed for the despeckling of SAR images, while the sharpness and details of image patterns can be preserved.

- The feasibility and superiority of proposed motion estimation approach from high resolution SAR are demonstrated and endorsed by both synthetic and real datasets.

2.6.2 Glacier Areas Classification

With respect to the detection of glacier areas, a classification method inspired by the benefit of structure in sparse domain is proposed. The key assumption of this method in this context is that the sparse representations contain appropriate information for objects discrimination. Under this assumption, discriminative features are directly learned on sparse representations. The dictionary and the linear projection for data representation and task of classification are alternatively learned, respectively. The following items are the core contributions that are specific to the approaches proposed in this theis:

- Extend the existing methods using single-polarization SAR data for glacier facies detection by two-layers learning discriminative features using sparse representations.

- The method is constructed based on the relationships between target pixel and its neighboring pixels, which focuses on the local geometry of image patches. Additionally, the proposed method can avoid the worst case of misclassification among the points that share the distance similarity but from different classes.

3   Estimation of Glacier Surface Motion

An overall workflow of proposed glacier motion estimation approach is shown in Fig. 3.1. As illustrated in Fig. 3.1, the workflow consists of three main phases: (1) Pre-processing of TerraSAR-X (TSX) intensity image. (2) Dense matching of image pair. (3) Estimation of glacier surface motion.

In the pre-processing phase, the TSX intensity image pair is filtered by the proposed adaptive refined Lee (ARLee) filter, so as to reduce the speckles and preserve the details of texture as the same time. External DEM data are introduced for eliminating the topographic distortion caused by the oblique view angle of line of sight (LOS) of TSX. In dense matching phase, the TSX intensity images are firstly aligned via a registration process. Subsequently, point-like features are detected and selected from aligned image pairs acting as candidates for the following dense matching. Eventually, an accurate dense matching between conjugate point like features of the image pair is conducted via proposed robust PC algorithm. In the final phase, by measuring displacements between corresponding point like features, the 2D movements of glacier in horizontal plane are obtained. Based on these 2D displacements, the 3D motion and velocities of the glacier are reconstructed and estimated with the help of an imaging model and parameters.

3.1   Preprocessing of SAR Images

For the preprocessing, the reduction of speckles and the correction of topographical distortions of TSX intensity image are conducted. The former one is implemented through a filtering us-
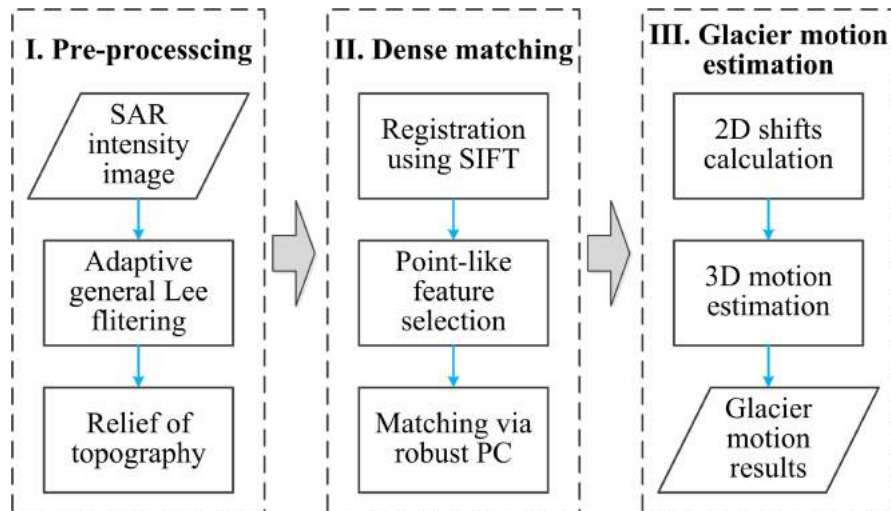

Figure 3.1: Overall workflow for the proposed glacier motion estimation approach.
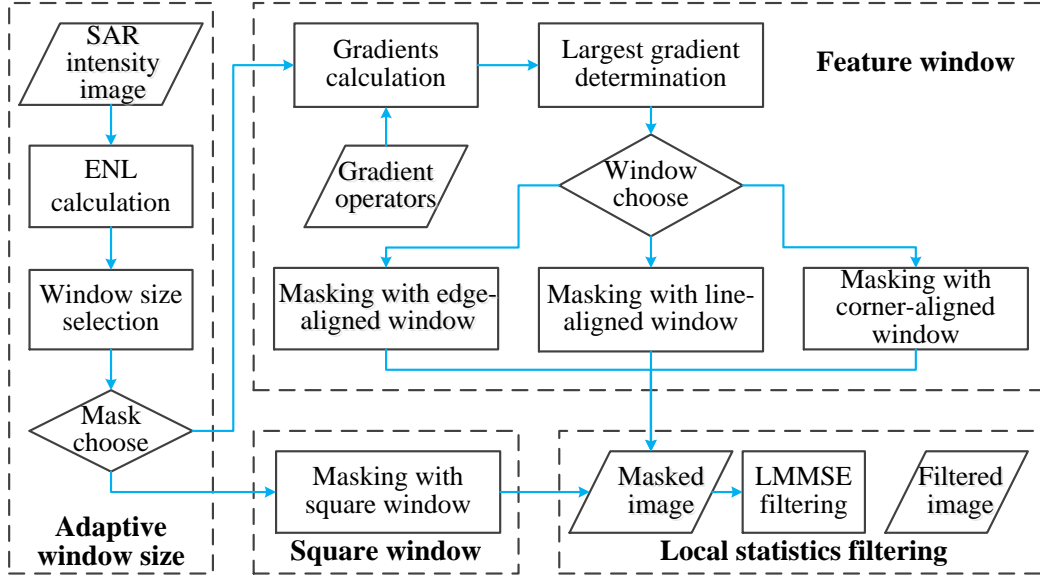
Figure 3.2: Filtering process of adaptive refined Lee filter.

ing proposed ARLee filter, whereas the later one is achieved by means of range-doppler terrain correction, with external digital elevation model employed.

3.1.1 SAR Images Despeckling and Denoising

Speckle, basically connecting to the interference of the returning wave at the transducer aperture, is a artefact intrinsically existing in the SAR imagery. The origin of this effect has been thoroughly analyzed in [Lee et al., 1999]. Speckle appearing as bright and dark dots in intensity image will apparently hamper the interpretation of SAR image, the accuracy of segmentation, image classification, object recognition and image registration. To decrease the influence of speckle and noise, an improved adaptive refined Lee filter is developed to suppress speckles as much as possible and in the meanwhile preserves the sharpness and features of image patterns.

ARLee filter is an improved version of the renowned refined Lee filter, where an adaptive filtering window size as well as the edge-, linear- and corner- aligned mask windows are adopted so that the edge, linear and corner features can be conserved while the speckles in homogeneous areas can be filtered. ARLee filter follows three core steps: adaptive determination of window size and type, selection of feature-aligned windows and local statistic filtering. The entire processing flow is illustrated in Fig.3.2. For the conventional refined Lee filter, the selection of filtering window size is crucial to the despeckling result. Generally, the larger the window is, the better the detailed features of image can be recognized and preserved, while the smaller the window is, in the homogeneous areas, the better the ability of despeckling is. Thus, in the proposed ARLee filter, a determination of window size based on the equivalent number of looks (ENL) is introduced [Lang et al., 2014], which are calculated through following equation:

$$ENL = \left(\frac{C_v}{C_y}\right)^2 \tag{3.1}$$

where C_v refers to the theoretical coefficient of variation (CoV) of imagery equaling to 1 for the single-look SAR intensity image, whereas C_y denotes the local CoV of the given filtering window. The search of optimized window size starts from the predefined maximum window to the minimum window, with their corresponding ENL calculated. The window size with largest ENL is chosen
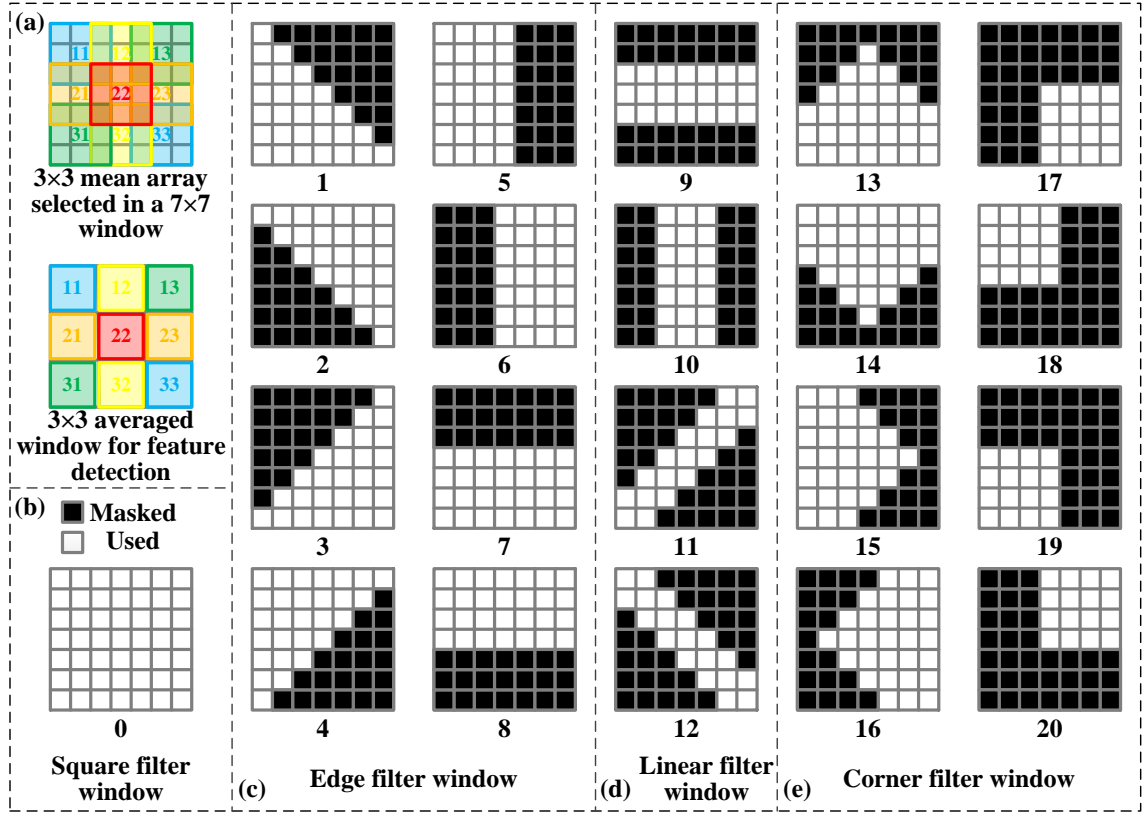
Figure 3.3: Filtering masks. (a) Mean array window. (b) Square windows used in the filter. (c)-(e) Feature-aligned windows used in the filter.

as the optimum, and a lower bound threshold of ENL is given as well. If ENL is lower than the given threshold, the filtering area is highly likely to be homogeneous area, so that in the following step a square mask window shown in Fig. 3.3(b) will be adopted.

The feature-aligned windows are designed to preserve the detailed features in image. Similar to the refined Lee filter, the optimized filtering window is segmented into nine 3×3 sub-windows and their mean values are computed as shown in Fig. 3.3(a). For the feature detection, besides edges used in refined Lee filter, linear and corner features are also taken into consideration, which correspond to the feature-aligned window shown in Fig. 3.3(d) and (e). To determine what kind of feature is and which type of feature-aligned window should be used, the Prewitt gradient operator and its variants are adopted. In Fig. 3.4, six examples (I to VI) coinciding to the windows of numbers 1, 5, 9, 11, 13 and 17 in Fig. 3.3 are given. The gradient operators are then convoluted with 3×3 mean array of filtering windows and their gradients are computed. The feature-aligned window connecting to the operator with largest gradients will be selected as optimum for masking.

Afterwards, the local statistics filter on the basis of linear minimum mean square error (LMMSE) algorithm is applied to the masked filtering window, which can be expressed as following:

$$\hat{x} = \overline{y} + w \cdot (y - \overline{y}) \tag{3.2}$$

$$\begin{bmatrix} 0 & -1 & -1 \\ 1 & 0 & -1 \\ 1 & 1 & 0 \end{bmatrix} \quad \begin{bmatrix} 1 & 0 & -1 \\ 1 & 0 & -1 \\ 1 & 0 & -1 \end{bmatrix} \quad \begin{bmatrix} -1 & -1 & -1 \\ 1 & 1 & 1 \\ 0 & 0 & 0 \end{bmatrix}$$
$$\text{I} \qquad\qquad\qquad \text{II} \qquad\qquad\qquad \text{III}$$

$$\begin{bmatrix} -1 & -1 & 1 \\ -1 & 1 & 0 \\ 1 & 0 & 0 \end{bmatrix} \quad \begin{bmatrix} -1 & -1 & -1 \\ -1 & 2 & -1 \\ 1 & 1 & 1 \end{bmatrix} \quad \begin{bmatrix} -1 & -1 & -1 \\ -1 & 2 & 1 \\ -1 & 1 & 1 \end{bmatrix}$$
$$\text{IV} \qquad\qquad\qquad \text{V} \qquad\qquad\qquad \text{VI}$$

Figure 3.4: Gradient operators used in the filter in accordance with some feature-aligned windows in Fig. 3.3.

where $\hat{x}$ refers to the filtered pixel value, y is the center pixel value of window, $\overline{y}$ is the local mean of window and w is the weighting function having a value ranging from zero to one. The weight parameter can be computed by:

$$w = \frac{var(y) - \overline{y}^2 \cdot \sigma_v^2}{(1 + \sigma_v^2) \cdot var(y)} \tag{3.3}$$

Here $var(y)$ is the local variance and σ_v is a measure of speckle level and has been proven to be the standard to mean ratio for homogeneous areas.

3.1.2   Elimination of Topographic Information

Since TSX sensor is an oblique scanning imaging system, ground topography will lead to geometric distortions (e.g., foreshortening and layover) in SAR image data [Stilla et al., 2003]. The geometric principal of topographical distortions in SAR imagery is shown in Fig. 3.5. Seen from the sketch that point P with elevation h is imaged at position P' in the SAR image, with its correct position should be at position P''. Here, the offsets Δr between P' and P'' reveal the topographic distortions. Consequently, before the dense matching procedure, a removal of topographic distortion via range-doppler terrain correction with external DEM data is conducted to orthorectify the intensity image.

The range and Doppler equation are shown as follows:

$$(S_x - P_x)^2 + (S_y - P_y)^2 + (S_z - P_z)^2 = R^2 \tag{3.4}$$

$$\frac{2}{\lambda} \cdot \frac{\overrightarrow{S} - \overrightarrow{P}}{|\overrightarrow{S} - \overrightarrow{P}|} \cdot (v_p - v_s) = f_D \tag{3.5}$$

where $\overrightarrow{S}(S_x, S_y, S_z)$ and $\overrightarrow{P}(P_x, P_y, P_z)$ refer to the positions of SAR sensor and ground point, v_p and v_s stand for their velocities, R and f_D are the reference slant range and image Doppler respectively, and λ is the wavelength. Topographical offsets Δn_r and Δn_a in range and azimuth can be expressed as follows:

$$\Delta n_r = \frac{2f_s}{v_c} \cdot (R - R'') \tag{3.6}$$

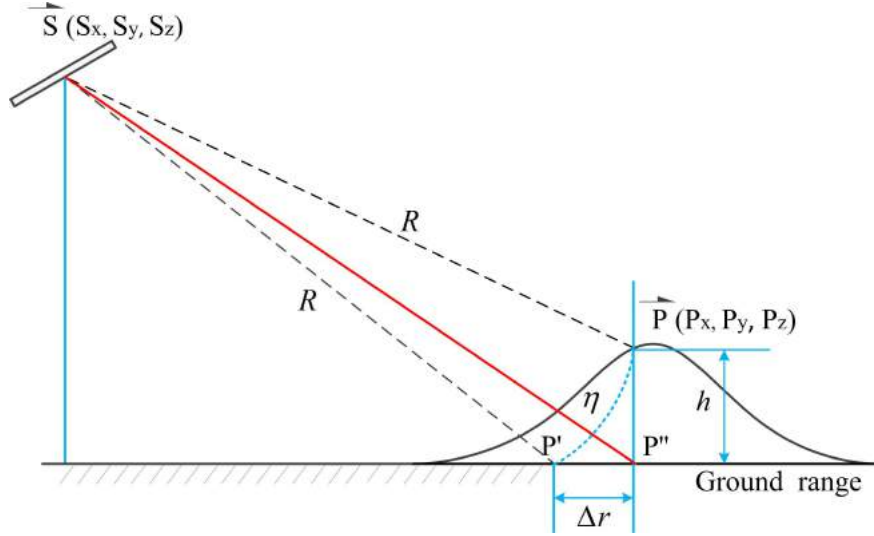$$\Delta n_a = [f_D(R) - f_D(R'')] \cdot \frac{f_p}{f_R} \tag{3.7}$$

Figure 3.5: Sketch of topographical mapping of SAR in ground range geometry [Stilla et al., 2003].

where f_s and f_p are sampling frequency and pulse repetition frequency respectively, f_R refers to the Doppler frequency at range R and v_c stand for wave velocity. By introducing the height deviation h from the external DEM, offsets Δn_r and Δn_a in slant range and azimuth can be corrected through an iteration foreshortening process. Then, the corrected range and azimuth data in radar geometry will be converted to the orthorectified map frame via back projection. The external DEM used for this work was obtained from STRM X-band DEM. It has a spatial resolution of 25 m, which is oversampled onto 2.09 m grids for TSX strip mode (SM) data.

3.2   Dense matching between SAR image pair

After the preprocessing step, the dense matching process aiming at obtaining the 2D movements of glacier is performed. The entire dense matching process involves three steps: Co-registration of orthorectified TSX image, selection of PLF and matching using robust PC algorithm. In Fig. 3.6, a detailed flowchart of dense matching process is given.

3.2.1   Co-registration

For the co-registration, first, the SIFT features are extracted from the SAR images. Then, an affine transformation model is generated and optimized with these features and least square adjustment. Finally, the image is resampled following the affine transformation model using two-dimensional cubic convolution interpolation.

3.2.2   Selection of Point Like Features

For the sake of solving the inevitable matching problems caused by the decorrelated areas and fattening effect appearing as patch-like offset patterns (Fig. 3.7, marked in red dash line box) from strong reflectors [Hu et al., 2014b], instead of matching uniformly distributed points (e.g., pixel-by-pixel matching), a PLF matching strategy is introduced to increase the accuracy and robustness of matching results.

To extract the PLFs, a 2D sinc-function template (Fig.3.8(a)) is cross-correlated with the intensity image to obtain a correlation map with its pixels value referring to correlation coefficients ranging from 0 to 1, because strong reflective targets will result in a 2D sinc-function like patterns
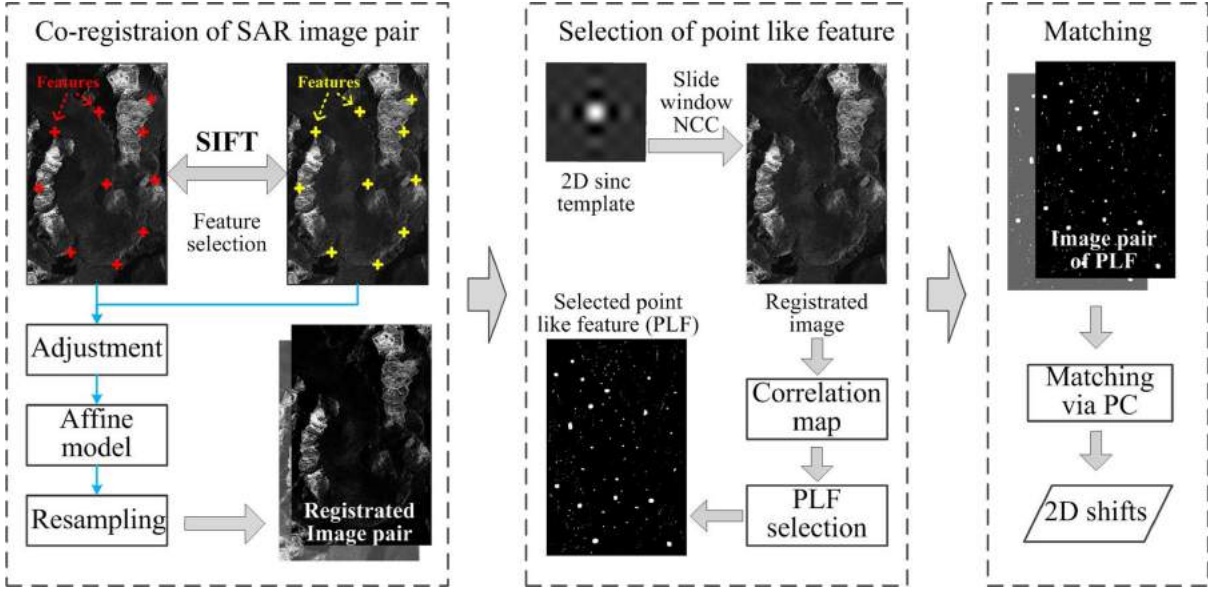
Figure 3.6: The flowchart of dense matching between SAR image pair.
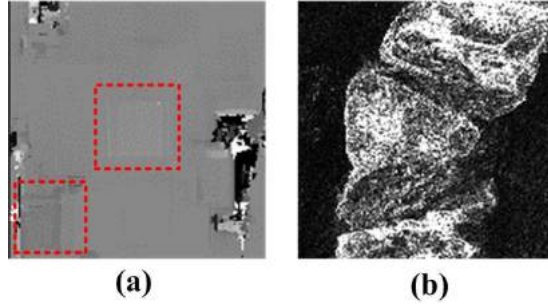
Figure 3.7: Fattening effect. (a) Fattening effect when using patch like template "pixel-by-pixel" correlation. (b) Original SAR imagery used in (a).

in SAR amplitude images due to side-lobes of the transmitted SAR beam [Hu et al., 2014b]. Accordingly, the correlation map is multiplied by the SAR amplitude image itself to restrain amplitudes of other pixels than the detected targets of PLFs. Moreover, the PLFs with a lower correlation value in the correlation map will be discarded, with a threshold based on local mean and standard deviation used. Finally, an image pair of PLFs (Fig. 3.8(c)) is gained for the following dense matching.

3.2.3   Robust Phase Correlation

According to the Fourier shift property, the shifts between two images in the spatial domain will result in a linear phase difference in the frequency domain after Fourier transform (FT) [Kuglin, 1975]. Two image functions relating to shifts x_0 and y_0 in the line and column directions are denoted as $f(x,y)$ and $g(x,y)$, and expressed as:

$$g(x,y) = f(x - x_0, y - y_0) \tag{3.8}$$

According to the Fourier shift property by means of the FT:

$$G(u,v) = F(u,v)e^{-i(ux_0 + vy_0)} \tag{3.9}$$
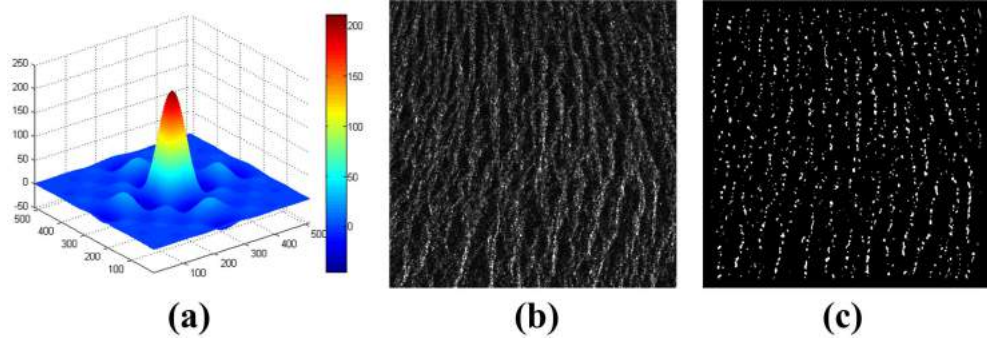
Figure 3.8: Illustrations for the selection of point like feature. (a) 2-D Sinc-function template. (b) Original SAR intensity imagery. (c) Image of point like features.
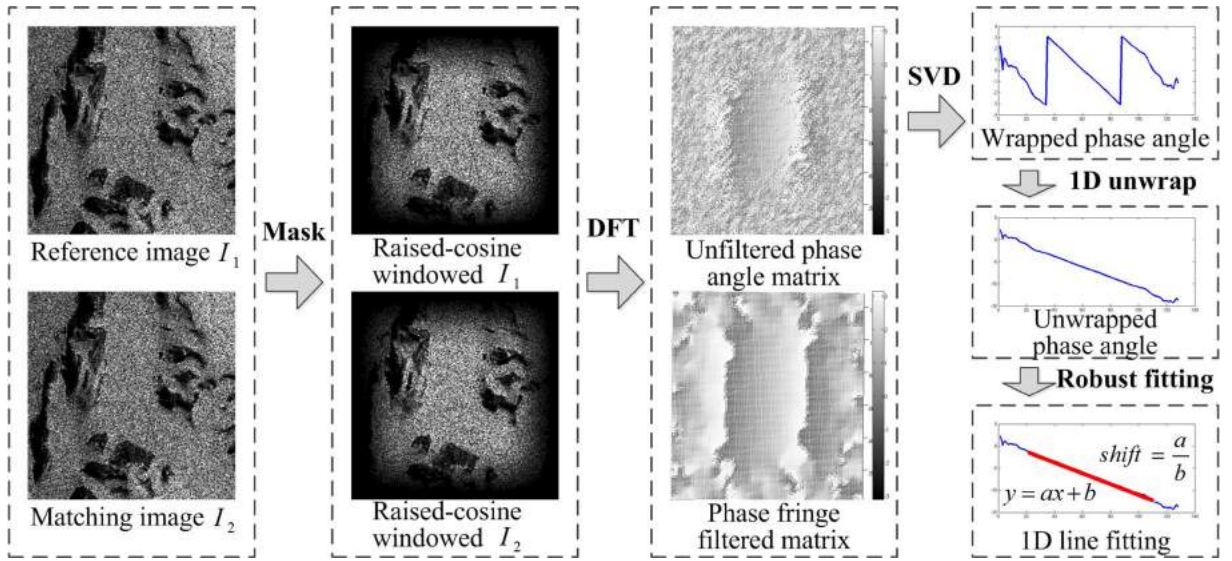
Figure 3.9: workflow of the proposed robust phase correlation algorithm.

where $F(u,v)$ and $G(u,v)$ are the corresponding FT of $f(x,y)$ and $g(x,y)$. The normalized cross-power spectrum matrix is given by:

$$Q(u,v) = \frac{F(u,v)G(u,v)^*}{|F(u,v)G(u,v)^*|} = e^{-i(ux_0+vy_0)} \tag{3.10}$$

where $*$ denotes the complex conjugate, and Q is the normalized complex matrix that only relates to the phase shift components of the two input images. It is therefore insensitive to illumination differences and image content. In the case of integer pixel shifts, the IFT of $Q(u,v)$ is a Dirac delta function centered on (x_0, y_0) , if $F(u,v)$ and $G(u,v)$ are supposed to be continuous functions (replaced by a unit impulse in the discretized case). Integer pixel shifts can therefore be estimated from the peak coordinates of the IFT of the normalized cross-power spectrum matrix [Kuglin, 1975]. In order to obtain the subpixel accuracy and ensure the robustness of estimation results, subpixel shift estimation directly in the Fourier domain is adopted in this paper. Here, we take advantage of the thought of SVD-RANSAC method [Tong et al., 2015], which jointly uses SVD and robust fitting algorithm (e.g., RANSAC).

In light of the fact that the normalized cross power spectrum matrix Q is theoretically separable, Hoge [2003] proposed an effective subpixel phase correlation method that simplifies the 2-D subpixel shift estimation between two images through SVD to find the best rank-one approxima-

tion of the normalized cross-power spectrum matrix Q. Therefore, 1-D unwrapping is performed on the the phase angle of the left and right domain singular vectors, and then the 2-D subpixel shift parameters can be estimated from the slope of unwrapped phase angles. The advantage of Hoge' method lies in avoiding the ill-posed problem of 2-D phase unwrapping in a theoretical manner. In addition, the implicit Eigen-filtering nature of identifying the dominant singular vectors of Q makes the method more reliable [Hoge, 2003]. However, the results of Hoge's method become inaccurate in several practical cases [Gonzalez et al., 2010], especially in the presence of aliasing and noise. For this case, Tong et al. [2015] proposed SVD-RANSAC method which integrates raised-cosine window, phase fringe filter and RANSAC algorithm into the original Hoge's method in order to enhance the robustness to corruptions and noise.

The workflow of the robust phase correlation algorithm is illustrated in Fig. 3.9 and described as follows. After the application of a 2-D raised-cosine window to avoid edge effects, we can safely apply the discrete fourier transform (DFT) to the weighted images before calculating the normalized cross-power spectrum matrix Q. Frequency masking proposed in [Leprince et al., 2007] and phase fringe filter [Morgan et al., 2010] can efficiently be used to reduce high-frequency noise and aliasing. Subsequently, SVD and 1-D phase unwrapping is performed to obtain the unwrapped phase angles. Finally, we can estimate subpixel shift parameters by means of robust line fitting. As stated in [Pham et al., 2014], hypotheses fitted on minimal subsets in standard RANSAC algorithm may be severely biased due to the influence of measurement noise, even if the minimal subsets contain purely inliers. The speckle of SAR images could make the unwrapped phase angles very noisy. Therefore, the robust strategy using higher than minimal subset sampling proposed in [Tennakoon et al., 2015] is adopted in this work to reduce the influence of noise.

Once the PLFs are extracted, the matching operation between the image pair of PLFs is carried out, with aforementioned robust PC algorithm applied. The displacements Δi, Δj in x- and y- direction on the image are achieved by comparing the coordinates of matched conjugate PLFs P_a and P_b from the image pair as shown in following equation:

$$(\Delta i, \Delta j) = P_b(i_b, j_b) - P_a(i_a, j_a) \tag{3.11}$$

3.3   Estimation of Glacier Surface Motion

In consonance with dense matching results, the 2D shifts (east- and north- directions) of glacier in the orthorectified plane will be converted to the 3D motion vector in three dimensions: east, north and elevation. Thus, the change in elevation direction should be estimated from the known 2D motion in east and north direction. To accomplish this, the 2D shifts in orthorectified planes are back projected and transformed to the shits in range and azimuth direction in SAR geometry. The relations between the shifts Δx and Δy in orthorectified plane and change value of range ΔR can be derived from Eq. 3.4 as follows:

$$\Delta R = [(S_x - P_x - \Delta x)^2 + (S_y - P_y - \Delta y)^2 + (S_z - P_z)^2]^{\frac{1}{2}} - [(S_x - P_x)^2 + (S_y - P_y)^2 + (S_z - P_z)^2]^{\frac{1}{2}} \tag{3.12}$$

In consideration of the relatively small changes in elevation, the deviation of range and azimuth value can be approximately connected to the variation of elevation following Eq. 3.13, with their relationships illustrated in Fig. 3.10.

$$\Delta R = \frac{\Delta h}{\cos(\eta)} \tag{3.13}$$

where ΔR and Δh refer to the deviation of range and change in elevation respectively and η stands for the angle of incidence of radar wave.
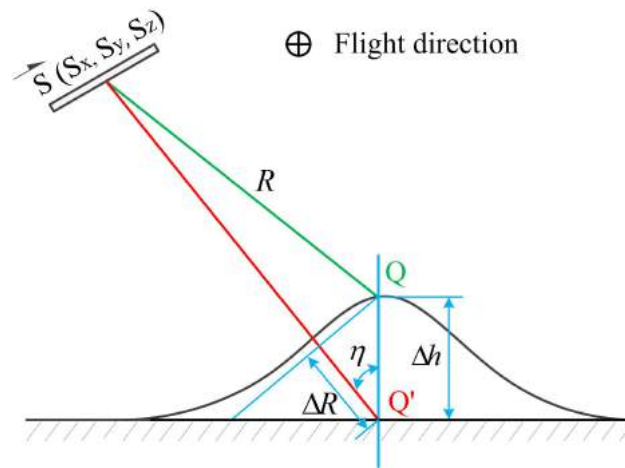
Figure 3.10: Relationships between the deviation of range and azimuth and change in elevation.

4 Classification of Glacier Surface Area

An overall workflow of proposed multi-classes classification on and around the glacier is shown in Fig. 4.1. As illustrated in Fig. 4.1, the workflow consists of three main phases: (1) Projecting image patches on to a unit sphere. (2) Learning dictionary for classification from the unit sphere. (3) Multi-classes classification via optimization of DPLC (learning dictionary and projection matrix for linear classification) .

One possible way to describe the relationships between neighboring pixels, as described in Section 2.5, is to adopt an extracted patch to represent the target pixel in its centre. In this work, we put an emphasis on the distribution of the pixels in each image patch, and ignore its intensity value. To achieve this, a method projecting all the training patches onto a unit sphere, i.e. all the patches have united length (see Fig. 4.1(a)), is applied. In the following part of this section, we propose an approach to exploit a simple and differentiable platform to solve target pixels classification problem via jointly learn a dictionary and projection matrix.

$X := [x_1, \ldots, x_n] \in \mathbb{R}^{m \times n}$ is defined as the data matrix containing n SAR image patches $x_i \in \mathbb{R}^m$. With respect to the supervised learning problems, the class label of the patch x_i is assumed to be $c_i \in \{1, 2, \cdots, c\}$, where c is the number of classes. Additionally, let l_i and n_i denote the index set and number of the samples belonging to the ith class, respectively.

Prior to give the proposed method, some technical details of dictionary learning are briefly recalled in Section 4.1, and then the proposed learning algorithms associated with a steepest gradient algorithm will be introduced.

4.1 Data-driven Dictionary Learning

Assuming that all data points $x_i \in \mathbb{R}^m$ admit sparse representations with respect to a common dictionary $D := [d_1, \ldots, d_k] \in \mathbb{R}^{m \times k}$, i.e.

$$x_i = D\phi_i, \qquad \text{for all } i = 1, \ldots, n, \tag{4.1}$$

where $\phi_i \in \mathbb{R}^k$ is the corresponding sparse representation of x_i. For the performance of algorithms exploiting this model, it is crucial to find a dictionary that allows the signal of interest to be represented most accurately with a coefficient vector ϕ_i that is as sparse as possible. Given a set of representative training signals, jointly learning the dictionary D associated with the sparse vector ϕ is called dictionary learning [Elad & Aharon, 2006; Hawe et al., 2013], which could be accomplished by solving the following minimization problem:

$$(D, \Phi) = \underset{D, \Phi}{\arg \min} \|X - D\Phi\|_2^2, \ \forall i, \|\phi_i\|_0 \leq s, \tag{4.2}$$

where $\Phi = [\phi_1, \phi_2, \cdots, \phi_n]$, s is a sparsity constraint factor.
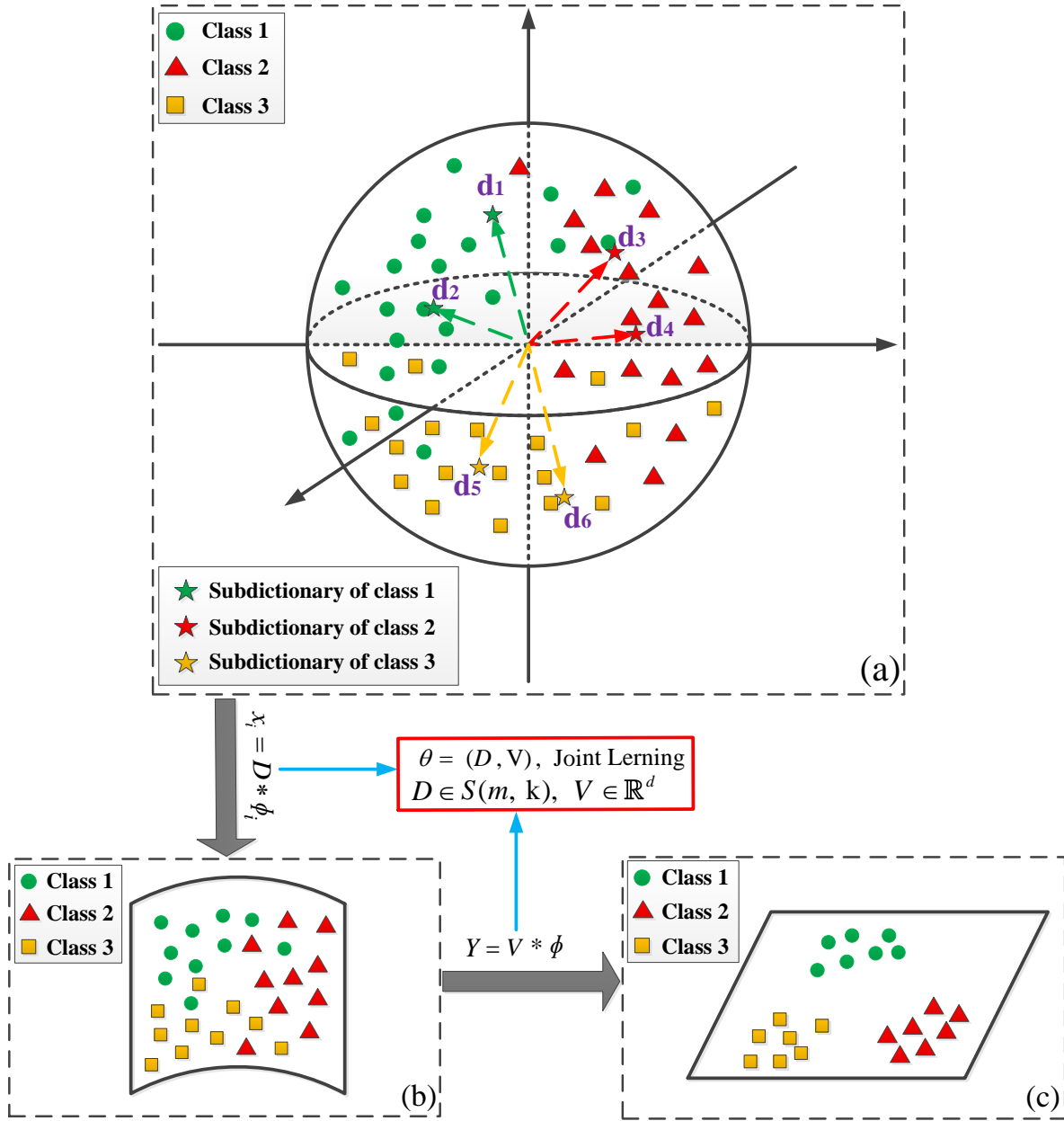
Figure 4.1: Workflow of two layers learning sparse representation. (a) Dictionary atoms and training data points. (b) Sparse codes. (c) Extracted features.

Given D, the sparse solution of an Lasso problem is confined, which is proposed in Efron et al. [2004], as

$$\phi_x(D) := \operatorname*{argmin}_{\phi \in \mathbb{R}^k} \tfrac{1}{2}\|x - D\phi\|_2^2 + \lambda_1\|\phi\|_1, \tag{4.3}$$

where $\lambda_1 > 0$ weighs the sparsity against reconstruction error. The set of indices of the non-zero entries of the solution $\phi^* = [\varphi_1^*, \ldots, \varphi_k^*]^\top \in \mathbb{R}^k$ is defined as

$$\Lambda := \{i \in \{1, \ldots, k\}|\varphi_i^* \neq 0\}. \tag{4.4}$$

Then the solution ϕ^* has a closed-form expression as

$$\phi_x^*(D) := \left(D_\Lambda^\top D_\Lambda\right)^{-1}\left(D_\Lambda^\top x - \lambda_1 s_\Lambda\right), \tag{4.5}$$

where $s_\Lambda \in \{\pm 1\}^{|\Lambda|}$ carries the signs of ϕ_Λ^*, $D_\Lambda \in \mathbb{R}^{m \times |\Lambda|}$ is the subset of D in which the index of atoms (rows) fall into support Λ.

4.2 Learning Dictionary for Classification

The sparse vector $\phi_x(D)$ can be directly used as a feature for classification. Without loss of generality, a regular classifier $g(\phi_x(D))$ can be obtained by determining its model parameters $W \in \mathbb{R}^{d \times k}$ satisfying:

$$\operatorname*{arg\,min}_{D \in \mathbb{R}^{m \times k}, W \in \mathbb{R}^{d \times k}} \sum_i \ell\{z_i, g(\phi_i(D), W)\} + \mu\|W\|_F^2. \tag{4.6}$$

where ℓ is the classification loss function, z_i is the label of x_i and μ is a regularization parameter (which prevents overfitting). Typical loss functions are mainly the least squares loss function [Jiang et al., 2013; Pham & Venkatesh, 2008], logistic loss function [Mairal et al., 2009], or square hinge loss [Yang et al., 2010].

In practice, the feature dimension k is normally high and, thus, it is needed and will be beneficial to transform the coefficients from the high-dimensional space to a low dimensional one for alleviating the curse of dimensionality. Consider V is a scale-invariant linear transformation and denote $y = V^\top x$. It further assumes the features in the space panned by V carry more extract information than the sparse domain. Above mentioned dimensionality reduction algorithms have been applied successfully to multi-class and multi-label problems.They are commonly applied as a separate data preprocessing step before classification algorithms (such as Nearest Neighbors (NN) classifier, Binary classifier or SVM classifier). In this subsection, a joint learning framework is investigated two layers dimensionality reduction and multi-label classification are performed simultaneously. It is shown that when the Supervised Neighborhood Embedding (SNE) [He et al., 2005] is used in classification, this joint learning decouples into two separate components, i.e., dimensionality reduction followed by multi-label classification [Sun et al., 2013].

4.2.1 Discriminative Features Extraction

In this method, the core idea is to find the discriminative distribution of the pixels in each image patch for each class. However, the intensity values also play an important for classifying the samples from intuitive observation. For example, relief ground and steep edge of the glacier facing the SAR sensor appear as patches with high brightness in the intensity images but the water appears to be darker. To be specific, for TerraSAR-X image used in our research, the average value of each pixel for wet snow, ice, water, NCR are in $(47, 82)$, $(82, 132)$, $(0, 47)$, $(380, max)$, respectively, see Fig. 6.17(a).

In order to take advantage of the information from intensity value,the neighbors for each batch are first constructed via both the labels and sum of absolute intensity values of patch vectors.

Let $\tilde{X} := [\tilde{x}_1, \ldots, \tilde{x}_n] \in \mathbb{R}^{m \times n}$ denote the data matrix containing n SAR image patches $x_i \in \mathbb{R}^m$ with original intensity values, and $X := [x_1, \ldots, x_n] \in \mathbb{R}^{m \times n}$ the data matrix with each point on a unit sphere, see Fig.4.1.

Given label c_i, let $N_{k_1}(\hat{x}_i)$ denote the set of k_1 nearest neighbors, which is calculated from $\tilde{X}$ and the corresponding weight matrix be $C \in \mathbb{R}^{n \times n}$, defined by

$$C_{ij} = \begin{cases} 1, & \text{if } \hat{x}_j \in N_{k_1}(\hat{x}_i) \text{ or } \hat{x}_i \in N_{k_1}(\hat{x}_j) \\ 0, & \text{otherwise.} \end{cases}$$

At a similar way, let $N_{k_2}^-(\hat{x}_i)$ denote the set of k_2 nearest neighbors among the data points whose labels are different to that of $\hat{x}_i$ in $\tilde{X}$.

$$C_{ij}^- = \begin{cases} 1, & \text{if } \hat{x}_j \in N_{k_2}^-(\hat{x}_i) \text{ or } \hat{x}_i \in N_{k_2}^-(\hat{x}_j) \\ 0, & \text{otherwise.} \end{cases}$$

Let

$$L_W = \Sigma^+ - C^+, \Sigma_{ii}^+ = \sum_{j \neq i} C_{ij}^+, \forall i,$$

$$L_B = \Sigma^- - C^-, \Sigma_{ii}^- = \sum_{j \neq i} C_{ij}^-, \forall i,$$

where Σ^+ and Σ^- are diagonal. L_B and L_W are the so-called graph Laplacian matrix for between-class and within-class samples.

In this research, all columns of the dictionary D have maximal unit length is further assumed. Then the set defined as

$$\mathcal{D} := \left\{ \mathbf{D} \in \mathbb{R}^{m \times k} \,\middle|\, \mathrm{rk}(\mathbf{D}) = m, \|\mathbf{d}_i\|_2 \leq 1 \right\}. \tag{4.7}$$

The core idea is to maximize the distances among nearest neighbors from different class and minimize the distances among nearest neighbors from the same class. With this aim, it is expected to extract the low dimensional features that have enough power on discrimination. Mathematically, our goal is to learn a projection $V \in \mathbb{R}^{k \times d}$ to get a low dimensional embedding $Y = V^\top \Phi_X(D)$.

By employing a compact form of the solution of (4.5) using Lasso [Efron et al., 2004], the discriminative features learning problem can be formulated as the following minimization problem,

$$\min_{V,D} \quad f(V, D) := \| \left(V^\top \Phi_X(D) L_W \Phi_X(D)^\top V \right) \|_F^2 - \mu_1 \| \left(V^\top \Phi_X(D) L_B \Phi_X(D)^\top V \right) \|_F^2, \tag{4.8}$$

with the projection matrix $V^\top V = I_m$, $\mu_1, \mu_2 \in \mathbb{R}^+$. Therein $\Phi := [\phi_1, \ldots, \phi_n] \in \mathbb{R}^{k \times n}$ contains the corresponding n sparse transform coefficient vectors.

It is obvious that, when D is given, the optimal V can be computed by solving the following minimization problem

$$\min_V \| \left(V^\top \Phi L_W \Phi^\top V \right) \|_F^2 - \mu_1 \| \left(V^\top \Phi L_B \Phi^\top V \right) \|_F^2. \tag{4.9}$$

Resolving (4.9) is commonly readily computed via solving the generalized eigenvalue decomposition (GED) [Yan & Tang, 2006] method

$$A v_i = \lambda_i B v_i, \ i = 1, 2, \cdots k. \tag{4.10}$$

where $A = \Phi L_B \Phi^\top$, $B = \Phi L_W \Phi^\top$, v_i is the singular vector corresponding to the i-th largest singular value of AB^{-1}.

4.2.2 Linear Classification

When $Y = V^\top \Phi_X(D)$ is learned, the final step for our classification problem is discussed using a linear model

$$Z = W^\top Y, \tag{4.11}$$

where $Z \in \mathbb{R}^{l \times n}$ is the target matrix defined by labels, $W \in \mathbb{R}^{d \times l}$ is the prediction parameters for (4.11).

As shown in Sun et al. [2013], joint learning (D, V, W) is equal to learn them separately. Given D, V, the algorithmic solution to the classification problem (4.11) could be resolved by SVM or a general least square regression minimization

$$\min_W \| Z - W^\top Y \|_F^2 + \mu \| W \|_F^2. \tag{4.12}$$

The joint learning framework (4.11) decouples into two separate components, i.e., learning D and V before multi-label classification using W.

In this research, it is proposed to develop a alternative optimization algorithm to learn the parameters of D, V, W. In the i-th iteration, when the $D^{(i-1)}$ is fixed, the joint learning of $V^{(i)}$ and $W^{(i)}$ is equivalent to computing transformation $V^{(i)}$ at first by (4.10), and then apply classification in the dimensionality-reduced space to learn $W^{(i)}$. With $V^{(i)}$ and $W^{(i)}$ at hand, we then update $D^{(i)}$ via minimizing (4.9). This approach is called as *learning dictionary and projection matrix for linear classification (DPLC)* in the rest of this paper.

4.3 Optimization of DPLC

The minimization procedure of the original DPLC model in Eq. (4.9) is firstly presented, and then a simplified classification model in Eq. (4.11) is addressed. The final classification problem in Eq. (4.12) can be divided into three sub-problems by optimizing D, Φ, V and W alternatively: updating Φ with D, V fixed, updating D with Φ, V fixed, and updating V with Φ, D fixed. Finally, we calculate W via Eq. (4.12). The alternative optimization is iteratively implemented to find the desired dictionary D, projection V, coefficient matrix Φ and classification prediction parameter W.

Update of Φ

Suppose that the dictionary D is fixed, and then the objective function in Eq. (4.8) is reduced to a sparse representation problem to compute $\Phi = [\Phi_1, \cdots, \Phi_c]$ with i^{th} class sparse codes $\Phi_i = [\phi_1, \cdots, \phi_{n_c}]$. In this work, $D = [D_1, \cdots, D_c]$ is acquired, and D_i is the subdictionary for i^{th} class. At first iteration, for each subdictionary D_i, it is learned via K-SVD [Aharon et al., 2006]. Given dictionary D, Φ_i is got via minimizing (4.3).

Update of V and W

With the D and Φ at hand, it could get V via GED of Eq. (4.10). W has the closed expression via minimizing Eq. (4.12).

Update of D

The method to update $D = [D_1, \cdots, D_c]$ when Φ is fixed, is discussed in the following part. Firstly, the Euclidean gradient $\nabla_f(D)$ of f with respect to D is computed. Using some shorthand notation, let Λ_i be the support of nonzero entries of $\phi_D(x_i)$, and denote $K_i := D_{\Lambda_i}^\top D_{\Lambda_i}$, $r_i := D_{\Lambda_i}^\top x_i - \lambda_1 s_{\Lambda_i}$, $u_i = vv^\top \phi_i$ and $q = (L_W - \mu_1 L_B)$. Then, the Euclidean gradient $\nabla_f(P)$ of f is computed as

$$\nabla_f(D) = \sum_{i=1}^{n} 2\mathcal{V}\{y_i u_i q K_i^{-1} + D_{\Lambda_i} K_i^{-1}(q^\top u_i^\top r_i^\top + r_i u_i q)K_i^{-1}\}. \tag{4.13}$$

It is easy to update D using classical iterative gradient method.

Finally, the complete method of learning (D, V) is summarized in Algorithm 1.

1: Training data $X \in \mathbb{R}^{m \times n}$, initial dictionaries $D = D^{(0)}, V = V^{(0)}$, initializing the parameters λ_1, μ_1, μ_2 and μ_3, $i \leftarrow 0$.
2: **repeat**
3:     Using Lasso algorithm [Efron et al., 2004] to update sparse vectors set
    $\Phi_X^{(i+1)} = [\phi_{x_1}(D), \phi_{x_2}(D), \ldots, \phi_{x_n}(D)]$.
4:     Update $V^{(i+1)}$ via resolving Eq.(4.10).
5:     Update $W^{(i+1)}$ via resolving Eq.(4.12).
6:     Using the well-known line search to find step size $t^{(i)}$.
7:     Update $D^{(i+1)} = D^{(i)} + t^{(i)} * \nabla_f(D^{(i+1)})$. If $\|d_j\|_2 > 1$, project d_j on to $\|d_j\|_2 = 1$.
8:     Set $i = i + 1$.
9: **until** $\|(\nabla_f(D^{(i+1)}))\| < \text{thresh} \vee i = \text{maximum iterations}$
10: **return** $D \leftarrow D^{(i+1)}, V \leftarrow V^{(i+1)}, W \leftarrow W^{(i+1)}$.

Algorithmus 1 : Alternative Dictionary Learning for classification.

4.4 Details on Implementation

In this thesis, D_0 is acquired using the general method on dictionary learning for each class respectively, known as K-SVD [Aharon et al., 2006]. In detail, a sub-dictionary is learned for each class using several iterations of K-SVD and then all the sub-dictionaries are combined (i.e., dictionary items learning from each class) as a global dictionary D_0. The label of each dictionary item d_k is then initialized on the basis of the class it corresponding to and will remain fixed during the entire dictionary learning process, although d_k updated during the learning process.

The procedures displayed in Algorithm 1 are the version of gradient descent procedure. The learning rate $t^{(i)}$ can be computed via the well-known line search method, referring to Moré & Thuente [1994]. Here, considering the high coherence among the images or imaginary patches, the dictionary with low redundancy is preferred, that is, $k \leq 3m$ for the dictionary $D \in \mathbb{R}^{m \times k}$. The parameters for μ_1, μ_2 in (4.8) could be well tuned via performing cross validation.

5 Experiments

This Chapter describes the experimental dataset used for assessing the performances of the methodology presented in Chapter 3 and Chapter 4. Firstly, the experimental dataset is introduced in Section 5.1. Then, the fundamental states of investigated areas are described in the next section. At last, more specifically, the flow of the experiment design is presented in Section 5.3.

5.1 Experimental Dataset

5.1.1 TerraSAR-X Images

TerraSAR-X (TSX) is a German Earth observation satellite, built in the context of a public-private partnership between the German Federal Ministry of Education and Research, the German Aerospace Center, and Astrium GmbH. Its launch accomplished on 15th June 2007, and the sensor has a nominal lifetime of 5 years, although it is currently expected to last up to more years. The payload of the satellite is an X-band SAR system with a 9.65 GHz centre frequency, an electronically steerable phased-array antenna and a side-looking imaging capability within an off-nadir pivoting range of approximately 20-55 degrees. The TSX flights in a near-polar dawn/dusk orbit at an altitude of 514 km. With its active radar antenna it possesses abilities to obtain image data with a spatial resolution of 1 m, and regardless of weather conditions or absence of daylight.

In this thesis, six TSX scenes covered two different areas represented discriminative characteristics of glaciers in light of dimensions, surface features, topography etc. acquired in SM are available for experiments. Detailed information of the data used can be seen in Table 5.1. TSX's particularly high spatial resolution and an exact-repeat cycle of 11 days, in combination with its extremely high geolocation accuracy, makes it a popular data sources for glaciers monitoring. Fig. 5.1 gives examples of original TSX SAR intensity images after terrain correction.

Location	Min Incidence Angle	Max Incidence Angle	Acquisition Time	Imaging Mode	Pass Direction	Polarisation Channels	Data Type
	35.81°	38.79°	20090711	SM	ascending	HH	SSC
Taku Glacier	35.80°	38.79°	20090722	SM	ascending	HH	SSC
	26.94°	30.57°	20090802	SM	descending	HH	SSC
	31.67°	34.78°	20090616	SM	ascending	HH	EEC
Baltoro Glacier	29.43°	32.73°	20090627	SM	ascending	HH	EEC
	33.71°	37.14°	20091224	SM	descending	HH	EEC

Table 5.1: TSX data delineation used for experiments. SSC: single look slant range complex; EEC: enhanced ellipsoid corrected; HH: horizontal transmit, horizontal receive; SM: stripmap mode.
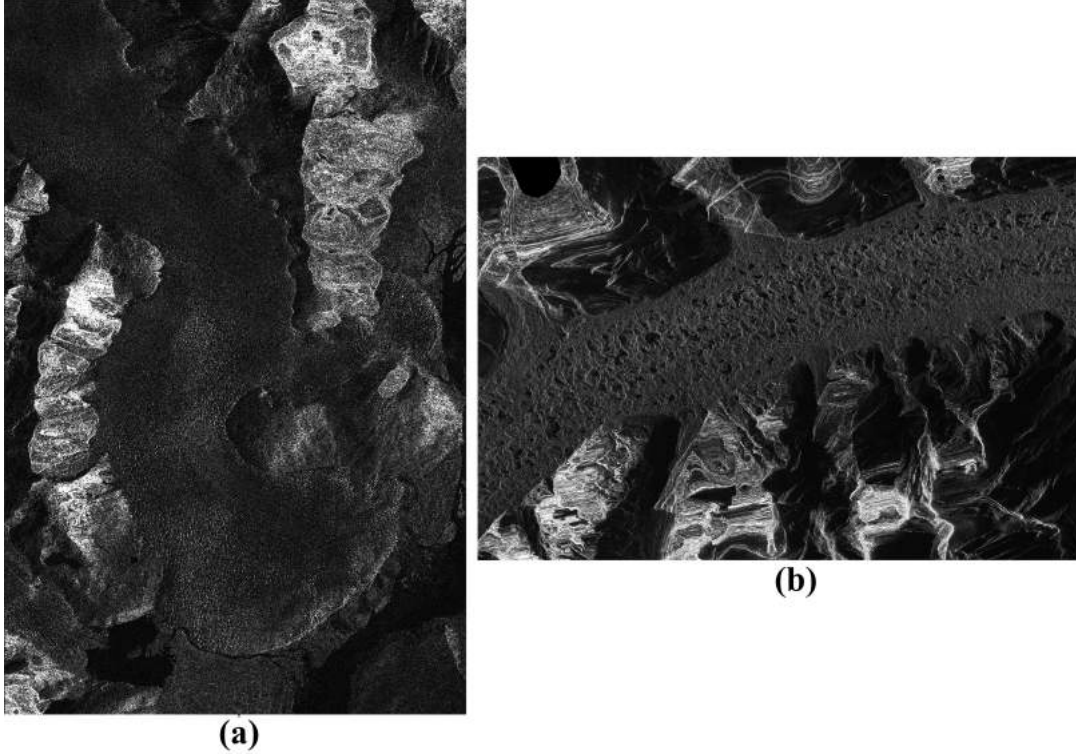
Figure 5.1: Examples of original TSX SAR intensity images after terrain correction. (a) TSX SAR intensity image, area of Taku glacier; (b) TSX SAR intensity image, area of Baltoro glacier.

5.1.2   Simulated SAR Dataset

The objective of experiments using simulated SAR dataset is to evaluate the performance of robust phase correlation algorithm when dealing with the SAR intensity images in the context of speckle, and the performance of proposed ARLee filter is also assessed. The original optical images for simulating SAR image originate from artificial test image (Fig. 5.2a), ASTER Band3N image of Antarctic region (Fig. 5.2b) and THEOS panchromatic image of urban areas (Fig. 5.2c). The way of generating synthetic SAR image is similar to the method used in Schmitt & Stilla [2014], in which the multiplicative noises with a Rayleigh distribution are added to the intensity information. The images shown in Fig. 5.2d is designed to prove the performance of the proposed ARLee filter. While the images shown in Fig. 5.2e and f are designed to assess the property of robust PC algorithm, respectively.

In detail, the original shifted optical image pairs were generated from a downsampled high-resolution image with known sub-pixel shifts, according to Eq. 5.1 in Tong et al. [2015].

$$I_{low}^{optical} = D(I_{high}^{optical}, M) \tag{5.1}$$

where $I_{high}^{optical}$ and $I_{low}^{optical}$ refer to the high-resolution imagery with integer shifts and the low-resolution imagery with same sub-pixel shifts, respectively, and D indicates the downsampling process with the factor M in each dimension. For instance, the integer shift Δx in the high-resolution imagery will be downsampled as a sub-pixel shift $\frac{\Delta x}{M}$ in a low-resolution imagery. The M used in this work is equal to 4. For each image, the subset image was translated by subpixel displacements ranging from 0.25 to 5 pixels by a step of 0.25 pixels in the x-direction, and a fixed displacement of 0.5 pixels in the y-direction to achieve 20 synthetic image pairs (i.e., the original
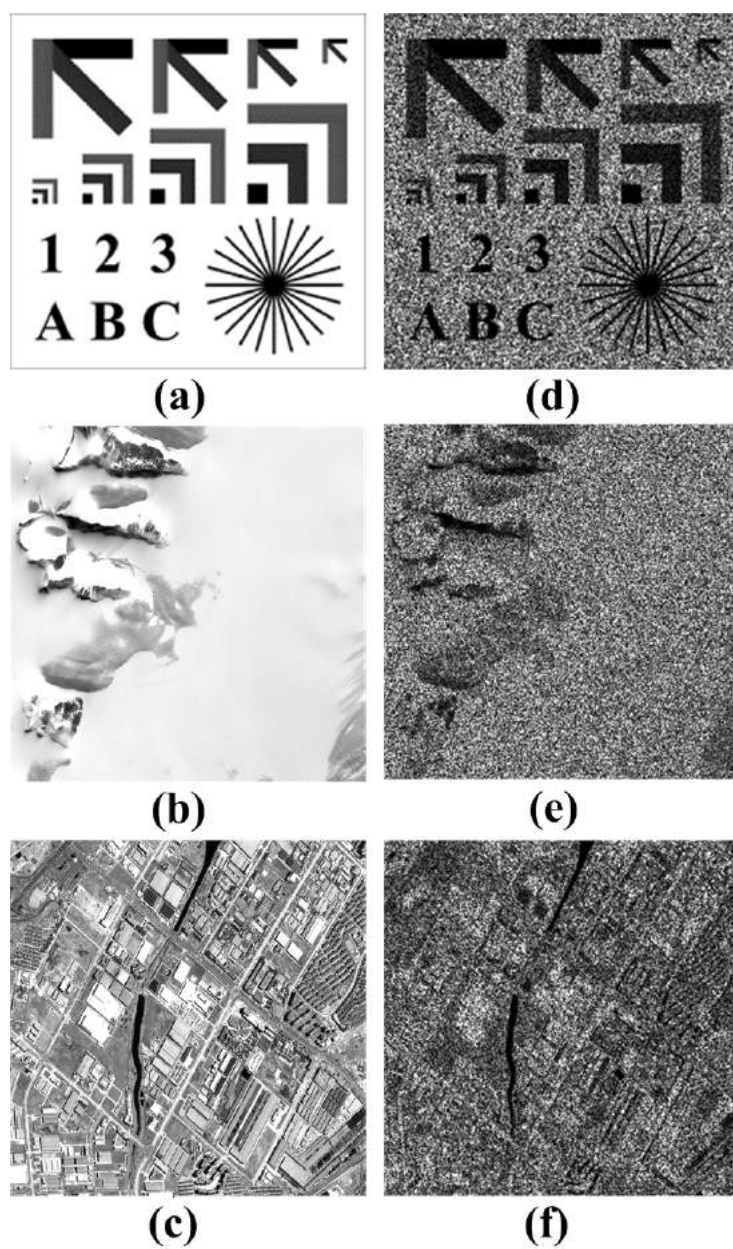
Figure 5.2: Examples of simulated SAR intensity images. (a)-(c) original images; (d) simulated SAR intensity image used for testing performances of filters; (e) and (f) simulated SAR intensity images used for assessing properties of matching methods.

image and the shifted image). Basis on the synthetic optical shifted imagery, the simulated SAR images is generated following Eq. 5.2.

$$I^{SAR} = S(I_{low}^{optical}, \sigma_{sar}, \mu_{sar}) \tag{5.2}$$

where I^{SAR} stands for the simulated SAR imagery and S denotes the simulation process with the noise variance σ_{sar} and noise mean value μ_{sar} . Since the noises of amplitude and phase are independent sharing the same noise variance, their corresponding noise of intensity value will follow Rayleigh distribution. In this case, the noise mean value μ_{sar} is 1 and the noise variance σ_{sar} is ranging from 0.1 to 1.

To evaluate the performance of proposed ARLee filter, the speckle suppression and mean preservation index (SMPI) and edge preservation index (EPI) proposed in Schmitt & Stilla [2014] and Lang et al. [2014] are referred to give a reliable assessment. The SMPI is calculated by:

$$SMPI = (1 + |\mu_o - \mu_f|) \cdot \frac{\sigma_f}{\sigma_o} \tag{5.3}$$

where μ_o , μ_o , σ_o and σ_f stand for means and standard deviations of the original optical (intensity) image and the filtered SAR image, respectively. More sophisticated EPI is given by the following:

$$EPI = \frac{(|p_f(i,j) - p_f(i+1,j)| + |p_f(i,j) - p_f(i,j+1)|)}{(|p_o(i,j) - p_o(i+1,j)| + |p_o(i,j) - p_o(i,j+1)|)} \tag{5.4}$$

where p_o , p_f , i and j donate pixel values in the original optical (intensity) image and the filtered SAR image and image coordinates, respectively. The lower the SMPI values are, the more efficient the filter performs, while the higher the EPI values are, the more details the filter can preserve.

Towards the evaluation for matching performance of robust PC, similar to that in Tong et al. [2015], the mean value, root mean square error (RMSE) and standard deviation are adopted to assess the accuracy and robustness of the proposed PC algorithm. In this simulated matching test, five representative matching algorithms, including (i) NCC [Lewis, 1995], (ii) Foroosh's PC based on interpolation [Foroosh et al., 2002], (iii) Nagashima's PC based on peak elevation fitting [Nagashima et al., 2009], (iv) Hoge's PC based on SVD [Hoge, 2003], (v) Leprince's PC based on non-linear optimization [Leprince et al., 2007], in spatial and phase domain are employed as comparisons.

5.2   Investigated Areas

5.2.1   Taku Glacier in Juneau Icefield

The first study area used in this thesis is located in Juneau icefield in the coast mountains of southeast Alaska, U.S.A, within the scope of which several glaciers are included and can be observed. Their distributions can be seen in Fig. 5.3, and the Taku glacier among them is our projected investigating object. The Taku Glacier is a tidewater glacier belonging to a low-latitude glacier system of small scale which is recognized as the deepest and thickest glacier known in the world, with its thickness and length measured at 1477 m and approximately 58 kilometres, respectively [Pelto, 2011]. As the only advancing glacier among the 20 major glaciers of the Juneau Icefield, monitoring the behavior of Taku glacier is of great value since it can reflect the tendency of glacier changing in south Alaska district. In Fig.5.4a, the coverage area of the TSX image scenes used is illustrated, while the shuttle radar topography mission- X band (STRM-X band) DEM for the terrain correction is given in Fig. 5.4b.
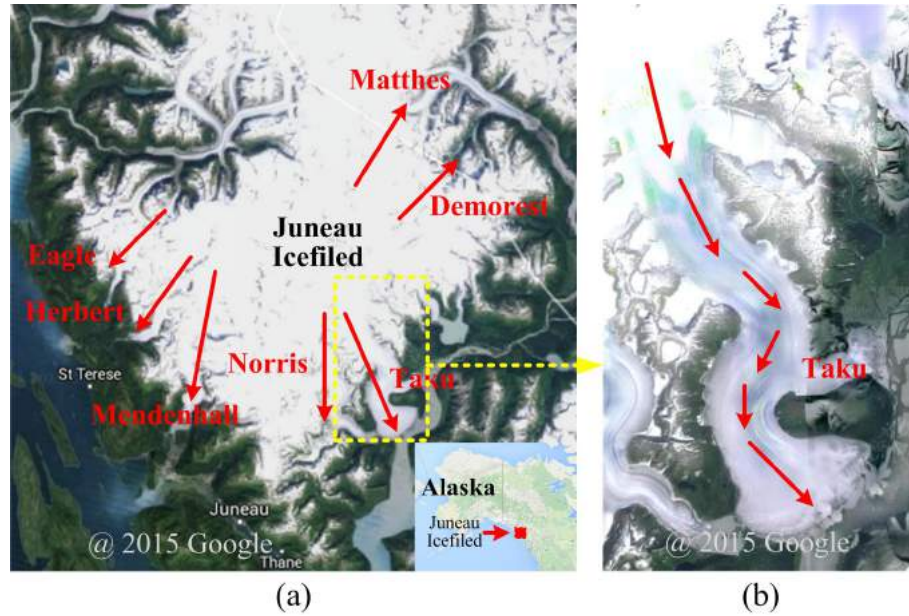
Figure 5.3: Taku Glacier in Juneau Icefield. (a) Distribution of glaciers in Juneau Icefiled. (b) Illustration of Taku glacier.
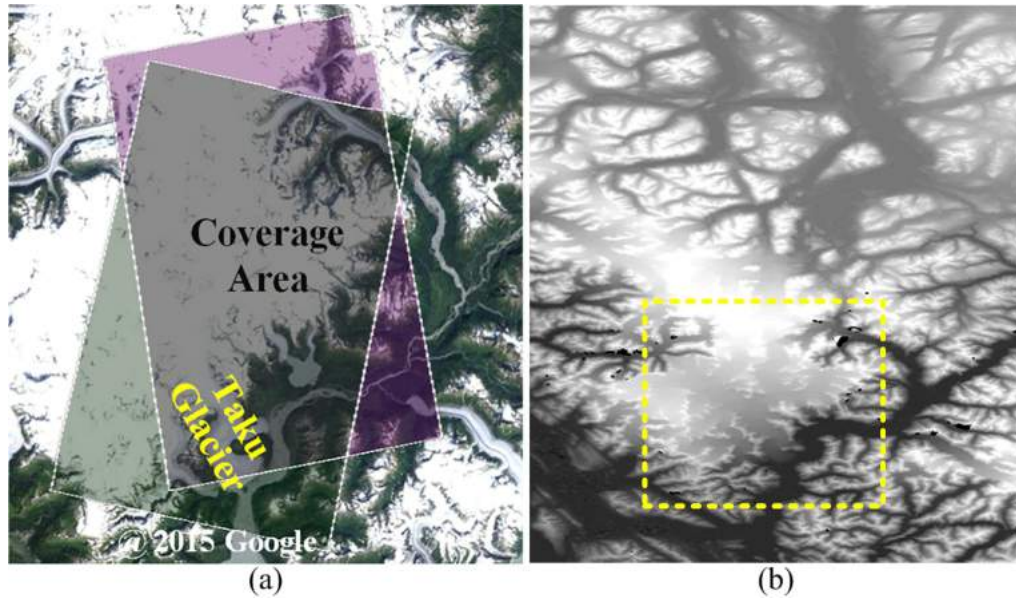

Figure 5.4: The coverage area of the data used in Taku glacier. (a) TSX scenes coverage area in Juneau Icefield. (b) STRM-X Band DEM used for terrain correction and brighter grey value means higher elevation; Yellow box: coverage area of image (a).
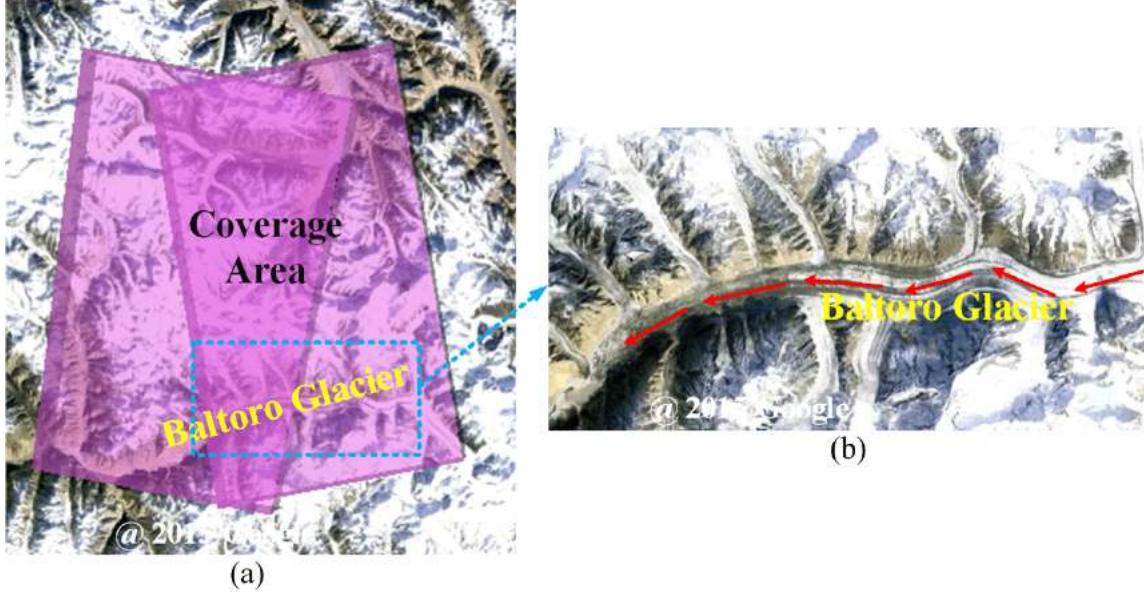
Figure 5.5: The coverage area of the data used in Baltoro glacier. (a) TSX scenes coverage area in Karakorum mountain range. (b) Illustration of Baltoro glacier.

5.2.2   Baltoro Glacier in Himalyas

Aiming to validate the feasibility and robustness of our proposed methods, another case area, named Baltoro glacier located in Karakorum mountain range in Northern Pakistan, descending to east from the K2 (8611 m a.s.l.) and terminating at an elevation of 3500 m with a length of about 63km, which can represent discriminative characteristics of glaciers in light of dimensions, surface features, topography etc. is introduced to our experiments. Different with the Taku glacier featuring by the large covering area and a wide variety of ground objects, the Baltoro glacier is characterized by thick debris cover in its lower part and high relief topography. In Fig. 5.5, the coverage area of the TSX image scene used and the case area are illustrated.

5.3   Experiment Design

Since this thesis is trying to focus on glacier monitoring via two important aspects, i.e. glacier surface velocity, and areas of glacier facies, the experiments are divided into two main categories separately as follows.

- **Glacier surface motion estimation:** the methodology described in Chapter 3 is tested and evaluated firstly on the simulated SAR dataset. Next, the method is applied in the Taku glacier and the Baltoro glacier using 2 pairs of sequential TSX images in summer time (see Table 5.1) with 11 days as the interval period, aiming to test the potentials of the method in glaciers with different characteristics (e.g., gentle and high-relief topography, clean and debris covered ice, fast and slow movements).

- **Glacier surface classification:** the methodology illustrated in Chapter 4 is tested on two glaciers represented discriminative characteristics in light of dimensions, surface features, topography etc., in order to evaluate the feasibility of the proposed method. Firstly, the method is applied in the Taku glacier using a single-polarization TSX imagery acquired in summer time (ablation season) to mainly test the abilities of the method on discriminating wet snow and ice. Then, the method is test on the Baltoro glacier with a single-polarization

TSX imagery acquired in winter time (accumulation season) in light of potentials of the proposed method on discriminating dry snow and ice. Additionally, the superiority of proposed approach is demonstrated and endorsed by comparing with other classical techniques.

6 Results

In this chapter, the experimental results using dataset described in Chapter 5 are presented aiming to evaluate the methods and algorithms proposed in this thesis. In the context of glacier monitoring tasks in this thesis, two important parameters which are most indeed to be obtained using spaceborne SAR intensity images, namely the glacier surface velocity and the areas of glacier facies, are analyzed. Two different datasets covering areas located in two types of glaciers representing discriminative characteristics in light of dimensions, surface features, topography etc. are selected to undergo the experiments in order to validate the feasibility and robustness of our proposed methods. The results are structured as the results on glacier surface motion (Section 6.1), and the results on glacier surface classification (Section 6.2).

6.1 Glacier Surface Motion

In these experiments, both the simulated SAR and real SAR intensity image data were used to assess the performance of proposed methods and to measure the real glacier motion respectively. In simulated cases, synthetic SAR intensity images are generated from original optical images with additional noise added. In real application case, the real TSX intensity image pairs covering Taku glacier and Baltoro glacier are employed, separately, aiming to measuring the 2D motion of glacier surface within a time period of 11 days.

In the former work [Maksymiuk et al., 2016], the glacier velocity of Taku glacier once estimated by the use of intensity tracking using NCC corrected by a physically-based regularization. However, in this work, the intensity tracking is operated via PLF and robust PC algorithm, in order to achieve more detailed motion information in Taku glacier and Baltoro glacier. This approach is independent from exploiting a physical model as long as the fundamental topographic information (e.g., DEM) is obtained.

6.1.1 Validation of Algorithm using Simulated SAR Dataset

Image Filtering

In Fig. 6.1, the filtering results using different filters are exemplified. Besides the proposed ARLee filter, Boxcar filter, local sigma filter, Lee filter, enhanced Lee filter and non-local mean filter are employed as comparisons. The simulated SAR intensity image is generated with a noise variance of 0.3 and noise mean of 1. The filtering window size of filters used is 7×7 (for the ARLee filter, it is the minimum window size). SMPI and EPI, aforementioned evaluation criterions for the performance of filters, is calculated and shown in Table 6.1.

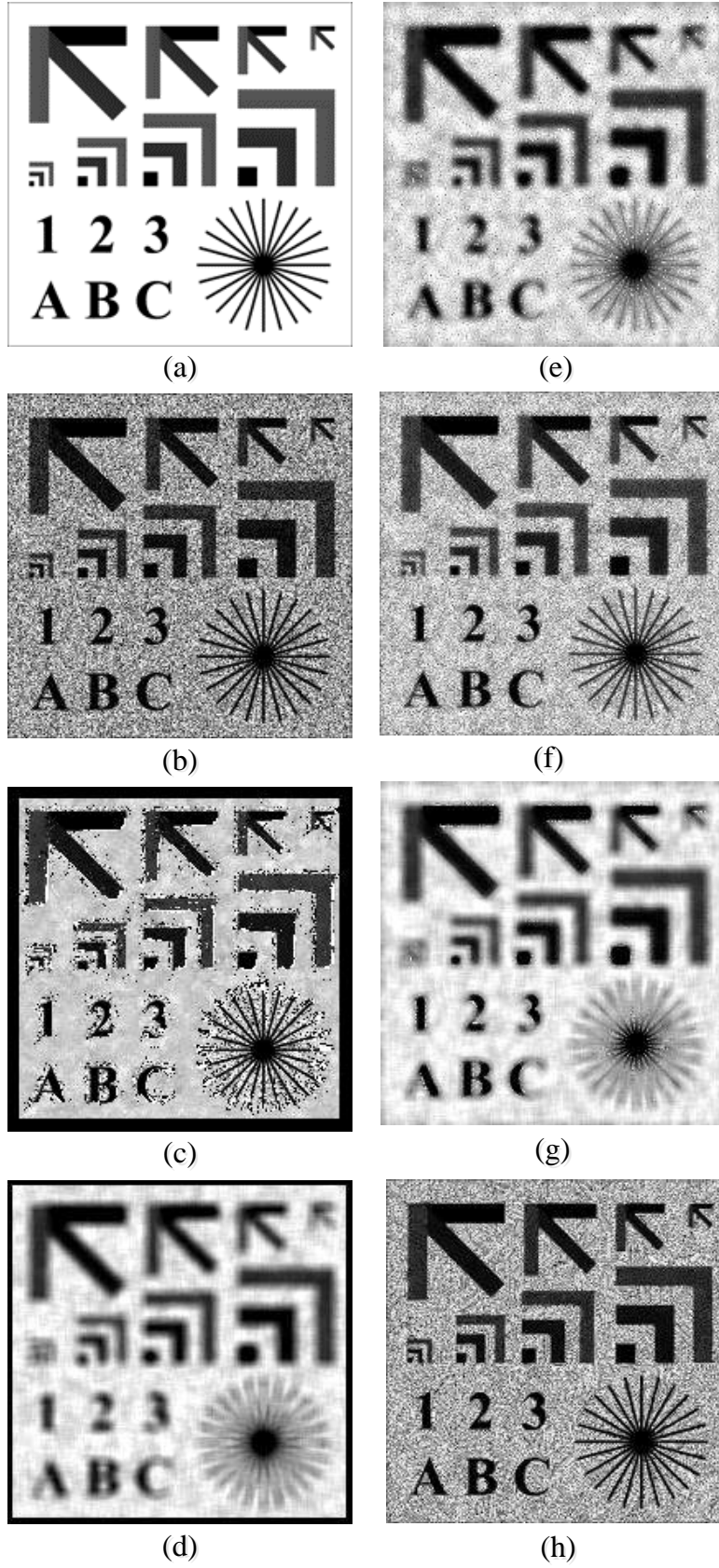(a)

(e)

(b)

(f)

(c)

(g)

(d)

(h)

Figure 6.1: The filtering results by different filters. (a) Original optical image, (b) Simulated SAR image, (c) filtering result by ARLee filter, (d) filtering result by Boxcar filter, (e) filtering result by Local sigma filter, (f) filtering result by Lee filter, (g) filtering result by Enhanced Lee filter, (h) filtering result by Non-local mean filter.

Index	ARLee	Boxcar	Local Sigma	Lee	Enhanced Lee	Non-local mean
SMPI	32.4945	15.4319	23.3742	32.6774	16.0836	49.7571
EPI	2.5053	0.6524	1.1861	2.0380	0.7577	2.3722

Table 6.1: Comparison of filtering performance. SMPI: the larger value means better filtering performance; EPI: the smaller value means better filtering performance.

Robust PC Matching

The corresponding results of the different phase correlation methods in terms of mean value, RMSE and standard deviation are shown in Fig. 6.2, respectively, with the various matching algorithm compared and noise variance level increased.

6.1.2 Application using TSX Images

Dataset in the Taku Glacier

- **Image Filtering:** An example of filtering results of real TSX intensity image using the proposed ARLee filter is given in Fig. 6.3, and two areas in the scene are zoomed for detailed observation.

- **Topographic Information Relief:** The result of topographic relief is exhibited in Fig. 6.4. As seen from Fig. 6.4, it is clear that by using the Range-Doppler terrain correction, the geometric distortions resulting from topography have been rectified.

- **Point Like Feature Selection:** The scale factor of 2D sinc-function have a decisive impact on the selection of PLFs since only the 2D sinc-function template with an appropriate scale can result in a better correlation coefficient in the convolution process. In Fig. 6.5b, namely the distribution histogram aggregated from the intensity values of Fig. 6.5a, different shapes of 2D sinc-function with various scale factors (1 and 2.5, respectively) and the same template sizes (16×16 pixels) can be observed. Attaining to obtain the optimal scale factor, an adaptive scale estimating procedure is used via the statistical frequency. For each pixel in the matching image patch, a set of 2D sinc-function template with incremental scale factors is applied to the correlation. The scale factor resulting in a highest correlation coefficient will identified as the optimal scale factor. All the optimal scale factors for every pixel in the whole image area will be calculated and accumulated into a histogram of occurrence frequency. The scale factor with highest frequency of occurrence will be selected as the optimal scale factor for the whole image. Examples showing this histogram of frequency for selecting the scale factors can be seen in Fig. 6.5c and d. In this example, the scale factors range from 0.01 to 5.0, it is apparently that the scale factor of around 0.73 getting the highest frequency, so that as for the image patch in Fig. 18a, the scale factor of 2D sinc-function template used is set as 0.73. This scale factor of 2D sinc-function template will be further used for the selection of PLFs in the whole study area. Additionally, in Fig. 6.6b, the result of selection of PLF using the optimal 2D sinc-function template is illustrated.

- **Dense Matching via Robust PC:** After the selection of PLFs, the dense matching process between the image pair is conducted to obtain the 2D displacements of the glacier surface. In this process, the matching grid is designed with an interval of 4 pixels, which means that the matching point will be chosen every four pixels in the image of PLFs. In addition, the correlation coefficients and signal to noise ratio (SNR) are brought in as the evaluation criterions of the matching performance for every matching point. In Fig. 6.7, results of
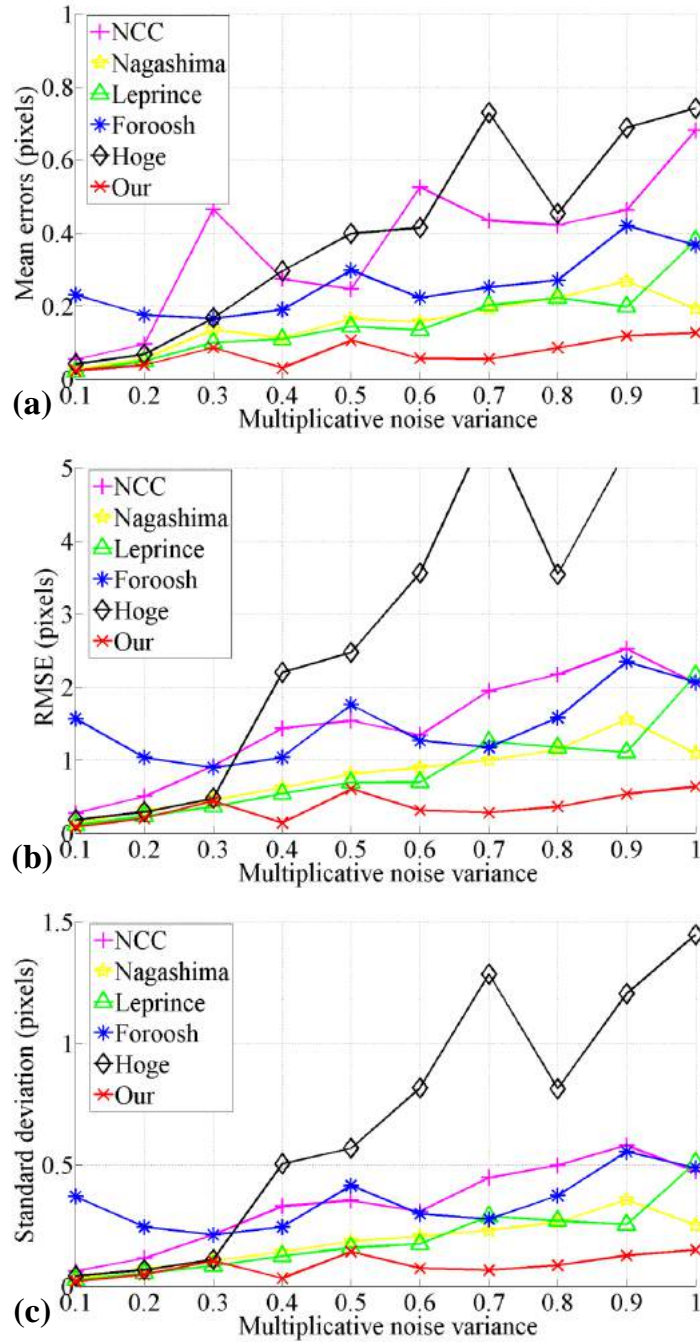
Figure 6.2: The corresponding results of the different PC methods. (a) Mean value, (b) RMSE, (c) standard deviation of the absolute error for the different matching methods with various noise variance.
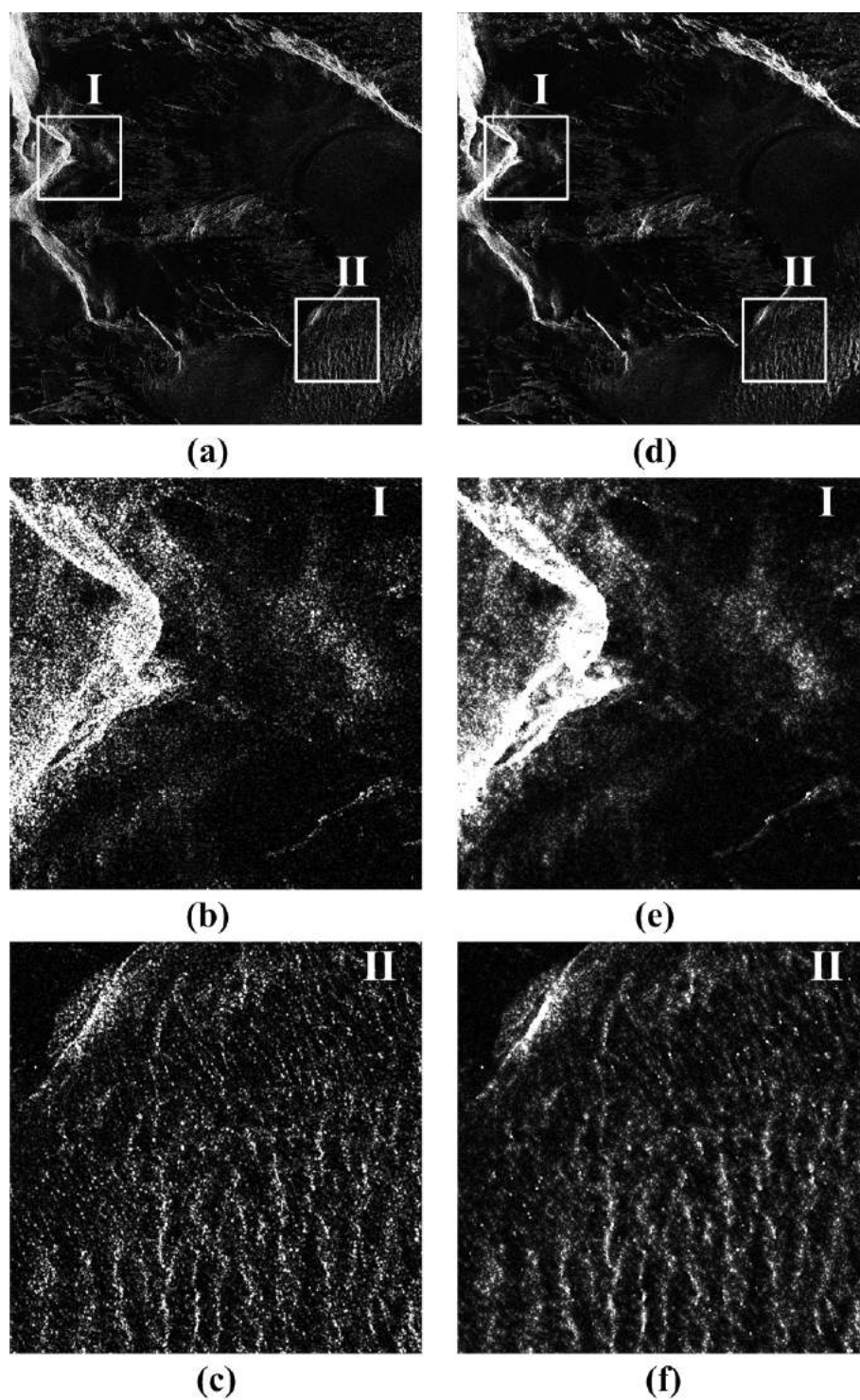
Figure 6.3: An example of filtering results of real TSX data using the ARLee filter. (a)-(c) The original TSX intensity image patches. (d)-(f) The filtered TSX intensity image patch.
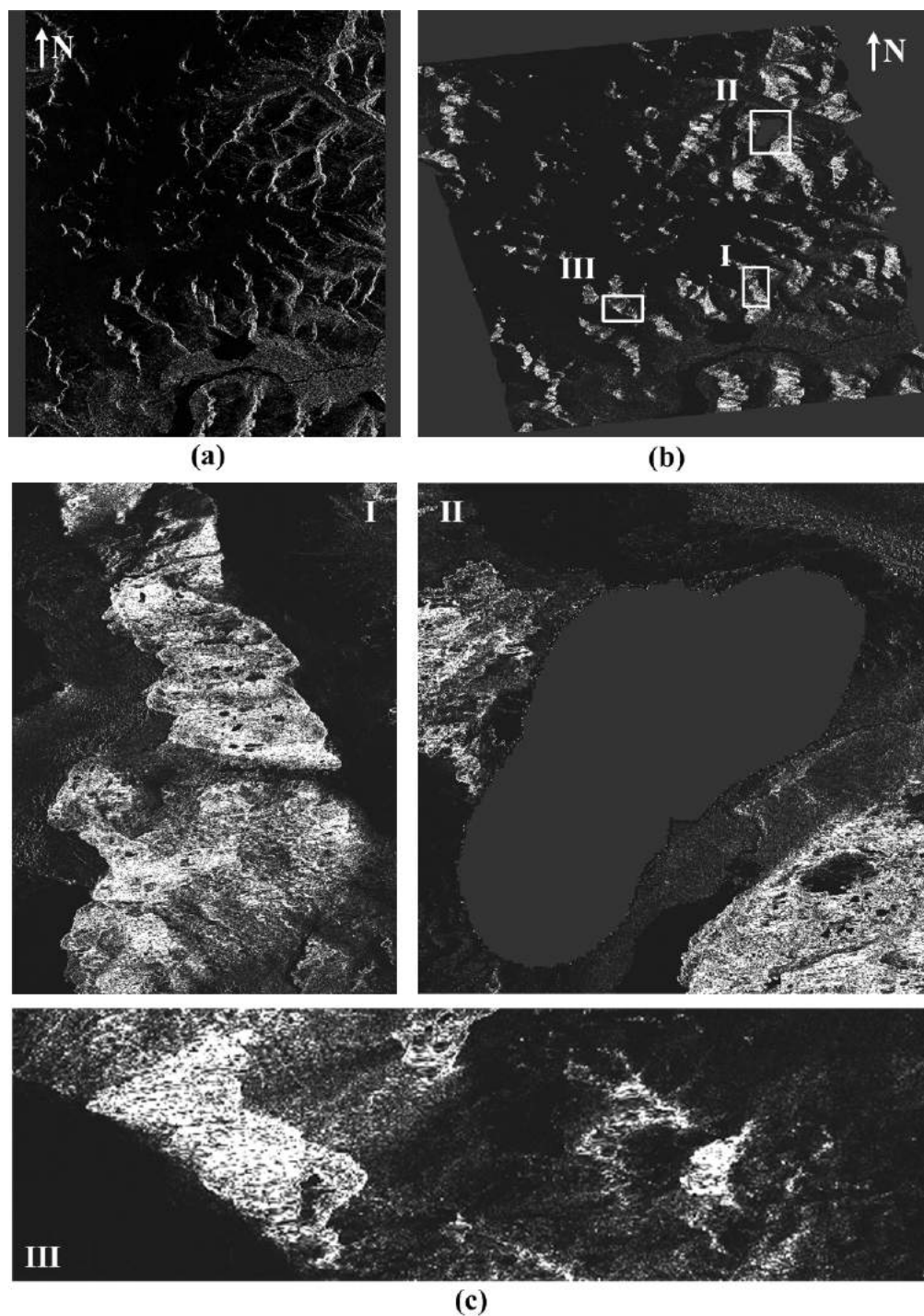
Figure 6.4: The result of topographic relief. (a) Original and (b) orthorectified SAR intensity images of the same scene. (c) Examples of wrongly corrected areas, zoomed in from boxes in (b).
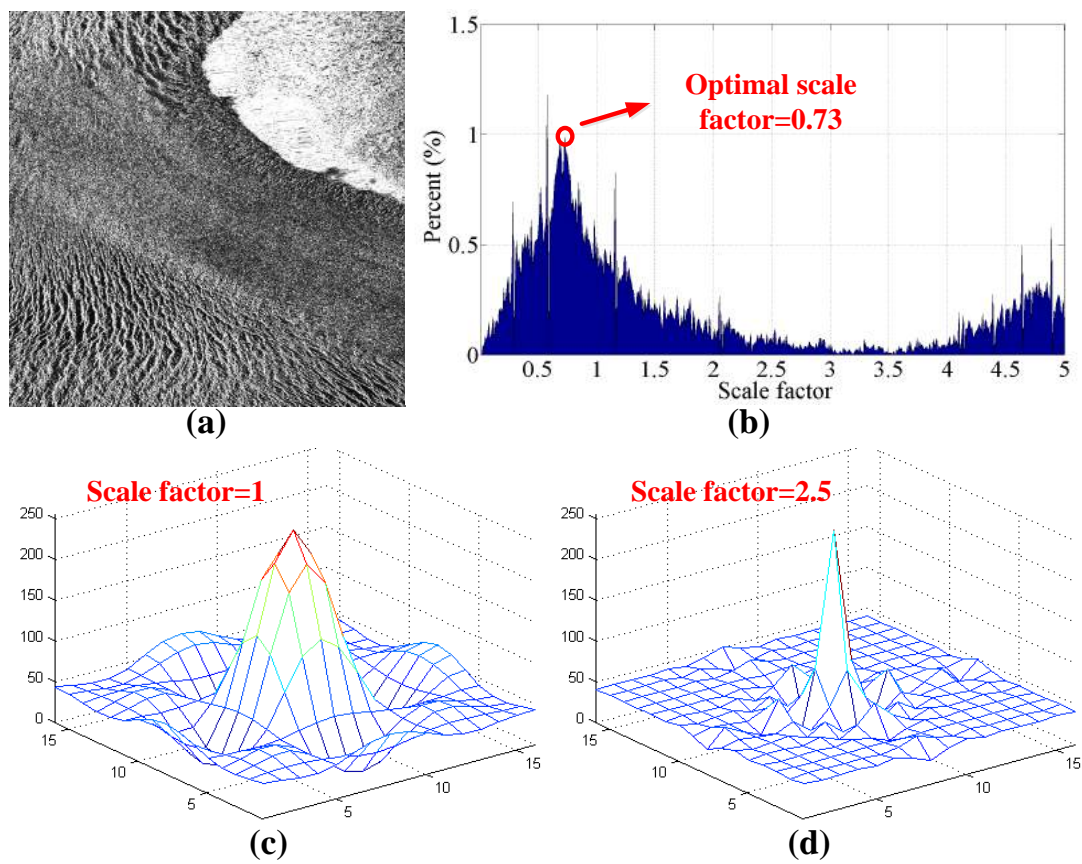
Figure 6.5: Selection of the scale factor of 2D sinc-function. (a) SAR intensity image patch. (b) The 2D sinc-function templates with various scalers. (c) and (d) Corresponding statistical histogram of the optimal scale factor of 2D sinc-function.

Figure 6.6: Results of selection of PLF using the optimal 2D sinc-function template. (a) SAR intensity image patch. (b)Selection result of point like features using optimized 2D Sinc function. (c) Zoom in view of the right rectangle shown in (b).
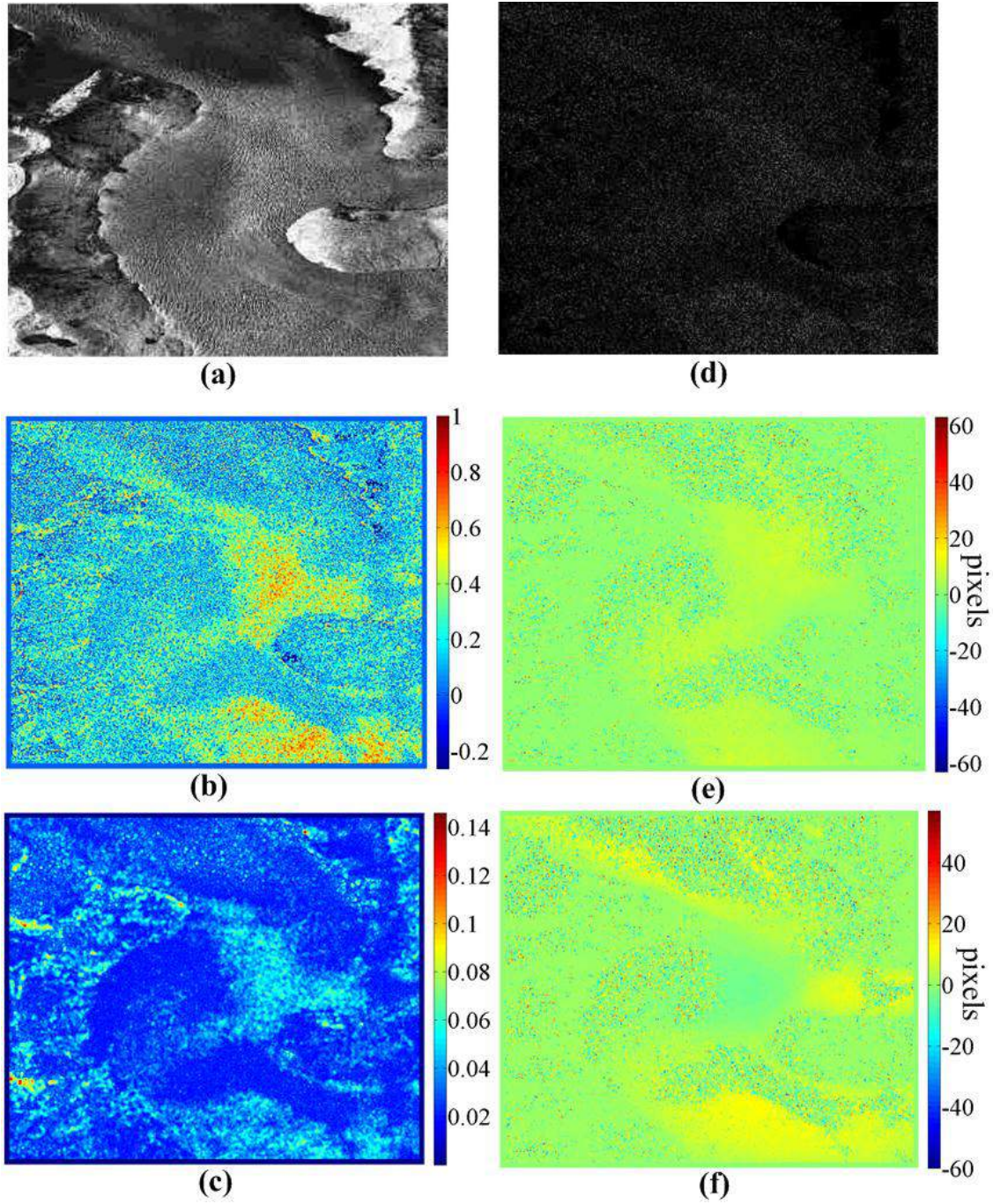
Figure 6.7: Results of the dense matching in Taku glacier. (a) SAR intensity image, area of Taku glacier. (b) Map of correlation coefficients. (c) Map of SNR. (d) Image of selected point like features. (e) Disparity map in x-direction. (f) Disparity map in y-direction.

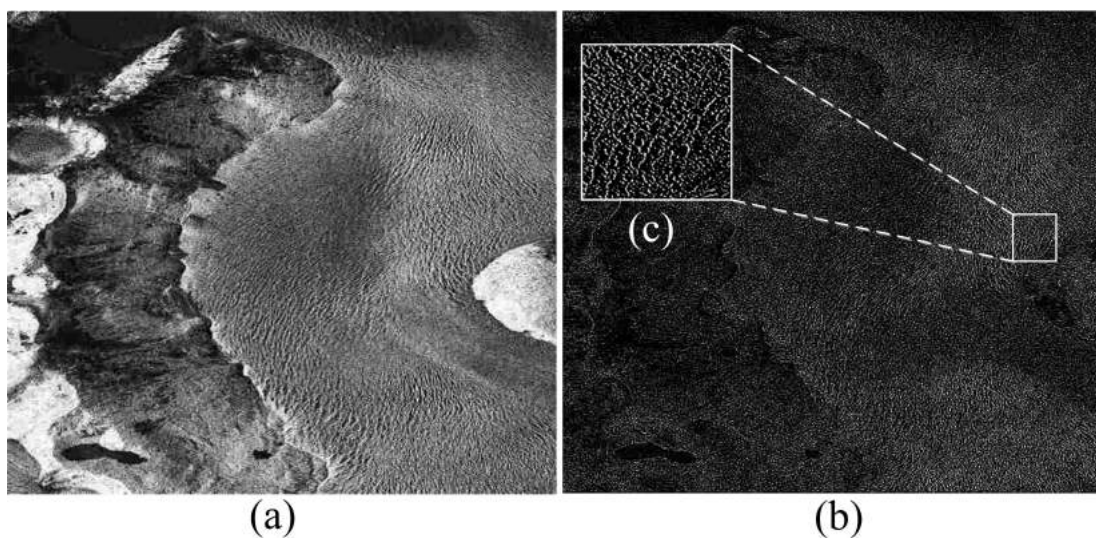dense matching, including the disparity maps in x- and y- directions and correlation map and SNR map recording correlation coefficients and SNR value, are displayed, respectively.

- **Estimated Glacier Surface Motion:** It can be seen from the figures that the main trends of the 2D motion for the glacier during the revisit period of 11 days are obtained with precise values provided. As seen from Figs. 6.7e and 6.7f, the motion of glacier surface in x- direction (west-east) can reach approximately 20 pixels equating to about 42 m on

the ground when considering the ground resolution of 2.09 m for the orhtorectified image. The glacier motion in y-direction (north-south) can also be as large as around 20 pixels. Moreover, the motion trend of glacier in x- direction is relatively consistent, moving from the west to the east with the movement magnitude growing. Whereas the tendencies of glacier motion in y- direction have some variations. In detail, in the upper (north) and lower (south) part of the study area, the glacier surface is moving towards south, but in the middle part (namely the bend of glacier), the moving direction of glacier surface is inversed, with the glacier surface tending to move north.

To make a detailed investigation of the motion of glacier surface in a relative small scale, two profiles of the disparity maps are selected which are set out in Fig. 6.8. One of profiles is located at the intersection of the glacier's main body and its branch, while the other one is placed at the outlet of glacier. The ground lengths of the two profiles are around 960 meters and 1300 m, respectively. The former one aims at analyzing the small changes of movement in the areas with various moving tendency, whereas the latter one is designed to figure out the small changes of movement in the areas with largest global motion. As seen from Fig. 6.8b, the plot of displacement in x- direction for profile 1 shows a stable tendency with values fluctuating between 11 m and 13 m, but for its plot of displacement in y-direction, the movement presents a decreasing trend with the value dropped from 9 m to nearly 0 m. In contrast, for the plots of profile 2, the values movements in both x- and y- directions display a stabilized trend reaching approximately 15 m and 20 m, respectively, but experience more frequent fluctuations than that of profile 1.
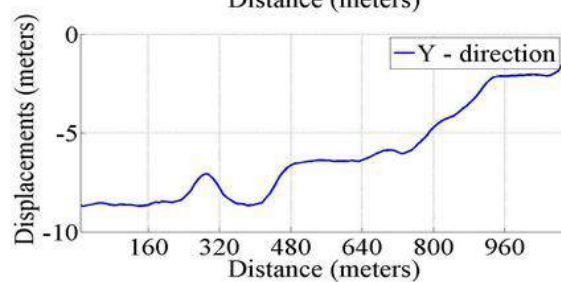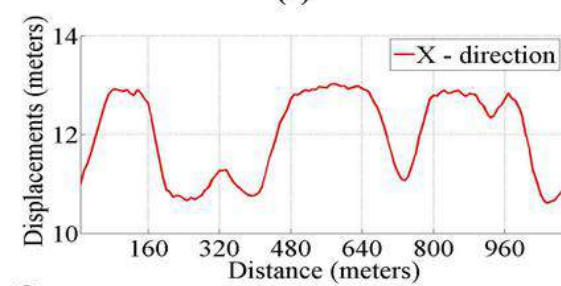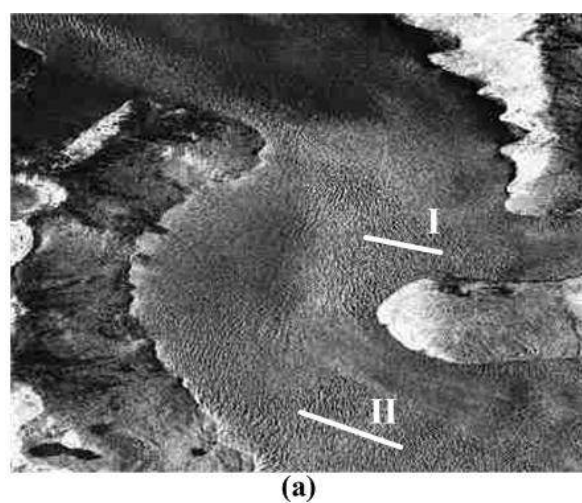
For the sake of a more direct view of glacier motion, two 2D motion fields are selected and drawn through the medium of colorful arrows in Fig. 6.9, in which the direction of arrows indicate the moving direction of glacier ice in the local area and colors represent magnitudes of movements in the moving direction. Similar to the profiles, two motion fileds are given in the glacier areas with complex and largest movements, respectively.

In Fig. 6.10, the elevation changes of the glacier are estimated from the 2D motion value following the aforementioned approaches. Compared with the values of 2D movements, the values of elevation changes are much smaller, with absolute values ranging from 0 to around maximum 0.7 m.

A 3D velocity field of the region in relation to the turning bend of the glacier is given in Fig. 6.11. In this 3D velocity field, the direction of arrow denotes the moving direction of ice, while the color represents the value of velocity in the 2D horizontal plane and the length of arrow shows the value of vertical elevation change.

Dataset in the Baltoro Glacier

- **Dense Matching via Robust PC:** After the selection of PLFs, the dense matching process between the PLFs image pair is carried out to measure the 2D displacements of the glacier surface. To reduce the computation cost, the interval of the matching grid is chosen as 4 pixels, which means that the matching point will be chosen every four pixels in the image of PLFs. In addition, the correlation coefficients and SNR are brought in as the evaluation criterions of the matching performance for every matching point. To refine the dense matching outcome, the same median filter and cutoff thresholds based on statistical histogram are used to the disparity maps to eliminate the gross matching errors. In a similar way to the work of Taku glacier, the cutoff thresholds are identified by the histogram of displacements values from the disparity maps. In Fig. 6.12, the refined results of dense matching, including the disparity maps in x- and y- directions and correlation map and SNR map recording correlation coefficients and SNR, are illustrated.
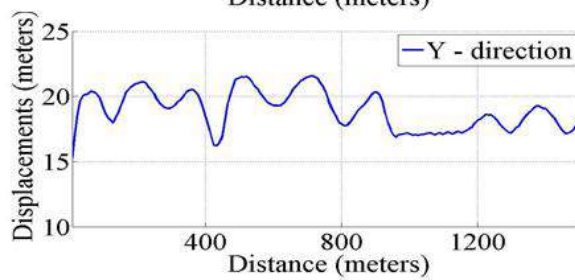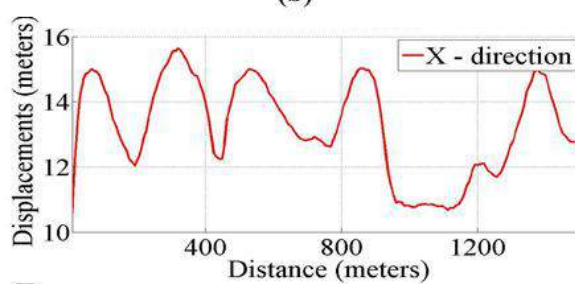
Figure 6.8: Profiles of the 2D motion map. (a) area of profiles. (b) profile I. (c) profile II

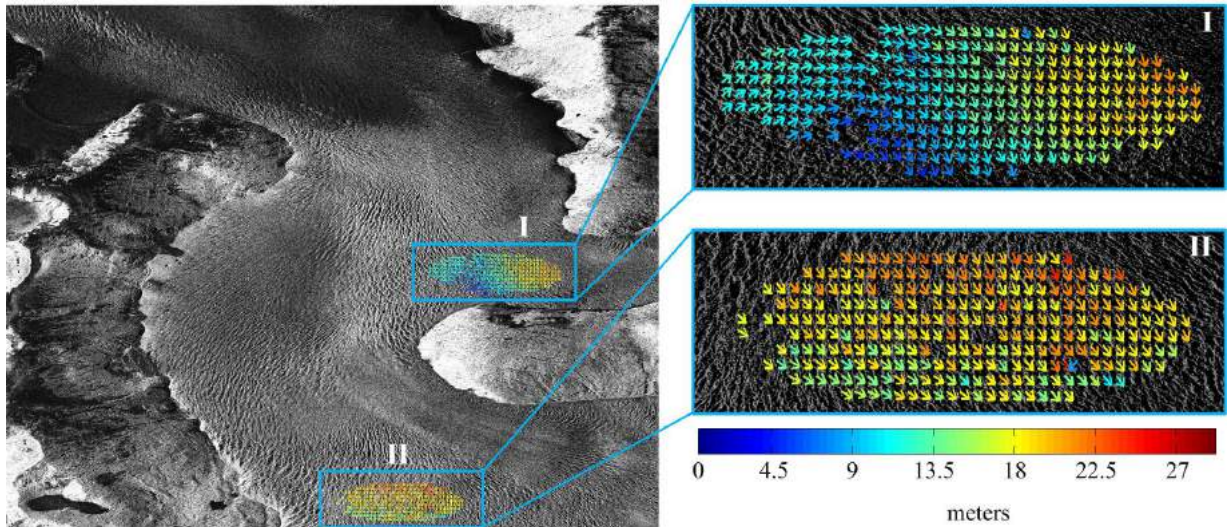Figure 6.9: 2D motion field of the glacier surface in the selected image patches.

- **Estimated Glacier Surface Motion:** On account for a direct view of the glacier motion, two 2D motion fields are selected and drawn through the colorful arrows in Fig. 6.13, in which the direction of arrows indicates the moving direction of glacier ice in the local area and colors represent magnitudes of movements in the moving direction.

6.2 Glacier Surface Classification

The method for multi-classes classification, as described in Chapter 4, on and around the glacier using single-polarimetric SAR intensity images is applied on different datasets located in two areas representing the discriminative characteristics of glaciers. The results are separately presented in Section 6.2.1 and 6.2.2.

6.2.1 Dataset in the Taku Glacier

Fig. 6.14 gives an overview of the Taku glacier and acts as a reference image, which acquired in almost the same period as the TSX data obtained on August 02, 2009 from descending obit, as described in Table 5.1, used in this multi-class classification task.

In the preprocessing step, the reduction of speckles and the correction of topographical distortions of TSX intensity image are carried out. The former one is implemented through the ARLee filter illustrated in Section 3.1.1, while the later one is achieved by means of range-doppler terrain correction described in Section 3.1.2, with aforementioned external STRM data employed.

The Taku glacier is a temperate, maritime valley glacier and one of a small bunch of glaciers experiencing mass gain and terminus advance [Motyka & Beget, 1996]. After most of the yearly precipitation falls in the form of snow, the ablation season in the sample area spans from June to September every year. According to the National Land Cover Database of the United States (http://www.mrlc.gov/viewerjs/) and former researches [Benson, 1962; Pelto, 2011], the land cover map over this typical temperate alpine glacier can be classified into five classes: (i) wet snow, (ii) ice, (iii) water, (iv) natural corner reflector and (v) others comprised by barren land (rock/sand/clay) and vegetated area including forest area, grass land and wetland. Additionally, relief ground and steep edge of the glacier facing the SAR sensor appear as patches with high brightness in the intensity images due to the corner reflector effect in this paper. This special
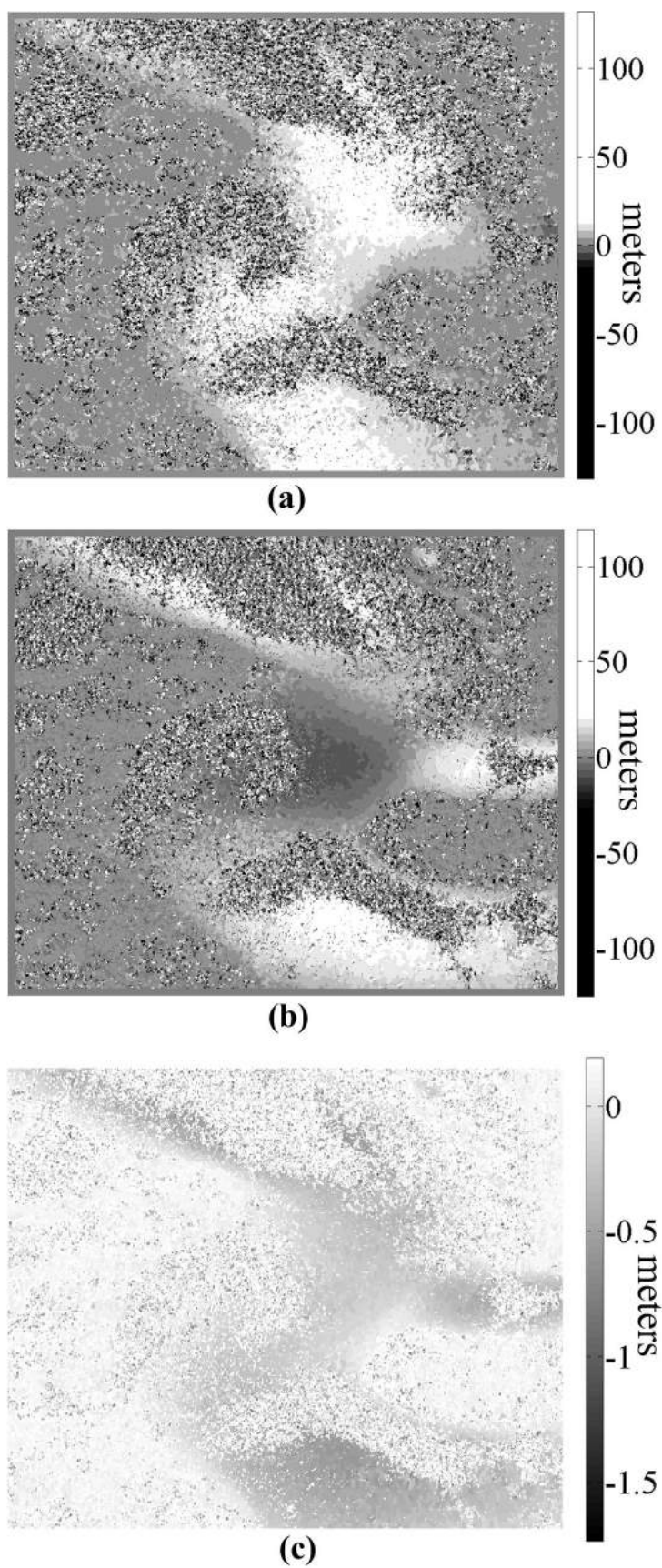
Figure 6.10: 3D motion map of Taku glacier with the gray values showing the horizontal and the vertical displacement. (a) and (b) horizontal motion in x and y directions. (c) vertical motion in z direction.
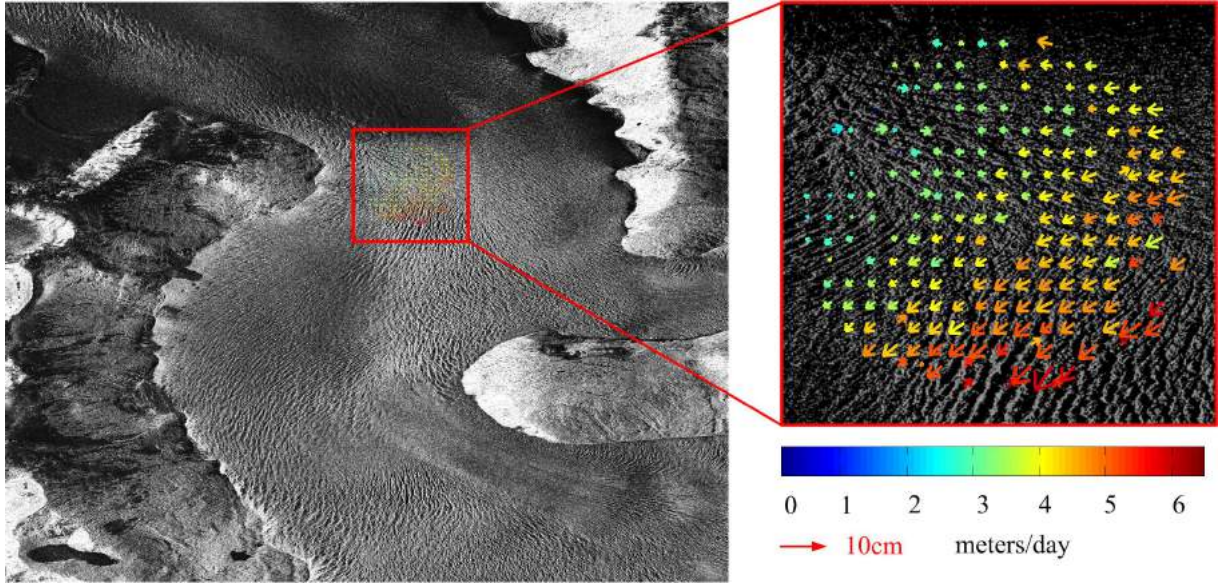
Figure 6.11: 3D velocity field of the glacier surface in the selected image patch.

type called as natural corner reflector (NCR) is not a kind of land cover object but rather a natural structure. In order to avoid mis-classification of the other land covers, the NCR is listed separately.

In the following numerical experiments for multi-class classification, several areas from the above mentioned five kinds of classes in the SAR data are first randomly selected, see Fig. 6.15. Afterwards, the scale of each patch is chosen as 31×31, which has been verified by our numerical experiments that it has enough power to demonstrate the discriminative information of the target pixel. In a similar way, more than 30000 target pixels from these areas are randomly chose, with its locations obtained, and then more than 30000 patches to represent the target pixel in its centre are extracted, with a patch size of 31×31 pixels. In all experiments, each patch is reshaped as a vector with size of 961.

- **Sparse Information:** Fig. 6.16 depicts several raw SAR patches and their sparse coefficients. The dictionary is in $\mathbb{R}^{961 \times 1200}$ and all atoms (column vectors) are randomly selected from the training patches. It is easy to see that the sparse coefficients carry the more discriminative information in comparison with the raw images patches. Such a phenomenon gives us an intuitive clue that the sparse coefficients could help the objects classification in SAR imagery. Fig. 6.17 shows the distribution of original data of different objects and their corresponding sparse codes. In Fig. 6.17a each waveform indicates a sum of absolute intensity value of patch vectors from the same class. In Fig. 6.17b each waveform indicates a sum of absolute value of corresponding sparse vectors from the same class.

- **Classification:** In this section, the proposed multi-class classification method is adopted, which uses SVM and NN as the classifier, to perform the final classification and the following experiments are made using the data sets shown in Fig. 6.15. The ground truth points were determined via the reference data from National Land Cover Database of the United States and optical images acquired in the same period shown in Fig. 6.14. Consequently in a similar way, more than 30000 target pixels from these areas are randomly chose, and its locations, as well extracting more than 30000 patches to represent the target pixel in its centre. The patch size is 31×31 pixels. For the stage of training parameters D and W, the
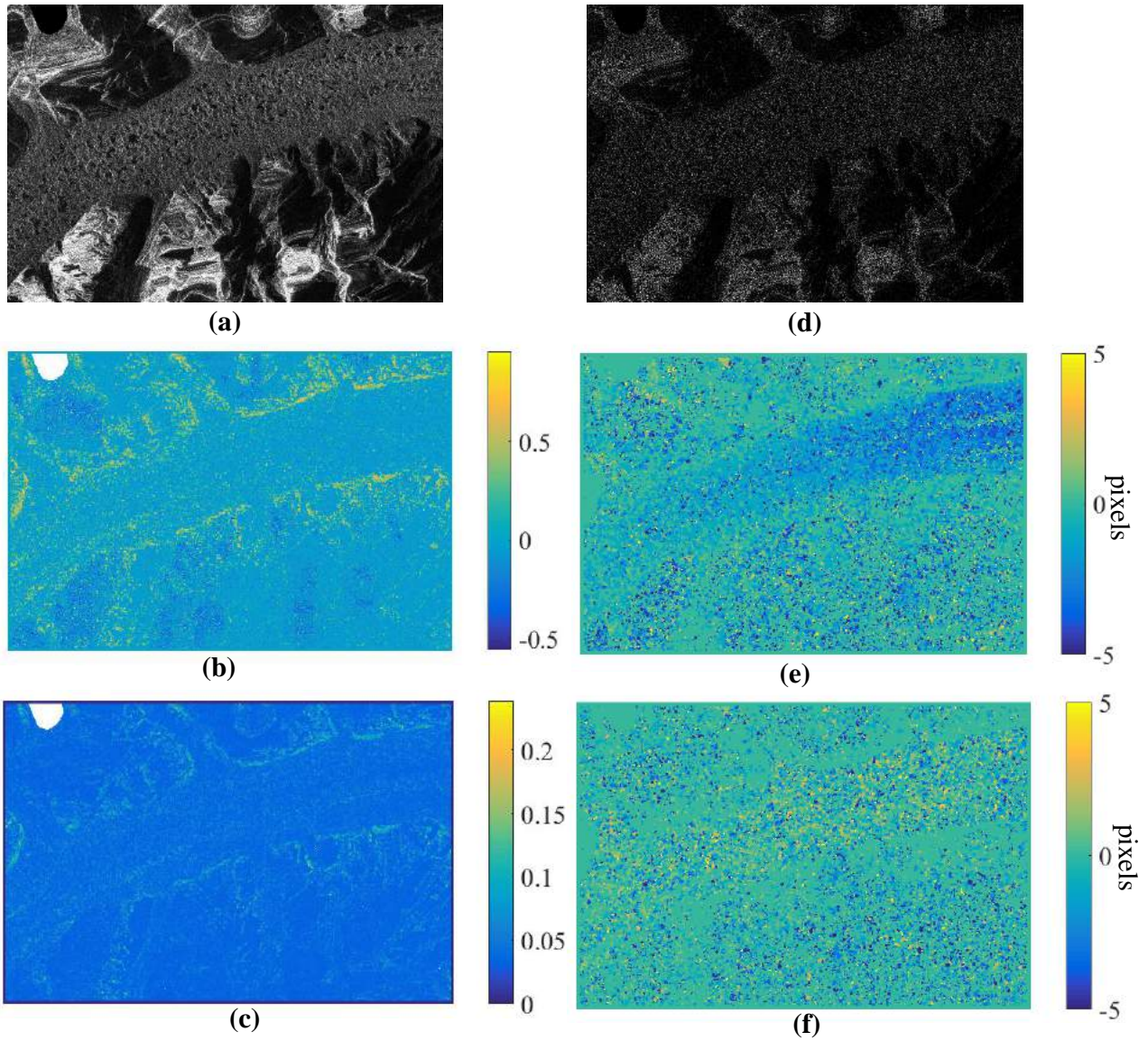
Figure 6.12: Results of the dense matching in Baltoro glacier. (a) TSX SAR intensity image, area of Baltoro glacier. (b) Map of correlation coefficients. (c) Map of SNR. (d) Image of selected point like features. (e) Disparity map in x-direction. (f) Disparity map in y-direction.
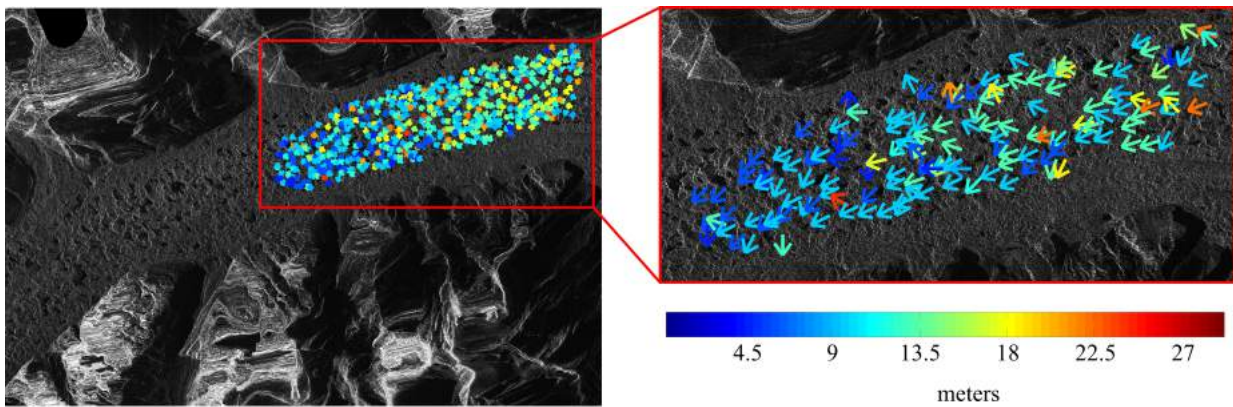
Figure 6.13: 2D motion field of the glacier surface in the selected image patches.
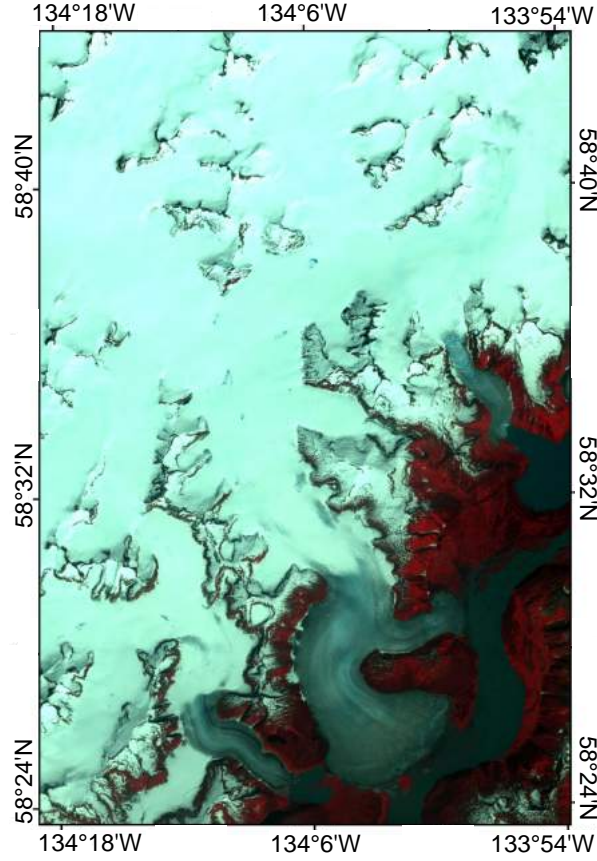
Figure 6.14: The study area around the Taku Glacier located in Alaska (the optical image is acquired in August, 2009, from Landsat-5).

training data of each class is randomly chose according to its size (i.e. 20% of wet snow and ice, 40% of water, NCR and others), and the rest for testing. For each test patch i denoting by its vector version x_i, the learning of its sparse representation x_i using learned dictionary D is firstly conducted, and then its reduced features y_i as well as its label l_i are obtained. Fig. 6.18 displays the optimization process of 25 iterations and the results achieve stability and convergence after 20 iterations, with the accuracy increased along with the incremental iteration times in a gently rising tendency. It is noteworthy that the accuracy will reach a maximal value when the iteration numbers increased larger than 22, with a value of approximately 0.9. The accuracy assessment of the proposed method is listed in Table 6.2 with an overall accuracy as 90.34%, which is higher than 87.96% (see Table 6.3) obtained by using SVM classifier directly on SAR intensity features.

Category	Wet snow	Ice	Water	NCR	Others
Wet snow	87.55%	0%	4.13%	0%	2.01%
Ice	11.80%	91.38%	0.91%	2.63%	1.38%
Water	0.25%	0.27%	88.79%	0.38%	4.0%
NCR	0.05%	4.11%	0.91%	93.61%	2.19%
Others	0.35%	4.24%	5.26%	3.3%	90.35%

overall accuracy = 90.34 %

Table 6.2: Confusion matrix of the proposed method.
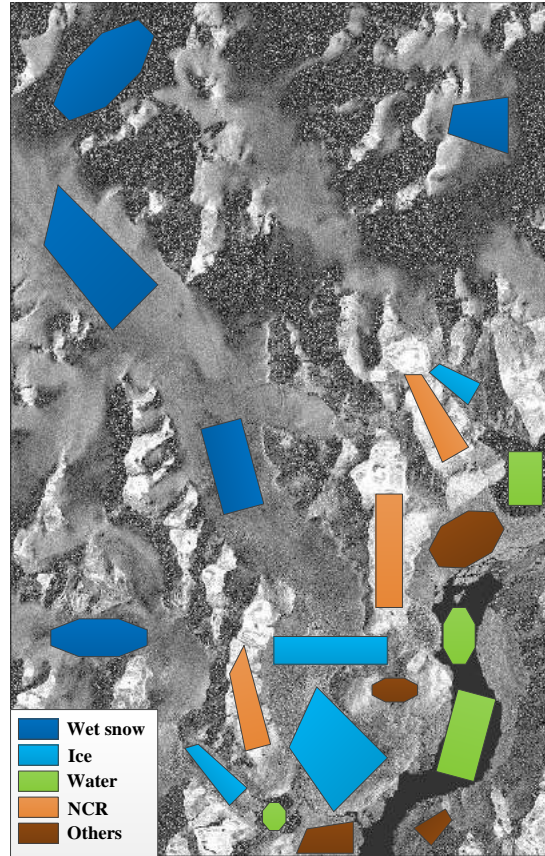
Figure 6.15: Experimental data sets obtained from the single polarization X-band SAR image.

Category	Wet snow	Ice	Water	NCR	Others
Wet snow	91.20%	7.03%	32.43%	0%	5.92%
Ice	1.95%	83.58%	0%	0%	11.85%
Water	6.30%	0%	64.86%	0%	0%
NCR	0	0.30%	0%	97.17%	11.85%
Others	0.54%	9.09%	2.70%	2.83%	70.38%

overall accuracy = 87.96 %

Table 6.3:   Confusion matrix of SVM.

Furthermore, in order to test different classifiers, the same SR and original intensity features are used to classify the SAR image. Two widely adopted methods, the Linear Discriminant Analysis (LDA) [Belhumeur et al., 1997] and direct LDA [Yu & Yang, 2001] combined with NN, are applied to examine the performance of the proposed method. Afterwards, the experimental results including the statistic of time consumptions and classification accuracy are listed in Table 6.4.

6.2.2   Dataset in the Baltoro Glacier

Aiming to validate the effectiveness and robustness of our proposed method, another case area, named the Baltoro glacier, which can represent discriminative characteristics of glaciers in light of dimensions, surface features, topography etc. is introduced to the experiments. Fig. 6.19 gives an overview of the Baltoro glacier and acts as a reference image, which acquired on November 24th, 2009.
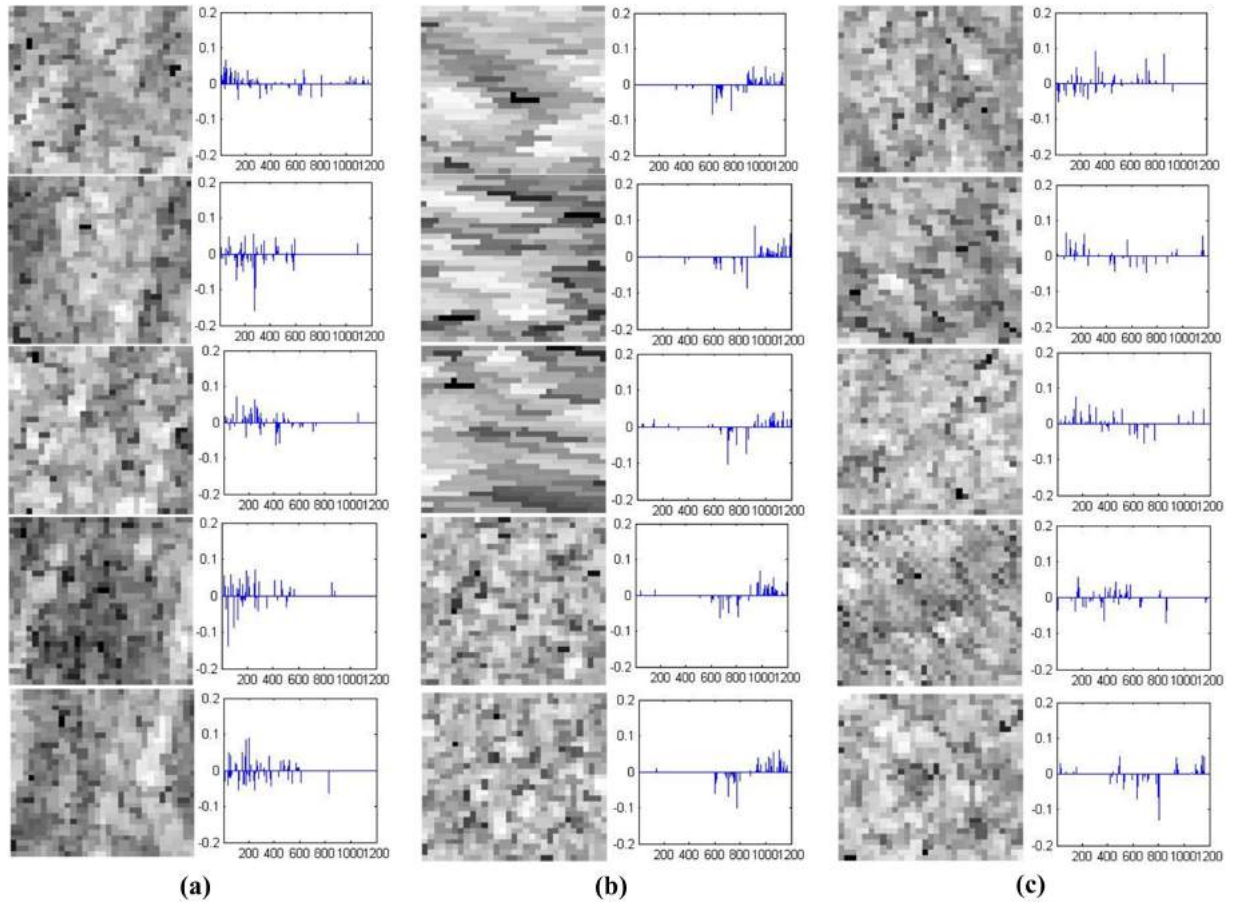
Figure 6.16: Oringinal image patches randomly selected from TerraSAR-X imagery and their corresponding sparse codes. X-axis: length of sparse vector; Y-axis: intensity value of sparse vector. (a) Different ice patches. (b) Different wet snow patches. (c) Different barren land patches.

Methods	Accuracy	learning time
Proposed method	90.05%	612.4410s
SVM on original data	87.96%	11057.3727s
LDA on SR	82.25%	1.1340s
LDA on original data	64.06%	0.3326s
Direct LDA on SR	82.83%	0.1960s
Direct LDA on original data	64.78%	1.1139s
Thresholds on original data	53.34%	0.0020s

Table 6.4: Classification Performance of the Proposed methods, LDA + NN, direct LDA + NN, and SVM on SR and original data

(a)

(b)

Figure 6.17: The comparison between the distribution of SAR data in original domain and in sparse domain. (a) The original intensity distribution of ground objects. X-axis: length of vector; Y-axis: averaged intensity value. (b) The sparse distribution of ground objects. X-axis: length of sparse vector; Y-axis: absolute value.
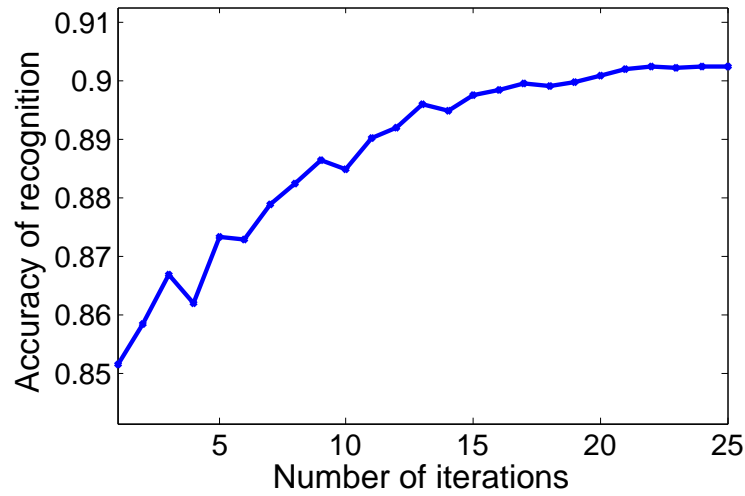
Figure 6.18: The lerning process of our method.
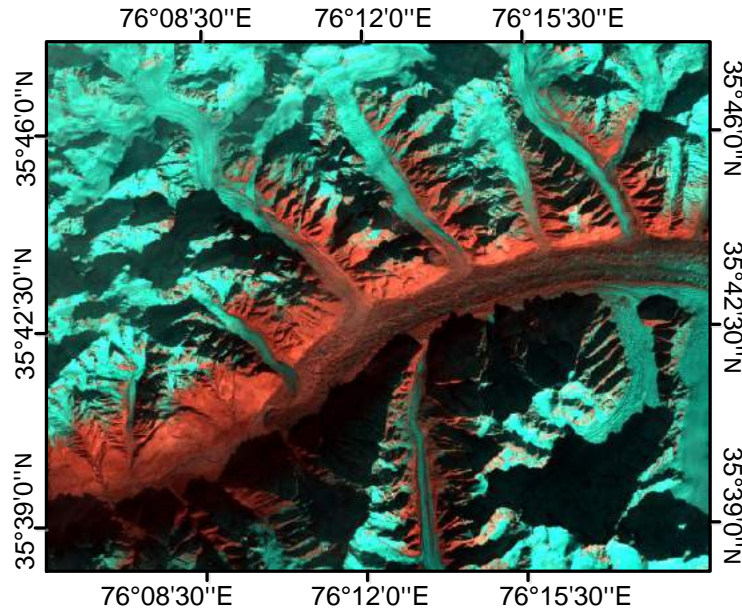
Figure 6.19: The study area around the Baltoro Glacier located in Karakorum mountain range (the optical image is acquired in November 24th, 2009, from Landsat-5).

In this case, the SM TSX EEC data acquired via single-polarization on December 24th, 2009 from descending obit is used. As topographical distortion of this type data has already been relieved via SRTM (90 m), the single-polarimetric intensity image is applied for classification only after the reduction of speckles via the aforementioned ARLee method.

Different with the Taku glacier featuring by the large covering area and a wide variety of ground objects, the Baltoro glacier is characterized by thick debris cover in its lower part and high relief topography. According to the former researches [Quincey et al., 2009; Veetti, 2009] and Landsat-5 image acquired one month before the SAR data due to the frequently strong cloud pollution in this high relief area (Fig. 6.19), during the cold season in this area, the land cover can be classified into five types: dry snow, ice, debris, NCR and others which include river outwash
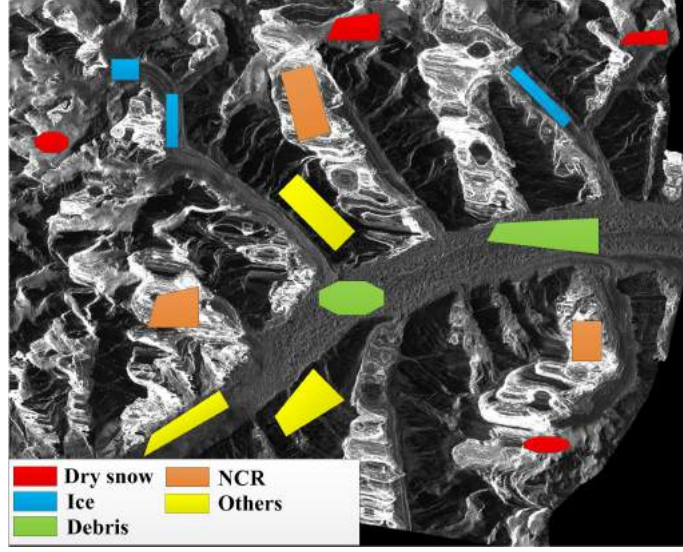
Figure 6.20: Experimental data sets obtained from the single polarization X-band SAR image.

and barren land, and the following classification experiments are made using the data sets shown in Fig. 6.20.

- **Classification:** Fig. 6.21 shows the distribution of original data and sparse codes. It can be apparently seen from Fig. 6.21b that the sparse distributions of the ground objects are more useful for classification than the original intensity distribution (see Fig. 6.21a). Based on the sparse information, the classification accuracy of our method is listed in Table 6.5, with an overall accuracy as 72.63% which is better than 68.69% derived by using SVM classifier directly on SAR intensity features.

Category	Dry snow	Ice	Debris	NCR	Others
Dry snow	52.20%	2.38%	1.48%	0.04%	0%
Ice	5.11%	55.01%	2.08%	2.51%	4.21%
Debris	1.12%	16.19%	90.14%	13.83%	11.18%
NCR	39.56%	22.33%	6.09%	82.24%	1.03%
Others	2.01%	4.09%	0.21%	1.38%	83.58%

overall accuracy = 72.63 %

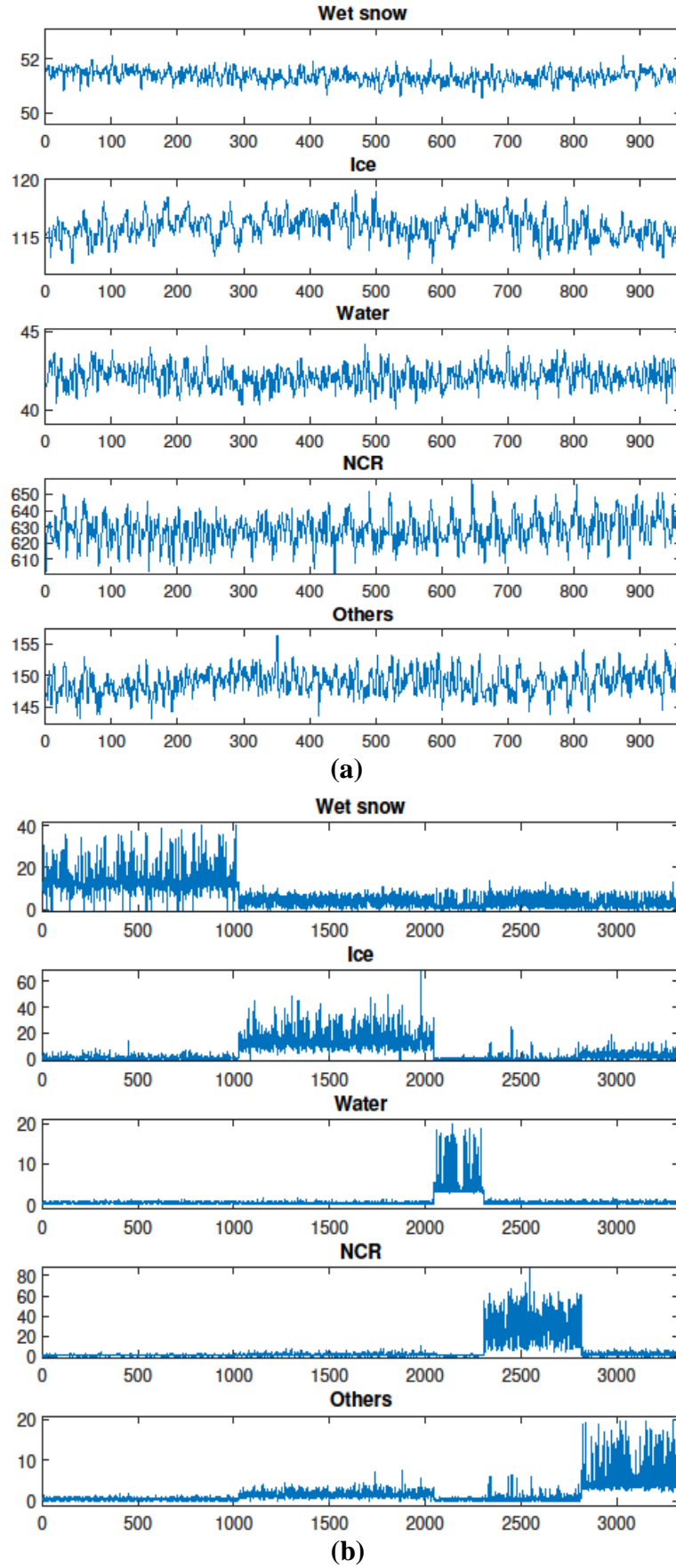Table 6.5: Confusion matrix of the proposed method.
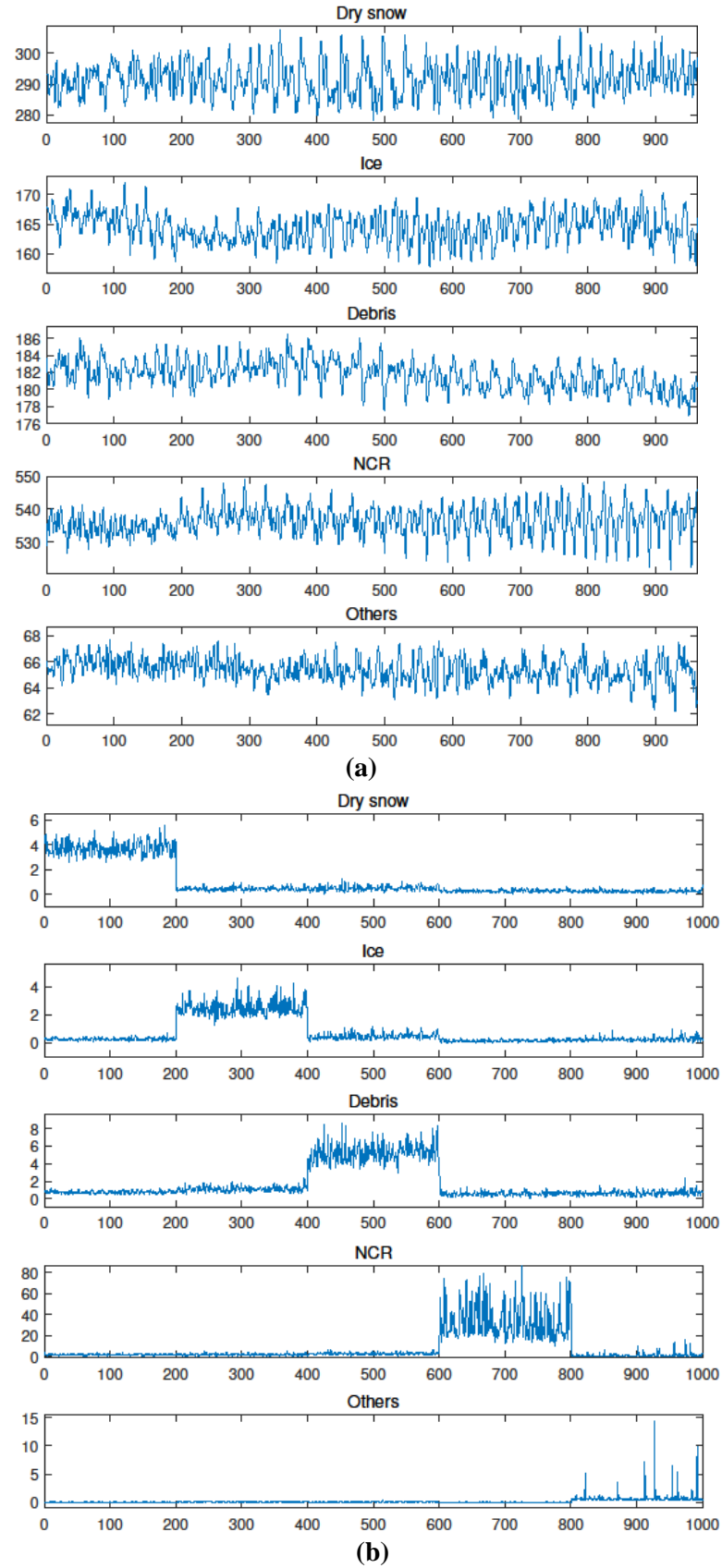
Figure 6.21: The comparison between the distribution of SAR data in original domain and in sparse domain. (a) The original intensity distribution of ground objects. X-axis: length of vector; Y-axis: averaged intensity value. (b) The sparse distribution of ground objects. X-axis: length of sparse vector; Y-axis: absolute value.

7 Discussion

In this Chapter, results presented in the previous Chapter 6 are discussed and evaluated. Similar to results, discussion is also organized in sections glacier surface motion (Section 7.1) and glacier surface classification (Section 7.2).

7.1 Glacier Surface Motion

7.1.1 Simulated SAR Dataset

- **Image Filtering:** It can be seen from Fig. 6.1 and Table 6.1 that the Boxcar filter shows the best performance of despeckling but details of image are sacrificed with sharp edges blurred, while the non-local mean filter preserves the most details of image with an inferior ability of removing speckles. In contrast, the proposed ARLee filter performs a good balance between reduction of speckles and preservation of details, with a good capability of keeping the sharp edges and corners and a relative acceptable competence of despeckling.

- **Robust PC Matching:** As shown Fig, 6.2, the results presents a tendency that for all the matching algorithms tested, their matching accuracies will decline with the increase of noise variance added. With the increasing level of multiplicative noise, it is clear that Hoge's PC method is inferior to other algorithms, which is quite sensitive to the growth of noise, with its RMSE and standard deviation is over 1 pixel when the noise variance increased. The NCC algorithm shows better accuracy compared with that of Hoge's, with its mean errors and standard deviation smaller than 1 pixel. Interestingly, the results of NCC and Foroosh's algorithm exhibits a fluctuation along with the noise level changing, which may reveals the instability of algorithm when dealing with image contaminated with large percent of noise. In contrast, the other PC based algorithms show better results, with their mean errors lower than 1 pixel and their standard deviation lower than 0.5 pixels, and they all have a relatively stable changing trend. Among all the PC based methods, the method presented in this thesis reports the best accuracy and robustness when noise accessing to the maximum level, which also appeals to be insensitive to the variation of noise with very stable error increasing plots.

7.1.2 Dataset in the Taku Glacier

- **Image Filtering:** It can be found that the proposed ARLee fitler can largely reduce the noise effect in the land area. Especially, in the boundary area crossing the glacier and the land (see Fig. 6.3f), the details of the boundary are preserved while the noise existing in the land and glacier is suppressed. In contrast, in the area of glacier containing a large present of ripple-like patterns of crevasses (see Fig. 6.3f), the patterns are well preserved but the effect of removing speckles seems not so significant. A mass of noise still remains in the glacier area. This is because in the calculation of weight parameter following Eq. 3.3, the speckle level σ_v can only be regarded as the standard to mean ratio for homogeneous areas,

but in the complex area shown in Fig.6.3f, the speckle level σ_v should be changed. However, in our current ARLee filter, we have not introduced an algorithm for adaptively confirm the speckle level. Fortunately, the following PLF selection process can help to suppress the unfiltered speckles as well.

- **Topographic Information Relief Image:** As seen in Fig.6.4, due to the errors of the external DEM data used, which have a lower ground resolution (30 m) and accuracy than the range-azimuth image, the ground surface are wrongly corrected in some areas as shown in Fig. 6.4c. For examples, the deformations of ridges in the Figs. 6.4cI and 6.4cIII as well as the empty hole in Fig. 6.4cII reveal the errors caused by the othorectification. However, it is found that the research interest, the Taku glacier placed in the southwest part of the Juneau ice field marked by a yellow box in Fig. 6.4b, is suffered little impact of othorectification errors because of its gentle topography.

- **Point Like Feature Selection:** Compared with the original SAR intensity image in Fig. 6.6a, Fig. 6.6b shows that only the pixels relating to a strong reflective target are selected. In this case, for the PLFs on the glacier surface, they are highly likely to be moraines, crevasses and wrinkles, which are in favor of the tracking process because of their independence and distinctiveness. It is also noteworthy that the selection of PLFs can also be regarded as a suppression of speckles and high frequency noise via filtering pixels of non-PLFs.

- **Dense Matching via Robust PC:** As seen in Fig.6.7, nevertheless, there are still some uncorrelated areas in the disparity maps appearing irregular spots in the result which indicate matching errors inducing by lack of correlation information. Such error areas can also be identified in the correlation map and SNR maps which featuring the low correlation coefficients and SNR values. In contrast to the image of PLFs as shown in Fig. 6.7d, it can be found that the low correlated areas in the disparity maps are mainly in correspondence with the areas with few PLFs. This relationship confirms that although the way of using PLFs can suppress unrelated noises and increase the robustness of dense matching, the selection of PLFs also have a significant influence on the final matching results in the workflow of proposed glacier monitoring approaches, which may decrease the whole matching result if distributions of PLFs in some areas are too sparse.

To refine the dense matching outcome, a median filter and a cutoff thresholds based on statistical histogram are applied to the disparity maps to eliminate the gross errors of matching. Here, the cutoff thresholds are identified by the histogram of displacements values from the disparity maps. The displacement values with low frequency of occurrence are deemed to be errors, since the movements of glacier surface in a neighborhood should have coherent values with a gentle changing tendency in reality. Therefore, abrupt displacement values with low frequency of occurrence representing the sudden changes of movement can be hardly likely happened in the real movement of glacier and to some extent such sudden changes will not influence our analysis of moving trends of glacier in large-scale measurement, so that they are filtered to refine the result of dense matching. Afterwards, the median filter is utilized as well in order to eliminate the rest noises (see Fig. 7.1).

- **Estimated Glacier Surface Motion:** One of the possible explanations of the motion trend of Taku glacier is because of the branch of this glacier in the middle left of the study area shunting the flow of glacier. To keep the mass balance, the ice in the bend of glacier should move towards northwest in order to fill the mass loss resulted from the branch. In light of the motion of glacier surface in a relative small scale, the trend illustrated in Fig. 6.8 implies that the movement of glacier surface is not performed in the form of a large and united moving block, rather a combination of small flowing patches with slight
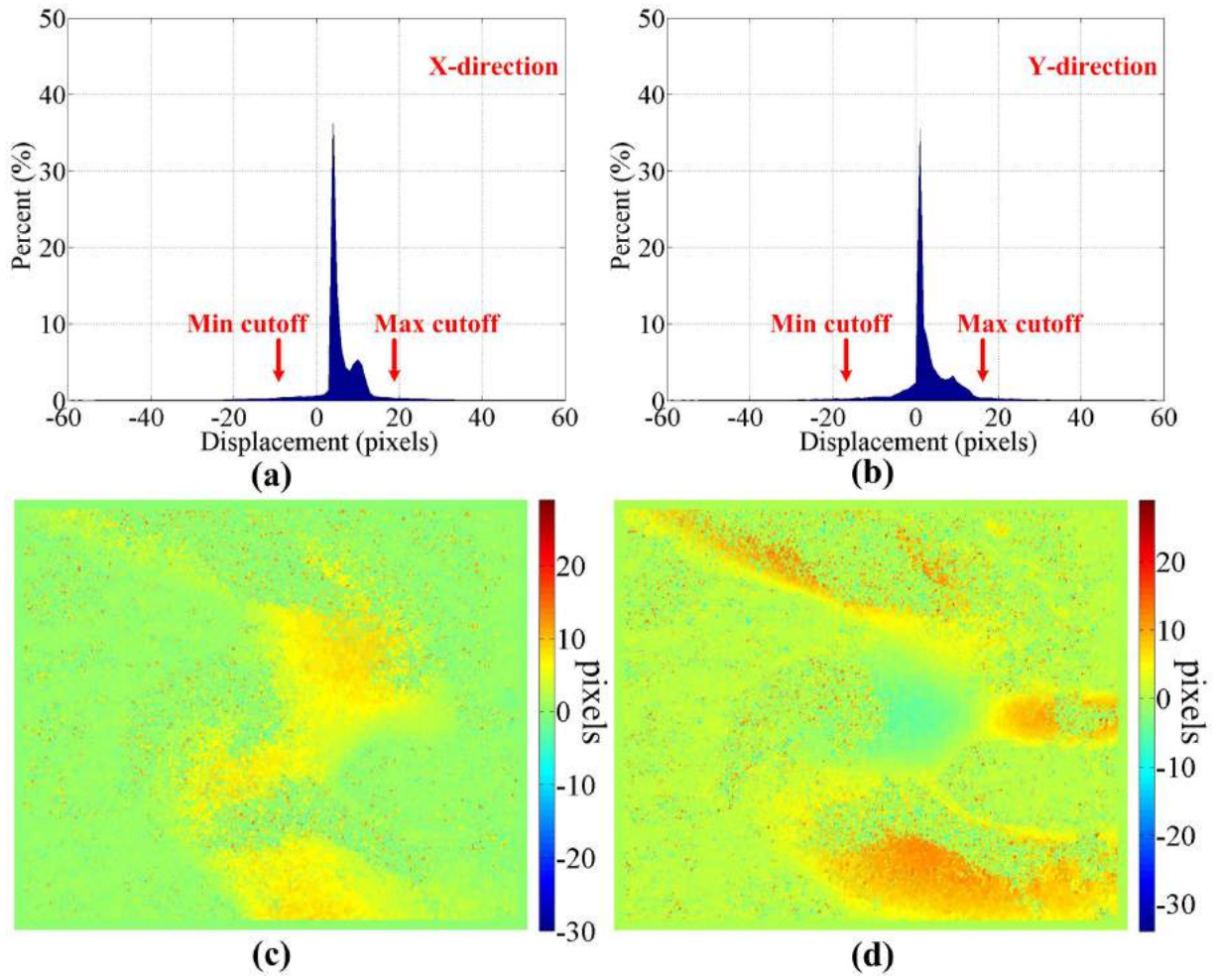
Figure 7.1: Refinement of the dense matching outcomes. (a) and (b) Histograms of disparity values and refinement thresholds. (c) Disparity maps in x-direction and (d) y-direction after refinement.

different movement magnitude and forming a united motion trend. Taking the time factor into consideration, it can also be deduced that the larger the moving velocity of the glacier area is, the more the small flowing patches with various velocities the glacier area have.

With respect to the first 2D motion field as shown in Fig. 6.9, it is worthy noticing that the ices of the glacier make an obvious turning along the moving direction with a changing magnitude of movement. By comparison, it can be confirmed that the movement of glacier's outlet reveals a coherent trend. However, from the variation of colors it can be figured out that the moving speed of ice patches approaching to the main body of glacier move faster than that located in the edge of the main body of glacier.

Moreover, as shown in Fig. 6.11, its corresponding 3D velocity field reveals that ice of glacier at the periphery of turning bend have a faster flow velocity than that in the center of the turning bend. The maximum velocity can reach as high as about 5 m per day in horizontal direction, which have a positive correlation with the changing velocity of elevation in vertical direction with a maximum value of around 5 cm per day.

7.1.3   Dataset in the Baltoro Glacier

- **Dense Matching via Robust PC:** It is obvious that, seen from Fig. 6.12, there exist more uncorrelated and error areas in the disparity maps appearing irregular spots which indicate matching bias induced by lack of correlation failures, especially when comparing with those of Taku glacier. All these errors can also be identified in the correlation map and SNR maps which show the low correlation coefficients and SNR.

  In contrast to the image of PLFs as shown in Fig. 6.12d, it can be found that the selection of PLFs show better performance than that in our former experiments for Taku glacier. This reveals that in the matching process, a more reliable result should be obtained benefiting from the sufficient pattern information. However, the matching results obtained still show a mass of outliers. To explain this, one reason relating to the earth covering the glacier surface is taken into consideration. The top surface of the Baltoro glacier is covered with earth, gravels or shingles, which have significantly different backscattering characteristics from the ice or snow. This debris-cover layer can also affect the penetration of SAR signals, which may shift the phase centers of signals. The shifts in phase centers will also have an impact on the intensity images. Another possible reason relating to debris-cover is about the data acquisition time in summer. The melting ice and snow not only contribute to the movement of glaciers, but also change the covering earth and gravels into mire mixtures, deforming the upper surface of glacier slightly. Considering the topographic situation, such a slight deformation can be enhanced, shown as a perpendicular motion of glacier, which is hardly to be measured from 2D images.

  Moreover, since the Baltoro glacier is located in Himalaya mountains, having more complex topography compared with the Junau icefield where the Taku glacier situated, it is more difficult to conduct an accurate topography relief process due to the lack of high resolution DEM dataset and layover phenomenon of SAR image. The errors caused by the topography relief can be observed in north-west part in Fig. 6.12a, where the mountains are apparently wrongly projected. Such errors will also influence our matching results.

- **Estimated Glacier Surface Motion:** It can be seen from the figures that the main trends of the 2D motion for the Baltoro glacier during the revisit period of 11 days are obtained. As seen from Fig. 6.12e and 6.12f, the motion of glacier surface in x- direction (west-east) can reach around 5 pixels equating to about 10 meters on the ground surface considering the ground resolution of 2.09 m for the orhtorectified image. While the glacier motion in y-direction (north-south) can is apparently disturbed by the uncertain results and errors, but main tendency of surface motion in this direction can also be recognized, with the maximum value reaching about 3 pixels. Moreover, the motion trend of glacier in x-direction is relatively stable, moving from the east to the west with its moving magnitude retarding. Nevertheless, the tendencies of glacier motion in y- direction seems to be unstable.

  Apparently, seen from Fig. 6.13, the 2D motion field is given in the glacier areas with complex and largest movements, due to the complex movement of glacier in y-direction. From the colors of these arrows, it can found the decelerating trend of the glacier movement. It is also notable that, the center parts of the ice stream in the glacier seem to have a faster moving speed than that in the boundary areas. One of the possible assumption for such phenomenon is that, the ice streams in the boundary areas are obstructed by the salient edges of the mountains locating in the side of the glacier. To sum up, it can be concluded that the movement of glacier's surface reveals a coherent trend, with a decelerating speed. From the variation of colors, it can be figured out that the detailed speeds and moving directions of ice patches have slight differences due to the uncertainty of matching results and the limitation of topographic situation.

7.2 Glacier Surface Classification

7.2.1 Dataset in the Taku Glacier

- **Sparse Information:** As seen from Fig. 6.17a, it is apparently that each waveform belong to an interval, for example, the average value of wet snow is in (47; 82), and it seems that these thresholds can be used to discriminate ground objects from each other efficiently and even as faster as the standard methods developed based on single polarization SAR BC image for the glacier snow and ice discrimination applied in several works [Brown, 2012; Huang et al., 2013; König et al., 2002, 2004]. However, in Fig. 7.2 a and b the histograms of different ground object classes over glacier area, as described in Fig.6.15, show that it is hard to discriminate wet snow, ice, barren land and vegetated area from each other because of having almost same BC values, and also Table 7.1 shows the unsatisfied classification result using thresholds directly on SAR intensity image, with 53.34% as the overall accuracy. It is proved that (isolated BC or intensity) value of each pixel itself in single polarization X-band SAR images is not important (even useless) for the glacier objects classification. Within opposite to this, compared to original data in Fig. 6.17a and b demonstrates the stronger separability of sparse representations.

Category	Interval	Accuracy
Wet snow	$(47, 82)$	32.38%
Ice	$(82, 132)$	74.95%
Water	$(0, 47)$	94.46%
NCR	$(380, max)$	62.61%
Others	$(132.5, 380)$	70.44%
overall accuracy = 53.34 %		

Table 7.1: Classification Performance based on intensity thresholds using original data.

- **Classification:** Seen from Table 6.2 and 6.3, it is found that the SR features has the better performance in overall accuracy. Except the classes of wet snow and NCR, the other classes are highly accurate for the two groups of features. In SR features space, the wet snow is confused with ice so that 11.8% is wrongly assigned to ice about 10% higher than that in original intensity space, but distinguished from water better with an increasing value of about 6%. Additionally, the NCR is also wrongly classified as ice with an increased value of 2.63%. However, due to the extreme brightness, the NCR is obviously distinguished from neighboring objects resulting in high classification performance in both feature space. The accuracy of water is relatively lower in both feature groups. Only 88.79% of it is recognized increased by about 24% even when using SR features. This should be reasoned by the textureless of water in SAR images. The others comprised by barren land (rock/sand/clay) and vegetated area including forest area, grass land and wetland have the most complicated scattering mechanism, so that in original intensity space only 70.38% is recognized. However, this has been hugely improved in SR features space with an accuracy of 90.35%.

Furthermore, as shown in Table 6.4, it can be concluded that the proposed method has the better performance on classification accuracy. The method proposed in this thesis is almost 20 times faster than the traditional used SVM method which obtained the second best performance on classification accuracy. Due to the two layers setting of the proposed framework, it observed that the other popular methods (e.g. LDA) are much faster than the proposed method, but this could be negligible while considering the better performance.
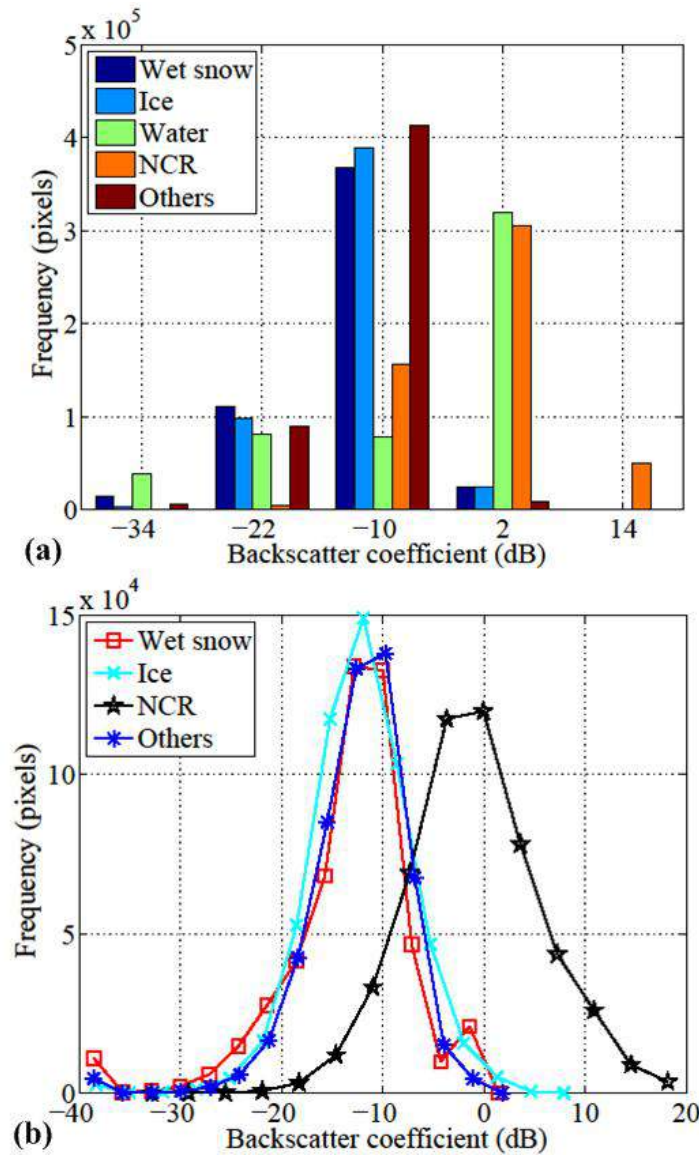
Figure 7.2: Histograms of the aforementioned data sets after been processed into BC values following Li et al. [2012], displayed in (a) bar graph and (b) curve graph.

7.2.2   Dataset in the Baltoro Glacier

- **Classification:** As shown in Table 6.5, the classification accuracy of dry snow is slightly above 50% with 40% wrongly assigned to NCR, which should be due to the strong backscattering behavior of dry snow in X-band SAR images. In ice area, 55% of the pixels are recognized as ice, with the rest mostly falsely classified as debris or NCR. However, 90% of the pixels in debris area are correctly classified as debris, which increases the capability of this method on automatic debris mapping helping the glaciologists to discriminate the debris from bare ice.

  Considering on SAR imagery, the speckles, shadows and foreshortening effects are inevitably hampering the performance of final classification result (72.63% as the overall accuracy). The speckles can be controlled in an acceptable extent through the ARLee filter. Unfortunately, the shadows and layovers disadvantages of SAR images are much more serious around the Baltoro glacier than in the Taku glacier due to its high relief topography and

low resolution DEM (SRTM with 90 m resolution) available in this area which helps for the reduction of topography distortions in SAR images. It is also found that the missing information resulted by SAR shadows and layovers make small glaciers located in narrow valley disappeared in SAR data contributing to a reduction on final classification performance.

8 Conclusion and Perspective

8.1 Summary and Conclusion

In this thesis, the proposed processing workflow for the glaciers monitoring task involving the quantitive estimation of glacier surface motion and the multi-classes classification on and around the glacier surface areas using spaceborne SAR intensity images have been proposed and evaluated with different research areas and datasets, separately.

The glacier surface motion estimation results obtained via PLFs and the robust PC algorithm under a variety of tests using simulated dataset as well as the actual application of glacier monitoring confirm the superiority and feasibility of the proposed approaches; The multi-objects classification on and around the glaciers is conducted based on the supervised classification method using SAR intensity image, taking the advantages of the local discrimination of SR as well as the relationships between target pixel and the information in its neighborhood, which focuses on the local geometry of image patches. The obtained classification results under a variety of tests on two glaciers representing discriminative characteristics of glaciers in light of dimensions, surface features, topography, climatic setting etc., confirm the superiority and feasibility of the proposed method on glacier mapping.

Several conclusions can be drawn, shown as following:

- The proposed ARLee filter provides an acceptable despeckling result and can keep a good balance between the suppression of noise and the preservation of image details.

- The presented robust PC algorithm outperform the commonly used correlation algorithms with a better accuracy and robustness when matching SAR intensity images in the context of multiplicative noise with various noise levels.

- The presented experimental results reveal that the effectiveness of the proposed robust PC is highly depend on the performance of selecting PLFs. The better the PLFs are selected, the more robust and effective the proposed PC algorithm can perform.

- With the proposed PC algorithm, the motion of glaciers can be estimated, with detailed dense ice movements obtained.

- However, there are still some drawbacks of our current method for the motion estimation. For the preservation of details and patterns in the SAR image, in our cases, only the patterns of edges and corners are considered. More details like curvature and dot-like patterns are neglected. Moreover, in the selection of PLF, setting appropriate parameters for the 2-D Sinc-function template is still an empirical work, which will significantly influence the performance of PLF. As for the PC method we used, the changes caused by rotation and scale are not included, which may lead to the loss of motion information.

- The results demonstrate that the use of SR can generate appropriate discriminative information making the single-polarization spaceborne SAR data characterized with wider coverage and huge amount of archives be useful for glacier mapping tasks.

- The geometry relationships between target pixel and its neighboring pixels effectively enrich the information existing in this resolution cell of single-polarization SAR image. Additionally, the proposed method can avoid the worst case of misclassification among the points that share the distance similarity but from different classes.

- The proposed method for multi-objects classification on and around glaciers has better performance than the commonly used classification methods considering classification accuracy and time consuming.

- Nevertheless, there is also some drawbacks of the proposed classification method. Although we have developed an effective feature extraction algorithm, the classification will still be affected by the performance of the classifier (i.e., SVM) we used. For instance, problems like overfitting frequently occurring in the training of SVM will have a negative impact on the classification results. Besides, the efficiency of our optimization method are also needed to be improved.

8.2   Future Work

The findings of this work have showed some potential topics for further research:

- The improvement of the filtering method having better abilities to cope with speckles while preserving more details and patterns in the SAR images.

- The improvement of the matching algorithm with respect to better robustness in diverse noise levels and different types of displacements. The investigation on its application for challenging texture-poor conditions is also interesting as well. In addition, more SAR datasets with different channels and bands will be tested and analyzed, in order to digest further information and relationships between the different electromagnetic and snow/ice characteristics, when dealing with SAR image matching work.

- The shadows and layovers disadvantages of SAR images are much more serious around the glaciers characterized by high-relief topography, such as the Baltoro glacier, which introduces much information missing in SAR images (e.g., small glaciers located in narrow valley disappeared in SAR data), resulting a worse glacier mapping result. The use of other complementary dataset such as optical and lidar data will be tested, in order to improve the final classification performance.

- Combining our proposed feature extraction algorithm with more robust and effective classifiers like the popular deep learning based Convolutional Neural Networks will also be tested, in order to yield the greatest returns on our classification method.

Bibliography

Abdelfattah R, Nicolas JM (2005) InSAR image co-registration using the Fourier-Mellin transform. International Journal of Remote Sensing, 26 (13): 2865–2876.

Abdou IE (1999) Practical approach to the registration of multiple frames of video images. In: Proc. SPIE Conf. Vis. Comm. Image Process.: 371–382.

Aharon M, Elad M, Bruckstein A (2006) K-SVD: An algorithm for designing overcomplete dictionaries for sparse representation. IEEE Transactions on Signal Processing, 54 (11): 4311–4322.

Akbari V, Doulgeris A, Eltoft T (2014) Monitoring glacier changes using multitemporal multipolarization SAR images. IEEE Transactions on Geoscience and Remote Sensing, 52 (6): 3729–3741.

Althof R, Wind M, Dobbins J (1997) A rapid and automatic image registration algorithm with subpixel accuracy. Medical Imaging, IEEE Transactions on, 16 (3): 308–316.

Ansari R, Mohan B (2014) Noise Filtering of Remotely Sensed Images using Iterative Thresholding of Wavelet and Curvelet Transforms. The International Archives of Photogrammetry, Remote Sensing and Spatial Information Sciences, 40 (1): 57.

Atwood D, Meyer F, Arendt A (2010) Using L-band SAR coherence to delineate glacier extent. Canadian Journal of Remote Sensing, 36: S186–S195.

Baghdadi N, Gauthier Y, Bernier M (1997) Capability of multitemporal ERS-1 SAR data for wet-snow mapping. Remote Sensing of Environment, 60: 174–186.

Bamler R, Eineder M (2005) Accuracy of differential shift estimation by correlation and split-bandwidth interferometry for wideband and delta-k SAR systems. IEEE Geoscience and Remote Sensing Letters, 2 (2): 151–155.

Bamler R, Hartl P (1998) Synthetic aperture radar interferometry. Inverse problems, 14 (4): R1.

Bechor BN, Zebker HA (2006) Measuring two dimensional movements using a single InSAR pair. Geophysical research letters, 33 (16).

Belhumeur P, Hespanha J, Kriegman D (1997) Eigenfaces vs. fisherfaces: Recognition using class specific linear projection. Pattern Analysis and Machine Intelligence, IEEE Transactions on, 19 (7): 711–720.

Benson CS (1962) Stratigraphic Studies in the Snow and Firn of the Greenland Ice Sheet, volume 70. US Department of Commerce, Office of Technical Services.

Berthier E, Vadon H, Baratoux D, Arnaud Y, Vincent C, Feigl K, Rémy F, Legrésy B (2005) Surface motion of mountain glaciers derived from satellite optical imagery. Remote Sensing of Environment, 95: 14–28.

Bethmann F, Luhmann T (2011) Least-squares matching with advanced geometric transformation models. Photogrammetrie-Fernerkundung-Geoinformation, 2011 (2): 57–69.

Bhambri R, Bolch T, Chaujar K (2011) Mapping of debris-covered glaciers in the Garhwal Himalayas using ASTER DEMs and thermal data. International Journal of Remote Sensing, 32: 8095–8119.

Brown I (2012) Synthetic aperture radar measurements of a retreating firn line on a temperate icecap. IEEE Journal of Selected Topics in Applied Earth Observations and Remote Sensing, 5 (1): 153–160.

Buades A, Coll B, Morel J (2005) A non-local algorithm for image denoising. In: Computer Vision and Pattern Recognition, 2005. CVPR 2005. IEEE Computer Society Conference on, 2: 60–65.

Bufford T, Chen Y, Horning M, Shee L (2013) When Dictionary Learning Meets Classification.

Cumming I, Zhang J (1999) Measuring the 3-D flow of the Lowell Glacier with InSAR. In: Proceedings of ESA Fringe'99 Meeting

Dai C, Zheng Y, Li X (2006) Accurate video alignment using phase correlation. IEEE Signal Process. Lett., 13 (12): 737–740.

de Lange R, Luckman A, Murray T (2007) Improvement of satellite radar feature tracking for ice velocity derivation by spatial frequency filtering. IEEE Transactions on Geoscience and Remote Sensing, 45 (7): 2309–2318.

Debella-Gilo M, Kääb A (2011) Sub-pixel precision image matching for measuring surface displacements on mass movements using normalized cross-correlation. Remote Sensing of Environment, 115 (1): 130–142.

Debella-Gilo M, Kääb A (2012) Measurement of surface displacement and deformation of mass movements using least squares matching of repeat high resolution satellite and aerial images. Remote sensing, 4 (1): 43–67.

Debella-Gilo M, Kääb A (2012) Locally adaptive template sizes for matching repeat images of Earth surface mass movements. ISPRS Journal of Photogrammetry and Remote Sensing, 69: 10–28.

Derauw D (1999) DInSAR and coherence tracking applied to glaciology: The example of Shirase Glacier. In: Proc. FRINGE'99

Dozier J (1989) Spectral signature of alpine snow cover from Landsat 5 TM. Remote Sensing of Environment, 28: 9–22.

Efron B, Hastie T, Johnstone L, Tibshirani R et al. (2004) Least angle regression. The Annals of statistics, 32 (2): 407–499.

Elad M, Aharon M (2006) Image denoising via sparse and redundant representations over learned dictionaries. Image Processing, IEEE Transactions on, 15 (12): 3736–3745.

Engeset R, Weydahl D (1998) Analysis of glaciers and geomorphology on Svalbard using multitemporal ERS-1 SAR images. IEEE Transactions on Geoscience and Remote Sensing, 36 (6): 1879–1887.

Erten E, Reigber A, Hellwich O (2009) Glacier velocity monitoring by maximum likelihood texture tracking. IEEE Transactions on Geoscience and Remote Sensing, 47 (2): 394–405.

Fahnestock M, Bindschadler R, Kwok R, Jezek K (1993) Greenland Ice-Sheet surface-properties and ice dynamics from ERS-1 SAR imagery. Science, 262 (5139): 1530–1534.

Fallourd R, Harant O, Trouve E, Nicolas J, Gay M, Walpersdorf A, Mugnier J, Serafini J, Rosu D, Bombrun L, Vasile G, Cotte N, Vernier F, Tupin F, Moreau L, Bolon P (2011) Monitoring temperate glacier displacement by multi-temporal TerraSAR-X images and continuous GPS measurements. IEEE Journal of Selected Topics in Applied Earth Observations and Remote Sensing, 4 (2): 372–386.

Faugeras O, Hotz B, Mathieu H, Viéville T, Zhang Z, Fua P, Théron E, Moll L, Berry G, Vuillemin J et al. (1993) Real time correlation-based stereo: algorithm, implementations and applications. Inria, Technical report.

Feng J, Cao Z, Pi Y (2014) Polarimetric contextual classification of PolSAR images using sparse representation and superpixels. Remote Sensing, 6 (8): 7158–7181.

Floricioiu D, Eineder M, Rott H, Nagler T (2008) Velocities of major outlet glaciers of the Patagonia Icefield observed by TerraSAR-X. In: IEEE International Geoscience and Remote Sensing Symposium (IGARSS), 4: 347–350.

Foroosh H, Balci M (2004) Sub-pixel registration and estimation of local shifts directly in the Fourier domain. In: Proc. Int. Conf. Image Process.: 1915–1918.

Foroosh H, Zerubia JB, Berthod M (2002) Extension of phase correlation to subpixel registration. IEEE Transaction on Image Process, 11 (3): 188–200.

Gao J, Shi Q, Caetano T (2012) Dimensionality reduction via compressive sensing. Pattern Recognition Letters, 33 (9): 1163–1170.

Gardner A, Moholdt G, Cogley J, Wouters B, Arendt A, Wahr J, Berthier E, Hock R, Pfeffer W, Kaser G et al. (2013) A reconciled estimate of glacier contributions to sea level rise: 2003 to 2009. Science, 340 (6134): 852–857.

Goldstein R, Engelhardt H, Kamb B, Frolich R (1993) Satellite Radar interferometry for monitoring ice-sheet motion-Application to an Antarctic ice stream. Science, 262 (5139): 1525–1530.

Gonzalez PJ, Chini M, Stramondo S, Fernández J (2010) Coseismic horizontal offsets and fault-trace mapping using phase correlation of IRS satellite images: The 1999 Izmit (Turkey) earthquake. IEEE Trans. Geosci. Remote Sens., 48 (5): 2242–2250.

Goodman J (1976) Some fundamental properties of speckle*. JOSA, 66 (11): 1145–1150.

Gourmelen N, Kim SW, Shepherd A, Park JW, Sundal AV, Björnsson H, Palsson F (2011) Ice velocity determined using conventional and multiple-aperture InSAR. Earth and Planetary Science Letters, 307 (1): 156–160.

Gray A, Short N, Mattar K, Jezek K (2001) Velocities and flux of the Filchner ice shelf and its tributaries determined from speckle tracking interferometry. Canadian Journal of Remote Sensing, 27: 193–206.

Guha T, Ward R (2012) Learning sparse representations for human action recognition. Pattern Analysis and Machine Intelligence, IEEE Transactions on, 34 (8): 1576–1588.

Gupta RP, Haritashya U, Singh P (2005) Mapping dry/wet snow cover in the Indian Himalayas using IRS multispectral imagery. Remote Sensing of Environment, 97: 458–469.

Hawe S, Seibert M, Kleinsteuber M (2013) Separable dictionary learning. In: IEEE Conference on Computer Vision and Pattern Recognition (CVPR): 438–445.

He X, Cai D, Yan S, Zhang H (2005) Neighborhood preserving embedding. In: Computer Vision, 2005. ICCV 2005. Tenth IEEE International Conference on, 2: 1208–1213.

Heid T, Kääb A (2012) Evaluation of existing image matching methods for deriving glacier surface displacements globally from optical satellite imagery. Remote Sensing of Environment, 118: 339–355.

Ho HT, Goecke R (2008) Optical flow estimation using Fourier Mellin transform. In: Proc. CVPR: 1–8.

Hoge WS (2003) A subspace identification extension to the phase correlation method [MRI application]. IEEE Transaction Medicine Image, 22 (2): 277–280.

Hu J, Li ZW, Li J, Zhang L, Ding XL, Zhu JJ, Sun Q (2014a) 3-D movement mapping of the alpine glacier in Qinghai-Tibetan Plateau by integrating D-InSAR, MAI and Offset-Tracking: Case study of the Dongkemadi Glacier. Global and Planetary Change, 118: 62–68.

Hu X, Wang T, Liao M (2014b) Measuring coseismic displacements with point-like targets offset tracking. IEEE Geoscience and Remote Sensing Letters, 11 (1): 283–287.

Huang L, Li Z, Tian B, Chen Q, Liu J, Zhang R (2011) Classification and snow line detection for glacial areas using the polarimetric SAR image. Remote Sensing of Environment, 115 (7): 1721–1732.

Huang L, Li Z, Tian B, Chen Q, Zhou J (2013) Monitoring glacier zones and snow/firn line changes in the Qinghai-Tibetan Plateau using C-band SAR imagery. Remote Sensing of Environment, 137: 17–30.

Ito K, Nakajima H, Kobayashi K, Higuchi T (2004) A fingerprint matching algorithm using phase-only correlation. IEICE Trans. Fundam. Electron. Commun. Comput. Sci., 87 (3): 682–691.

Jaenicke J, Mayer C, Scharrer K, Munzer U, Gudmundsson A (2006) The use of remote-sensing data for mass-balance studies at Myrdalsjokull ice cap, Iceland. Journal of Glaciology, 52: 565–573.

Jiang Y, Zhang G, Tang X, Li D, Huang W, Pan H (2014) Geometric calibration and accuracy assessment of ZiYuan-3 multispectral images. IEEE Trans. Geosci. Remote Sens., 52 (7): 4161–4172.

Jiang Z, Lin Z, Davis L (2013) Label consistent K-SVD: Learning a discriminative dictionary for recognition. Pattern Analysis and Machine Intelligence, IEEE Transactions on, 35 (11): 2651–2664.

Joughin I, Kwok R, Fahnestock M (1998) Interferometric estimation of three-dimensional ice-flow using ascending and descending passes. IEEE Transactions on Geoscience and Remote Sensing, 36 (1): 25–37.

Joughin I, Smith B, Abdalati W (2010) Glaciological advances made with interferometric synthetic aperture radar. Journal of Glaciology, 56 (200): 1026–1042.

Kargel J, Abrams M, Bishop M, Bush A, Hamilton G, et al HJ (2005) Multispectral imaging contributions to global land ice measurements from space. Remote Sensing of Environment, 99: 187–219.

Karvonen J, Cheng B, Vihma T, Arkett M, Carrieres T (2012) A method for sea ice thickness and concentration analysis based on SAR data and a thermodynamic model. The Cryosphere, 6 (6): 1507–1526.

Keller Y, Averbuch A (2007) A projection-based extension to phase correlation image alignment. Signal Process., 87 (1): 124–133.

König M, Wadham J, Winther JG, Kohler J, Nuttall AM (2002) Detection of superimposed ice on the glaciers Kongsvegen and midre Love´ nbreen, Svalbard, using SAR satellite imagery. Annals of Glaciology, 34 (1): 335–342.

König M, Winther J, Isaksson E (2001) Measuring snow and glacier ice properties from satellite. Reviews of Geophysics, 39: 1–27.

König M, Winther J, Kohler J, König F (2004) Two methods for firn-area and mass-balance monitoring of Svalbard glaciers with SAR satellite images. Journal of Glaciology, 50 (168): 116–128.

Komarov AS, Barber DG (2014) Sea ice motion tracking from sequential dual-polarization RADARSAT-2 images. IEEE Transactions on Geoscience and Remote Sensing, 52 (1): 121–136.

Kuan D, Sawchuk A, Strand T, Chavel P (1985) Adaptive noise smoothing filter for images with signal-dependent noise. Pattern Analysis and Machine Intelligence, IEEE Transactions on, (2): 165–177.

Kuglin C (1975) The phase correlation image alignment method. In: Proc. Int. Conf. on Cybernetics and Society, 1975: 163–165.

Kumar S, Azartash H, Biswas M, Nguyen T (2011) Real-time affine global motion estimation using phase correlation and its application for digital image stabilization. IEEE Transaction on Image Process, 20 (12): 3406–3418.

Kumara V, Venkataramanaa G, Høgdab K (2011) Glacier surface velocity estimation using SAR interferometry technique applying ascending and descending passes in Himalayas. International Journal of Applied Earth Observation and Geoinformation, 13: 545–551.

Kwok R, Fahnestock M (1996) Ice sheet motion and topography from radar interferometry. IEEE Transactions on Geoscience and Remote Sensing, 34 (1): 189–200.

Lang F, Yang J, Li D, Zhao L, Shi L (2014) Polarimetric SAR image segmentation using statistical region merging. Geoscience and Remote Sensing Letters, IEEE, 11 (2): 509–513.

Lee J (1980) Digital image enhancement and noise filtering by use of local statistics. Pattern Analysis and Machine Intelligence, IEEE Transactions on, (2): 165–168.

Lee J (1981) Refined filtering of image noise using local statistics. Computer graphics and image processing, 15 (4): 380–389.

Lee J (1986) Speckle suppression and analysis for synthetic aperture radar images. Optical engineering, 25 (5): 255636–255636.

Lee J, Grunes M, Grandi GD (1999) Polarimetric SAR speckle filtering and its implication for classification. Geoscience and Remote Sensing, IEEE Transactions on, 37 (5): 2363–2373.

Lee JS (1989) Speckle analysis and smoothing of synthetic aperture radar images. Computer graphics and image processing, 17 (1): 24–32.

Leprince S, Barbot S, Ayoub F, Avouac JP (2007) Automatic and precise orthorectification, coregistration, and subpixel correlation of satellite images, application to ground deformation measurements. IEEE Trans. Geosci. Remote Sens., 45 (6): 1529–1558.

Leprince S, Musé P, Avouac JP (2008) In-flight CCD distortion calibration for pushbroom satellites based on subpixel correlation. IEEE Trans. Geosci. Remote Sens., 46 (9): 2675–2683.

Lewis JP (1995) Fast normalized cross-correlation. Vision interface, 10 (1): 120–123.

Li S, Benson C, Gens R, Lingle C (2008) Motion patterns of Nabesna Glacier (Alaska) revealed by interferometric SAR techniques. Remote Sensing of Environment, 112: 3628–3638.

Li Z, Huang L, Chen Q, Tian B (2012) Glacier snow line detection on a polarimetric SAR image. IEEE Geoscience and Remote Sensing Letters, 9 (4): 584–588.

Li Z, Wang J (2014) Least squares image matching: A comparison of the performance of robust estimators. ISPRS Annals of the Photogrammetry, Remote Sensing and Spatial Information Sciences, 2 (1): 37.

Liu J, Yan H (2008) Phase correlation pixel-to-pixel image coregistration based on optical flow and median shift propagation. Int. J. Remote Sens., 29 (20): 5943–5956.

Liu JG, Yan H (2006) Robust phase correlation methods for sub-pixel feature matching. In: Proc. 1st Annu. Conf. Syst. Eng. Auton. Syst.: A13.

Liu W, Yamazaki F (2013) Detection of crustal movement from TerraSAR-X intensity images for the 2011 Tohoku, Japan Earthquake. IEEE Geoscience and Remote Sensing Letters, 10 (1): 199–203.

Lucchitta B, Ferguson H (1986) Antarctica: measuring glacier velocity from satellite images. Science, 234 (4780): 1105–1108.

Lucchitta BK, Mullins KF, Allison AL, Ferrigno JG (1993) Antarctic glacier-tongue velocities from Landsat images: first results. Annals of Glaciology, 17: 356–366.

Luckman A, Quincey D, Bevan S (2007) The potential of satellite radar interferometry and feature tracking for monitoring flow rates of Himalayan glaciers. Remote Sensing of Environment, 111: 172–181.

Luckmann A, Tansey K, Schmullius C (2004) The construction of ERS-tandem and JERS SAR image mosaics for large-scale mapping of boreal forest in Siberia. International Journal of Remote Sensing, 25: 751–768.

Mairal J, Bach F, Ponce J (2012) Task-driven dictionary learning. Pattern Analysis and Machine Intelligence, IEEE Transactions on, 34 (4): 791–804.

Mairal J, Ponce J, Sapiro G, Zisserman A, Bach F (2009) Supervised dictionary learning. In: Advances in neural information processing systems: 1033–1040.

Maksymiuk O, Mayer C, Stilla U (2016) Velocity estimation of glaciers with physically-based spatial regularization-Experiments using satellite SAR intensity images. Remote Sensing of Environment, 172: 190–204.

Mattar KE, Vachon PW, Geudtner D, Cumming IG, Brugman M (1998) Validation of alpine glacier velocity measurements using ERS tandem-mission SAR data. IEEE Transactions on Geoscience and Remote Sensing, 36 (3): 974–984.

Michel R, Rignot E (1999) Flow of Moreno Glaciar, Argentina, from repeat-pass Shuttle Imaging Radar images: Comparison of the phase correlation method with radar interferometry. Journal of Glaciology, 45 (149): 93–100.

Moré J, Thuente D (1994) Line search algorithms with guaranteed sufficient decrease. ACM Transactions on Mathematical Software (TOMS), 20 (3): 286–307.

Morgan GLK, Liu JG, Yan H (2010) Precise subpixel disparity measurement from very narrow baseline stereo. IEEE Trans. Geosci. Remote Sens., 48 (9): 3424–3433.

Motyka RJ, Beget JE (1996) Taku Glacier, southeast Alaska, U.S.A.: Late Holocene history of a tidewater glacier. Arctic and Alpine Research, 28 (1): 42–51.

Muquit MA, Shibahara T (2006) A high-accuracy passive 3D measurement system using phase-based image matching. IEICE Trans. Fundam. Electron. Commun. Comput. Sci., 89 (3): 686–697.

Nagashima S, Aoki T, Higuchi T, Kobayashi K (2006) A subpixel image matching technique using phase-only correlation. In: Proc. IEEE 2006 Int. Symp. Intell. Signal Process.Commun. Syst.: 701–704.

Nagashima S, ISHII H, KOBAYASHI K (2009) High-accuracy estimation of image rotation using 1D phase-only correlation. IEICE TRANSACTIONS on Fundamentals of Electronics, Communications and Computer Sciences, 92 (1): 235–243.

Nagler T, Rott H, Hetzenecker M, Scharrer K, Magnusson E, Floricioiu D, Notarnicola C (2012) Retrieval of 3d-glacier movement by high resolution x-band SAR data. In: IEEE International Geoscience and Remote Sensing Symposium (IGARSS): 3233–3236.

Pan W, Qin K, Chen Y (2009) An adaptable-multilayer fractional Fourier transform approach for image registration. IEEE Transaction on Pattern Analysis and Machine Intelligence, 31 (3): 400–414.

Paul F, et al. (2013) On the accuracy of glacier outlines derived from remote sensing data. Annals of Glaciology, 54 (63): 171–182.

Paul F, Huggel C, Kääb A (2004) Combining satellite multispectral image data and a digital elevation model for mapping debris-covered glaciers. Remote Sensing of Environment, 89: 510–518.

Paul F, Kääb A, Maisch M, Kellenberger T, Haeberli W (2002) The new remote sensing derived Swiss Glacier Inventory: I. Methods. Annals of Glaciology, 34: 355–361.

Paul M, Lin W, Lau CT, s. Lee B (2011) Direct intermode selection for H. 264 video coding using phase correlation. IEEE Trans. Image Process., 20 (2): 461–473.

Pellikka P, Rees W (2010) Remote Sensing of Glaciers: Techniques for Topographic, Spatial and Thematic Mapping of Glaciers. CRC Press, Taylor and Francis Group.

Pelto M (2011) Utility of late summer transient snowline migration rate on Taku Glacier, Alaska. The Cryosphere, 5 (4): 1127–1133.

Pham D, Venkatesh S (2008) Joint learning and dictionary construction for pattern recognition. In: Computer Vision and Pattern Recognition, 2008. CVPR 2008. IEEE Conference on: 1–8.

Pham T, Chin T, Yu J, Suter D (2014) The random cluster model for robust geometric fitting. Pattern Analysis and Machine Intelligence, IEEE Transactions on, 36 (8): 1658–1671.

Prats P, Scheiber R, Reigber A, Andres C, Horn R (2009) Estimation of the surface velocity field of the Aletsch glacier using multibaseline airborne SAR interferometry. IEEE Transactions on Geoscience and Remote Sensing, 47 (2): 419–430.

Pritchard H, Murray T, Luckman A, Strozzi T, Barr S (2005) Glacier surge dynamics of Sortebræ, east Greenland, from synthetic aperture radar feature tracking. Journal of Geophysical Research: Earth Surface (2003-2012), 110 (F3).

Quincey DJ, Copland L, Mayer C, Bishop M, Luckman A, Belò M (2009) Ice velocity and climate variations for Baltoro Glacier, Pakistan. Journal of Glaciology, 55 (194): 1061–1071.

Rastner P, Bolch T, Notarnicola C, Paul F (2014) A comparison of pixel- and object-based glacier classification with optical satellite images. IEEE Journal of Selected Topics in Applied Earth Observations and Remote Sensing, 7 (3): 853–862.

Rees W (2006) Remote Sensing of Snow and Ice. CRC Press, Taylor and Francis Group.

Ren J, Jiang J, Vlachos T (2010) High-accuracy sub-pixel motion estimation from noisy images in Fourier domain. IEEE Trans. Image Process., 19 (5): 1379–1384.

Rignot E, Jacobs SS (2002) Rapid bottom melting widespread near Antarctic ice sheet grounding lines. Science, 296 (5575): 2020–2023.

Rosen P, Hensley S, Joughin IR, Li FK, Madsen SN, Rodriguez E, Goldstein RM (2000) Synthetic aperture radar interferometry. In: Proceedings of the IEEE, 88 (3): 333–382.

Rott H, Mätzler C (1987) Possibilities and limits of synthetic aperture radar for snow and glacier surveying. Annals of Glaciology, 9: 195–199.

Ruan H, Zhang R, Li J, Zhan Y (2016) SAR target classification based on multiscale sparse representation. In: 2015 ISPRS International Conference on Computer Vision in Remote Sensing: 99010T–99010T.

Scambos T, Dutkiewicz M, Wilson J, Bindschadler R (1992) Application of image cross-correlation to the measurement of glacier velocity using satellite image data. Remote Sensing of Environment, 42 (3): 177–186.

Scherler D, Leprince S, Strecker M (2008) Glacier-surface velocities in alpine terrain from optical satellite imagery-Accuracy improvement and quality assessment. Remote Sensing of Environment, 112: 3806–3819.

Schmitt M, Stilla U (2014) Adaptive multilooking of airborne single-pass multi-baseline InSAR stacks. Geoscience and Remote Sensing, IEEE Transactions on, 52 (1): 305–312.

Schubert A, Faes A, Kääb A, Meier E (2013) Glacier surface velocity estimation using repeat TerraSAR-X images wavelet- vs. correlation-based image matching. ISPRS Journal of Photogrammetry and Remote Sensing, 82: 49–62.

Shi J, Hensley S, Dozier J (1997) Mapping snow cover with repeat pass synthetic aperture radar. In: IEEE International Geoscience and Remote Sensing Symposium (IGARSS): Singapore, 2: 628–630.

Shi JC, Dozier J, Rott H (1994) Snow mapping in alpine regions with synthetic aperture radar. IEEE Transactions on Geoscience and Remote Sensing, 32 (1): 152–158.

Shimoni M, Borghys D, Heremans R, Perneel C, Acheroy M (2009) Fusion of PolSAR and PolInSAR data for land cover classification. International Journal of Applied Earth Observation and Geoinformation, 11: 169–180.

Singh G, Venkataraman G, Yamaguchi Y, Park S (2014) Capability assessment of fully polarimetric ALOS-PALSAR data for discriminating wet snow from other scattering types in mountainous regions. IEEE Transactions on Geoscience and Remote Sensing, 52 (2): 1177–1196.

Stefano LD, Mattoccia S, Tombari F (2005) ZNCC-based template matching using bounded partial correlation. Pattern recognition letters, 26 (14): 2129–2134.

Stilla U, Soergel U, Thoennessen U (2003) Potential and limits of InSAR data for building reconstruction in built-up areas. ISPRS Journal of Photogrammetry and Remote Sensing, 58 (1): 113–123.

Stone HS, Orchard MT, Chang EC, Martucci SA (2001) A fast direct Fourier-based algorithm for subpixel registration of images. IEEE Trans. Geosci. Remote Sens., 39 (10): 2235–2243.

Strozzi T, Luckman A, Murray T, Wegmüller U, Werner C (2002) Glacier motion estimation using SAR offset-tracking procedures. IEEE Transactions on Geoscience and Remote Sensing, 40 (11): 2384–2391.

Sun L, Ji S, Ye J (2013) Multi-label dimensionality reduction. CRC Press.

Szeliski R, Scharstein D (2002) Symmetric sub-pixel stereo matching. In: Computer Vision-ECCV 2002 (pp. 525–540). Springer.

Tennakoon R, Bab-Hadiashar A, Cao Z, Hoseinnezhad R, Suter D (2015) Robust model fitting using higher than minimal subset sampling.

Thiagarajan J, Ramamurthy K, Knee P, Spanias A, Berisha V (2010) Sparse representations for automatic target classification in SAR images. In: Communications, Control and Signal Processing (ISCCSP), 2010 4th International Symposium on: 1–4.

Tong X, Ye Z, Xu Y, Liu S, Li L, Xie H, Li T (2015) A Novel Subpixel Phase Correlation Method Using Singular Value Decomposition and Unified Random Sample Consensus. IEEE Transactions on Geoscience and Remote Sensing, 53 (8): 4143–4156.

Trouve E, Vasile G, Gay M, Bombrun L, Grussenmeyer P, Landes T, Nicolas J, Bolon P, Petillot I, Julea A, Valet L, Chanussot J, Koehl M (2007) Combining Airborne Photographs and Spaceborne SAR Data to Monitor Temperate Glaciers: Potentials and Limits. IEEE Transactions on Geoscience and Remote Sensing, 45 (4): 905–924.

Tsai D, Lin C, Chen J (2003) The evaluation of normalized cross correlations for defect detection. Pattern Recognition Letters, 24 (15): 2525–2535.

Vandewalle P, Sü S, Vetterli M (2006) A frequency domain approach to registration of aliased images with application to super-resolution. EURASIP J. Appl. Signal Process., 2006: 1–14.

Vasile G, Trouvé E, Lee J, Buzuloiu V (2006) Intensity-driven adaptive-neighborhood technique for polarimetric and interferometric sar parameters estimation. IEEE Transactions on Geoscience and Remote Sensing, 44 (6): 1609–1621.

Veetti B (2009) Use of Landsat TM imagery for mapping debris-covered glaciers in the Karakoram Himalayas, Northern Pakistan. Master's thesis, University of Dundee.

Venkataraman G, Singh G, Kumar V (2008) Snow cover area monitoring using multitemporal TerraSAR-X data. In: in Proc. 3rd TerraSAR-X Sci. Team Meeting: 1–7.

Wang T, Jonsson S, Hanssen RF (2014) Improved SAR image coregistration using pixel-offset series. IEEE Geoscience and Remote Sensing Letters, 11 (9): 1465–1469.

Wohlleben T, Howell SE, Agnew T, Komarov A (2013) Sea-Ice Motion and Flux within the Prince Gustaf Adolf Sea, Queen Elizabeth Islands, Canada during 2010. Atmosphere-Ocean, 51 (1): 1–17.

Wright J, Yang A, Ganesh A, Sastry S, Ma Y (2009) Robust face recognition via sparse representation. Pattern Analysis and Machine Intelligence, IEEE Transactions on, 31 (2): 210–227.

Xiao J, Li J, Moody A (2003) A detail-preserving and flexible adaptive filter for speckle suppression in SAR imagery. International Journal of Remote Sensing, 24 (12): 2451–2465.

Yan S, Tang X (2006) Trace quotient problems revisited. In: Computer Vision–ECCV 2006 (pp. 232–244). Springer.

Yang J, Wang Z, Lin Z, Cohen S, Huang T (2012) Coupled dictionary training for image super-resolution. Image Processing, IEEE Transactions on, 21 (8): 3467–3478.

Yang J, Yu K, Huang T (2010) Supervised translation-invariant sparse coding. In: Computer Vision and Pattern Recognition (CVPR), 2010 IEEE Conference on: 3517–3524.

Yang M, Zhang L, Feng X, Zhang D (2014) Sparse Representation Based Fisher Discrimination Dictionary Learning for Image Classification. International Journal of Computer Vision, : 1–24.

Yommy A, Liu R, Wu S (2015) SAR Image Despeckling Using Refined Lee Filter. In: Intelligent Human-Machine Systems and Cybernetics (IHMSC), 2015 7th International Conference on, 2: 260–265.

Yu H, Yang J (2001) A direct LDA algorithm for high-dimensional data-with application to face recognition. Pattern recognition, 34 (10): 2067–2070.

Zhang L, Gruen A (2006) Multi-image matching for DSM generation from IKONOS imagery. ISPRS Journal of Photogrammetry and Remote Sensing, 60 (3): 195–211.

Zhang LM, Sun LZ, Zou B, Moon W (2015) Fully polarimetric SAR image classification via sparse representation and polarimetric features. Selected Topics in Applied Earth Observations and Remote Sensing, IEEE Journal of, 8 (8): 3923–3932.

Zhou J, Li Z, He X, Tian B, Huang L, Chen Q, Xing Q (2014) Glacier thickness change mapping using InSAR methodology. IEEE Geoscience and Remote Sensing Letters, 11 (1): 44–48.

Zitova B, Flusser J (2003) Image registration methods: a survey. Image and vision computing, 21 (11): 977–1000.

Lebenslauf

Name	Li Fang
Geburtstag und -ort	06.02.1986 in China
Wohnort	Oberhofer platz 10 80807 München

Ausbildung/Tätigkeit

2003 – 2007	Bachelor of Engineering in Land Resources Management China University of Geosciences, Wuhan (Wuhan, China)
2007 – 2009	Master of Science in Physical Geography China University of Geosciences, Wuhan (Wuhan, China)
2009 – 2011	Master of Science in Land Management and Land Tenure Technische Universität München (Munich, Germany)
2011 – 2016	Doctoral Candidate at Technische Universität München (Munich, Germany). CSC Research Fellowship

Acknowledgment